THE ANALYSIS OF SEPARATION AND METHODS OF THREE-DIMENSIONAL FLOW STRUCTURE DETECTION IN THE BOUNDARY LAYER SHOCK WAVE INTERACTION

JUSTYNA CZERWIŃSKA

Insititute of Fluid Flow Machinery
Polish Academy of Sciences
Fiszera 14, 80-952 Gdansk, Poland

Abstract: The normal shock wave turbulent boundary layer interaction still draws a great deal of attention as a flow phenomenon. This is due to its profound importance to numerous applications. The understanding of phenomena is crucial for future aims connected with the interaction control. Experimental investigations of the interaction have been carried out since the 1940s. They were aimed however at the determination of such general flow features as: pressure distribution, shock wave configuration or oil visualization of separation structures. In order to better understand the phenomenon, measurements of the entire field are required. At present, such measurements do not exist. A great help is expected from numerical simulations in this respect. There is enough experimental data to check the general features of the flow obtained from calculations. This thesis presents numerical simulations of flow that is assumed: steady, three-dimensional, compressible, viscous and turbulent. Its general aim is to present to what extend the modern numerical methods are able to predict the flow in shock wave turbulent boundary layer interaction including shock induced separation structures. These structures are very sensitive to channel geometry and may be useful in the understanding of separation's development.

In order to illustrate the abilities of numerical simulations, one aim of the presented thesis is to investigate the effect of the span-wise depth of the nominally two-dimensional test section. The presented results cast some light on the common problems experienced by typical comparisons of two-dimensional simulations to wind tunnel tests having a three-dimensional nature.

The first Chapter presents the basic theory of elementary structures. Considerations of elementary structures of the flow along with their dependencies are necessary for a better understanding of the separation flow structures induced by the boundary layer shock wave interaction. The classification of elementary structures will be presented. In addition, the possible occurrence of bifurcation will also be studied.

The second Chapter will be devoted to studying specific cases of transonic turbulent flow. The analysis of numerical results will be bounded to the shock wave structure. Studies shall include: the influence of the numerical scheme, three-dimensional effects connected with the changing width of the channel, a comparison to experiment and the influence of the symmetric boundary condition on the flow prediction in the channel. Finally, the boundary layer influence on the λ-foot structure will also be presented.

Chapter three will present the separation structures. Here too a comparison to experiments will be done. Changes in separation structures connected with the width of the channel will be studied. The influence of the symmetry boundary condition will be shown. Finally, the specification of the basic flow structures will be done.

Keywords: shock wave-boundary layer interaction, flow separation, 3-D flow structures, numerical simulations

1. The basic theory of elementary topological structures

1.1 Introduction

In this chapter the theory of elementary structures will be presented. It will contain the two- and three-dimensional analysis. For these two approaches the classification of structures and some possible bifurcations of such structures will be described. The conditions of the connections of the elementary structures will be also considered.

These two main considerations are important when the topological analysis is applied to fluid dynamics. Flow patterns like skin friction lines and streamlines are important elements in the description of fluid motion from the experimental and numerical point of view. The knowledge of basic topology is necessary to make a proper analysis of pictures containing flow pattern lines. A consideration of bifurcations is important when the entire class of flows are considered. Finally, the main point of interest is to concentrate on the influence of specific parameters on changes in flow. Such changes might include separation's occurrence and disappearance or any general flow pattern's change.

Based on the velocity field, the reconstruction and recognition of the basic flow features is possible. In this process, knowledge about the classification of elementary structures and their basic properties is helpful. All these main goals will be described in more details in the present chapter.

1.2 The classification of critical points

In this section the classification of elementary structures will be presented. This task can be done using the two and three-dimensional analysis. The problem of the classification of elementary structures is important for several purposes including: to standardize basic flow structures and their properties, to make a conclusion about the possibilities of changes in those structures and to make the process of obtaining the basic skeleton of flow patterns from the vector field more efficient.

To classify the structures or to decide on the type of critical points it is necessary to introduce a few definitions. First of these is the *structural stability*. The dynamic system of ordinary differential equations is structurally stable when the obtained system, by any small perturbation of vector field, is adequate to the original one. To complete the definition it is necessary to specify what kind of transformation, or mapping, is considered sufficient for both systems. The given transformation should be a differentiable and reversible mapping which transforms the oriented phase trajectories of the first dynamical system to the oriented phase trajectories of the second one. There is no need for the orientation of the curves to be the same.

In the two- and three-dimensional space the trajectories tend to the set of measure zero-attractor. This could be a single point, a closed cycle or a strange attractor. For two-dimensional cases of an autonomous system, the Poincaré--Bendinxon theorem reassures that the attractors could only be single points or

closed curves. The three-dimensional case further expands the possibilities to the inclusion of a strange attractor.

There are two types of *isolated critical points*: non-degenerate and degenerate. The degenerate point appears when the eigenvalue of the linearized vector field is equal to zero. The difference between these types of points is seen when a small change in the vector field is considered. In the case of the non-degenerate critical point it will not disappear but can change its position slightly. The degenerate critical point can disappear, split into more non-degenerate critical points or change to a non-degenerate critical point. The definition of the structural stability introduces the first type of classification. In real flow, when the flow patterns are taken into account, almost all cases have non-degenerate critical points. The degenerate critical point gains interest when more than one specific flow patterns is considered and information about possible bifurcations is desired. It means — when the group of flow patterns is considered and especially when the main interest is to study the process of changes between different flow patterns.

A study of the mentioned bifurcation will be done in the next section. In Chapter 3, changes of structures in the transonic turbulent flow of two nozzles will be presented. Due to this, attention in the present section will be paid to the non--degenerate critical points.

A consideration similar to the one for critical points can also be done for closed curves (cycles). A cycle is degenerated if the eigenvalue of the linearized Poincaré mapping is one. To understand this definition, an explanation of the Poincaré transformation is necessary. It follows that if a given curve is cut by a plane perpendicular to it, then the transformation of the point near the cut on one side transforms it to a point near the cut on the other side (after one cycle). This kind of transformation is called a *Poincaré transformation* (see Figure 1.1).
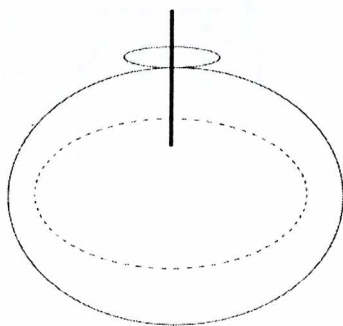
Figure 1.1. *The definition of the Poincarè transformation.*

Another approach to classifying the critical points is based on the linearization of the original system of equations in the neighborhood of a critical point. The mathematical details of such an approach are presented in Appendix A. Here the attention will be drawn to the main assumptions. The character of a critical point

depends on the signs and values of the eigenvalues of the linearized matrix of coefficients in the vicinity of the critical point.

With the definitions mentioned, it is now possible to describe the classification of critical points.

In two dimensions, the following points are possible: saddles, stable and unstable star, degenerate and ordinary nodes, stable and unstable focal (or spiral) points and centers. The structural stable points are saddles, nodes and spiral points. All such points are presented in Figure 1.2.
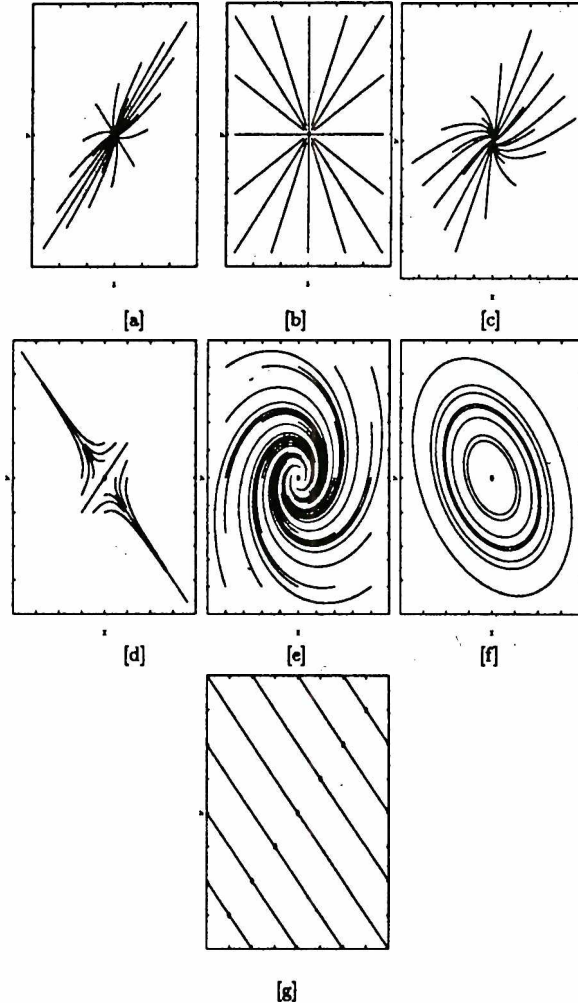
Figure 1.2. *The two dimensional critical points. [a] node; [b] star node; [c] degenerate node; [d] saddle; [e] focus; [f] center; [g] the trajectories are straight lines.*

Usually the set of critical points is considered. For this reason it is necessary to examine the stability of the group of singular points. The following theorem covers stability of the vector field.

Theorem:

The two-dimensional vector field is structurally stable when the following conditions are met:

— The field has a finite number of critical points

— All critical points are non-degenerate

— Any of the outcome node separatrics is not the income node separatrics

— The field has a finite number of closed phase trajectories

— All closed phase curves are non-degenerate cycles

This previous classification of the vector field is generally restricted to most cases of fluid dynamics when flow patterns are considered and also in the case of some specific structures called bifurcation lines. The only exception to this is the consideration of the bifurcation of flow patterns.

When the above classifications and theorems are known, the interpretation of either skin friction lines or two-dimensional streamlines is possible.
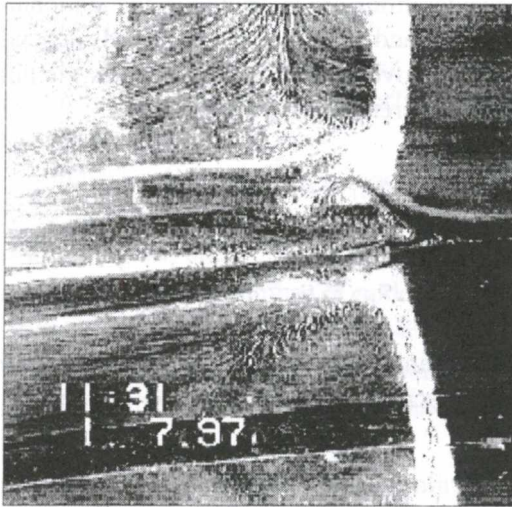
Figure 1.3. Picture of oil flow visualization on the surface. Main flow direction: right to left.

The fist approach to analyzing possible flow structures was done by Oswatitsch (1958) using the non-slip condition. Next, Lighthill (1963) studied and developed the Oswatitsch solutions further. Perry and Fairlie (1974) implemented the ordinary differential equations to describe the critical points. When the distribution of critical points is known, flow patterns such as skin friction lines (example in Figure 1.3) or streamlines can be obtained. The solution obtained by Oswatitsch was based on a series expansion to the second order terms and was only valid in the neighborhood of a critical point. Later, Dallmann (1983) showed that, when considering the higher order terms of the expansion, it was possible to obtain the entire set of critical points.

The subject was also studied by Tobak and Peake (1979) and Legendre (1977). Below is a short description of the process of obtaining the skin friction lines.

The viscous flow near the three-dimensional surface will be considered. The skin friction lines are the trajectories of the continuum vector field. (ξ, η) are the coordinates of the curvilinear coordinate system. Axes χ, η are attached to the body and axis ζ is perpendicular to the surface. In the neighborhood of a critical point, the velocity vector is parallel to the surface. Because of this, the movement of the element of flow along the given streamlines will be described by the following equations:

$$h_1(\xi,\eta)\frac{d\xi}{dt} = \zeta\frac{\partial u_1}{\partial\zeta}(\xi,\eta,0) = -\zeta\omega_2(\xi,\eta) = \zeta P(\xi,\eta), \tag{1.1}$$

$$h_2(\xi,\eta)\frac{d\eta}{dt} = \zeta\frac{\partial u_2}{\partial\zeta}(\xi,\eta,0) = \zeta\omega_1(\xi,\eta) = \zeta Q(\xi,\eta), \tag{1.2}$$

where $h_1(\xi, \eta)$ and $h_2(\xi, \eta)$ are the lengths of the vectors, (ω_1, ω_2) are the components of the rotation on the surface. Velocities (u_1, u_2) are the moment values and due to this; the considerations are restricted to the stationary flow. The coordinate ζ will be the parameter and functions P and Q will depend only on that coordinate. In such a case, the above system of equations is the autonomical two equation system of ordinary differential equations. If also

$$\tau_{w1} = \mu\frac{\partial u_1}{\partial\zeta}(\xi,\eta,0), \tag{1.3}$$

$$\tau_{w2} = \mu\frac{\partial u_2}{\partial\zeta}(\xi,\eta,0), \tag{1.4}$$

are the components of the tangential surface tension in the direction ξ and η, then the system of equations describing the skin friction patterns is given by:

$$\frac{h_1 d\xi}{\tau_{w1}} = \frac{h_2 d\eta}{\tau_{w2}}. \tag{1.5}$$

The orthogonal lines to the skin friction lines are the lines of the vorticity on the surface. The critical points appear when vector (τ_{w1}, τ_{w2}) is equal to zero.

In real flows, the skin friction lines are obtained either from computations (which will be considered in Chapter 3) or by oil visualization. In such a case, the system of critical points (not just one isolated point) is considered. In such analyses it is helpful to take into account the theorem relating the index of the vector field from the analysis of manifold. An investigation will be made of the closed curve which is not intersecting the critical point, and the vector field. There will also be an investigation involving the point on the curve that will follow the curve in the positive direction. When this point has followed the entire trace of the curve and has returned to the original position, the vectors will also be at the initial condition, but on the way they could do a few cycles. The number of cycles is the index of the

curve. With this it is possible to define the index of critical point. The considered curve will be a circle with sufficiently small radius and with the middle in the critical point. From the definition of the index of critical point it is easy to see that the basic critical points have indexes −1 or +1 (node and focus +1, saddle −1).

Theorem:

The sum of index of critical points on the compact manifold does not depend on the choice of the vector field, but is the property of the manifold itself.

This theorem excludes some combinations of critical points as impossible from the topological point of view and is used in analyzing the skin friction lines obtained, for instance, by oil visualization.

From this theorem, the following conditions are concluded.

— The difference between the number of nodes and foci and the number of saddles equals two when the skin friction lines on the three dimensional body or infinite surface are considered, Davey 1961, Lighthill 1963.

— The number of nodes and foci is equal to the number of saddles when the lines on the three dimensional body connected without the break with the infinite surface are considered, Tobak and Peake 1982.

— The difference between the number of saddles and the number of nodes and foci equals one when the two-dimensional surface cuts the three dimensional body, Tobak and Peake 1982.

— The number of saddles and the number of nodes and foci are equal when we consider the plane perpendicular to the body, cutting the body and spreading to infinity, Tobak and Peake 1982.

— The number of saddles and the number of nodes and foci are equal when we consider the streamlines on the sphere in cone flow, Smith 1969.

— The sum of the nodes and half nodes minus the sum of saddles and half saddles equals -1 for a streamline on a two-dimensional plane cutting a three-dimensional body, Hunt 1978.

The last four cases describe the behavior of streamlines and the two first cases are connected with the skin friction lines.

After considering two-dimensional structures and their classification, the three-dimensional approach will be presented. This case is usually less considered or even neglected in most literature because of a bit larger mathematical complexity of equations and because in most cases the three-dimensional analysis is not necessary to investigate physical problems. In this section, and also further in other chapters, the three-dimensional approach is necessary and the three-dimensional flow patterns will be considered.

The mathematical details of the classification based on the linearized vector field are presented in Appendix A. In Figure 1.4, the diagram of possible eigenvalues is presented. The third order polynomial, obtained from the characteristic matrix can have three real roots or one real and two complex conjugate roots.
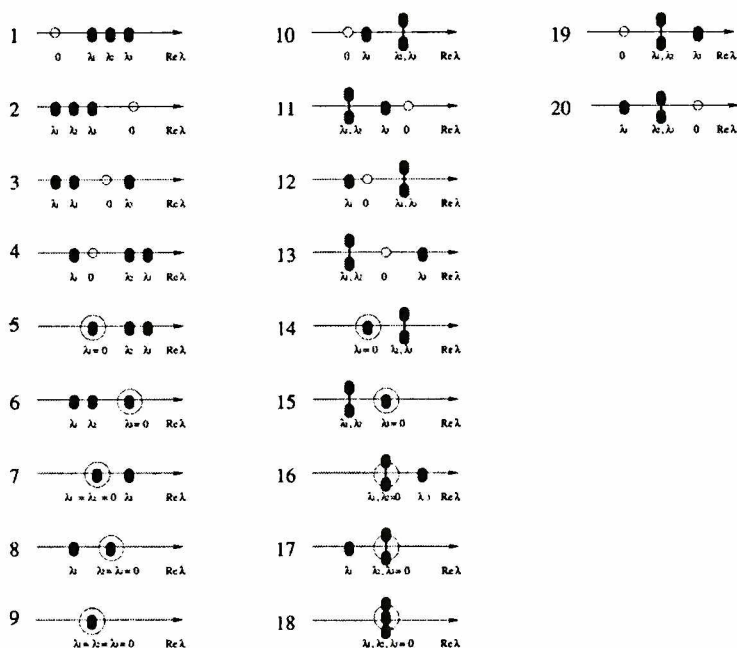
Figure 1.4. *Diagram of the eigenvalues.*

The diagram of eigenvalues is presented to help understand the nature of the critical points in three-dimensional space. In Figure 1.5 the classification of the critical points in three-dimensions is presented. Some degenerate points are not shown including the case when the phase plane is a superposition of linear two-dimensional planes. It is interesting that there are three different types of focal points. The projection of the trajectories on the perpendicular plane in all cases is the same, except for the direction, but the three-dimensional curve behavior is different. This becomes especially important when only the cross section is given because the direction of the line could be towards the critical point. On the other hand, in three-dimensional space this can mean that this is the stable point (the flow tends to this point) or the unstable condition in which flow tends to infinity on a perpendicular trajectory to the considered cross-section. This can lead to an incorrect interpretation of some two-dimensional pictures of flow patterns because the flow is always three-dimensional.

The consideration of the structural stability of the field is the same as in the two-dimensional case. Also, the definition of the index of the critical point is the same as in the case for two-dimensions but instead of the curve, the oriented surface is considered.

The index of critical points is:

1. $Re\lambda_i >= 0$, $i = 1, 2, 3$ — +1;
2. $Re\lambda_1 >= 0$, $Re\lambda_2 >= 0$, λ_3 real and negative — −1;
3. λ_1 real and positive, $Re\lambda_2 <= 0$, $\lambda_3 <= 0$ — +1;
4. $Re\lambda_i <= 0$, $i = 1, 2, 3$ — −1.
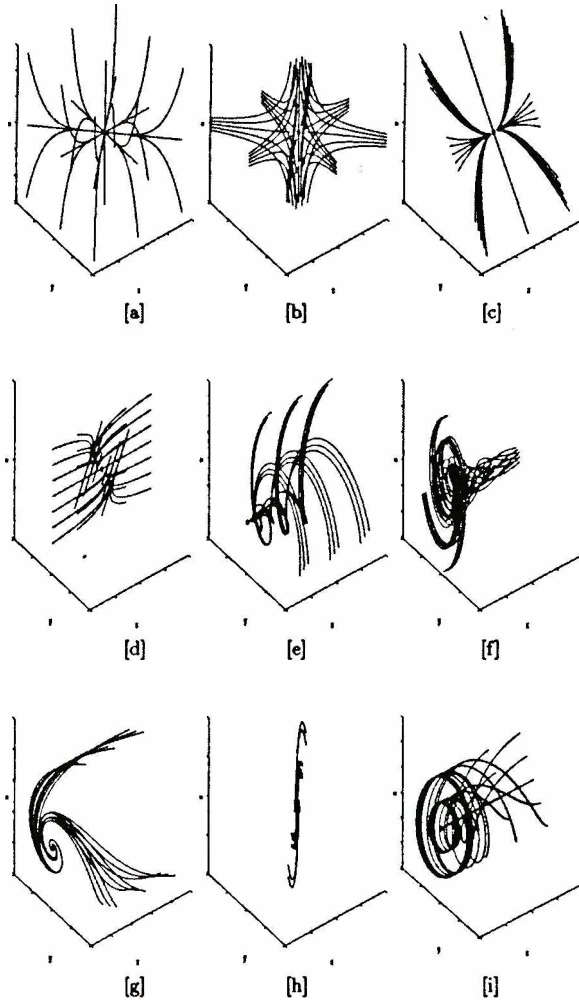
Figure 1.5. *Three-dimensional critical points.*

Similar to the case of the two-dimensional manifold, the sum of indices depends only on the manifold. From this it is possible to consider some specific case of manifolds.

— For the three-dimensional space the sum of indexes should be zero

To complete the investigation of the classification of the three-dimensional critical points it is necessary to describe the connection of the above consideration with the solutions of the Navier-Stokes equations. There could be two approaches divided by the reference coordinate system.

In the system connected with the moving fluid particle, the assumptions are as follows. The system (Lagrange system of coordinates) is non-rotating and ties up with the moving fluid particle. The neighborhood is sufficiently local for the linear approximation to be valid. The instantaneous velocity field can be expressed as:

$$\dot{x} = \mathbf{A}x. \tag{1.6}$$

The Jacobian matrix $\mathbf{A}$ is a matrix 3×3, where the elements are given by:

$$a_{ij} = \frac{\partial \dot{x}_i}{\partial x_j}. \tag{1.7}$$

This is the rate of deformation tensor and can be split into a symmetric and anti-symmetric part.

$$a_{ij} = S_{ij} + R_{ij}, \tag{1.8}$$

where the symmetric part is

$$S_{ij} = \frac{1}{2}\left[\frac{\partial \dot{x}_i}{\partial x_j} + \frac{\partial \dot{x}_j}{\partial x_i}\right], \tag{1.9}$$

and the antisymmetric part:

$$R_{ij} = \frac{1}{2}\left[\frac{\partial \dot{x}_i}{\partial x_j} - \frac{\partial \dot{x}_j}{\partial x_i}\right]. \tag{1.10}$$

The S_{ij} is the rate of strain tensor and R_{ij} is the rotation (or spin) tensor. The R_{ij} has three independent components and these components are the three components of vorticity.

The above set of equations represents the basic kinematics of fluid. Fluid motions can be reduced to the above set of equations locally relative to an observer moving with the fluid particle.

The properties of the flow patterns for the above equations could be investigated from the equation on the eigenvalues of this system. The eigenvalues are given by the solution of the equation:

$$\lambda^3 + P\lambda^2 + Q\lambda + T = 0, \tag{1.11}$$

where

$$P = -trace\,[A] = -S_{ij}, \tag{1.12}$$

$$Q = \frac{1}{2}\left(P^2 - trace[\mathbf{A}^2]\right) = \frac{1}{2}\left(P^2 - S_{ij}S_{ji} - R_{ij}R_{ji}\right), \tag{1.13}$$

$$T = -det[\mathbf{A}] = \frac{1}{3}\left(-P^3 + 3PQ - trace[\mathbf{A}^3]\right) =$$

$$= \frac{1}{3}\left(-P^3 + 3PQ - S_{ij}S_{jk}S_{ki} - 3R_{ij}R_{jk}R_{ki}\right). \tag{1.14}$$

The surface given by equations:

$$\frac{1}{3}P\left(Q - \frac{2}{9}P^2\right) - \frac{2}{27}\left(-3Q + P^2\right)^{\frac{3}{2}} - T = 0, \tag{1.15}$$

$$\frac{1}{3}P\left(Q - \frac{2}{9}P^2\right) + \frac{2}{27}\left(-3Q + P^2\right)^{\frac{3}{2}} - T = 0, \tag{1.16}$$

is the surface which splits solutions either to 2 complex and one real eigenvalue (above the surface), or to three real eigenvalues (below). This consideration has to be a bit improved in order to satisfy the non-slip boundary conditions for the separation case. The perpendicular coordinate to the wall is x_3 so it is necessary to transform the system of equation

$$dt_{new} = x_3 dt, \tag{1.17}$$

and then the non-slip boundary condition is satisfied at $x_3 = 0$. The matrix **A** is no longer the rate of deformation tensor, but it is made up of elements of the local pressure gradients and gradients of vorticity. In the case of incompressible flow the considerations are restricted to the plane (Q-T) in which only saddle points (not pure nodes) are possible. In compressible flow pure node points are also possible.

Another approach to interpret flow patterns is the global one. In such a case the solutions of Navier-Stokes equations are examined but also in some vicinity of the critical points. The solutions of the Navier-Stokes equations

$$\frac{\partial \rho}{\partial t} + div(\rho\mathbf{V}) = 0, \tag{1.18}$$

$$\frac{\partial \mathbf{V}}{\partial t} + grad\left(V^2 / 2\right) - \mathbf{V} \times rot\mathbf{V} = -\frac{1}{\rho}div\Pi + \mathbf{f}, \tag{1.19}$$

$$\rho\frac{d}{dt}\left(i + V^2 / 2\right) = div\Pi\mathbf{V} + \rho\,\mathbf{f}\,\mathbf{V} - div\mathbf{q}, \tag{1.20}$$

$$\frac{p}{\rho} = \frac{\kappa - 1}{\kappa}i, \tag{1.21}$$

are obtained by performing the Taylor expansions of velocity field vector.

$$\dot{x} = u = \sum_{i=0}^{N}\sum_{j=0}^{N-1}\sum_{k=0}^{N-1}U_{ijk}x^i y^j z^k + O(N+1), \tag{1.22}$$

$$\dot{y} = v = \sum_{i=0}^{N}\sum_{j=0}^{N-1}\sum_{k=0}^{N-1}V_{ijk}x^i y^j z^k + O(N+1), \tag{1.23}$$

$$\dot{z} = w = \sum_{i=0}^{N} \sum_{j=0}^{N-1} \sum_{k=0}^{N-1} W_{ijk} x^i y^j z^k + O(N+1). \tag{1.24}$$

The coefficients U_{ijk}, V_{ijk} and W_{ijk} are unknown constants. Due to the flow equations and the boundary conditions some relations between those coefficients exist and reduce the number of coefficients that could be chosen independently. In the case of an N order Taylor expansion the phase portrait of the truncated system is studied. Due to this fact, it is necessary to study whether the order of expansion is sufficient for the considered flow topology and mainly the description of the degenerate critical points is necessary. For the case of the incompressible flow near the viscous wall the Navier-Stokes equations can be reduced to:

$$\dot{x} = \mathbf{B}x + O(2), \tag{1.25}$$

where matrix $\mathbf{B}$

$$\mathbf{B} = \frac{1}{\mu} \begin{pmatrix} \tau_x & \dfrac{1}{2}p_x & \tau_z \\ 0 & \dfrac{1}{2}p_y & 0 \\ \sigma_x & \dfrac{1}{2}p_z & \sigma_z \end{pmatrix}. \tag{1.26}$$

The shear stresses in respectively x and z directions are defined by $\tau = \mu\,(u_y)\,|_{y=0}$, and $\sigma = \mu\,(w_y)\,|_{y=0}$ and wall position is at $y = 0$.

Above the classification of the two- and three-dimensional critical points was presented. The attention was restricted to the non-degenerate critical points. In the next section the degenerate and structurally unstable critical points will be presented in more details.

1.3 Bifurcations

This section will be devoted to the subject of bifurcation. The word bifurcation is used in the sense of the description of any qualitative change of topological structure with some parameter. In this section some basic deformations of the trajectories near isolated critical points or cycles will be considered. In the case of the investigation of the whole family of different objects, like pictures of trajectories, some general position of objects might be found. The topological character of the system of critical points in general position cannot be changed by small deformations. Such cases are generally more important to investigate in terms of the analysis of some physical processes. Basic information of such analysis was presented in the previous section. When the entire group of the family of the simple cases of trajectories is considered and when information about the entire possible changes is expected, there is a need to also investigate the specific class (i.e. for critical points, degenerate critical points or for cycles — degenerate cycles.)

The subject matter of this section falls into two parts. In the first part, basic methods of the theory of bifurcations will be presented. The next step will be to show some specific cases of bifurcations. The need for this is connected with Chapter 3 in which such cases of changes of topological structures of turbulent flow past the nozzle will be presented.

Two general problems are associated with bifurcation:
— to what extent the geometrical structure of the solution is resistant to perturbation;
— to what extent expansions in a series nearby a stationary state may be used.
These problems are connected with the structural stability.

First, attention will be paid to the definition of the co-dimension and the k-parameter family. Both these definitions are necessary and connected somehow with the definition of bifurcations. These definitions could be better presented and understood with Figure 1.6.
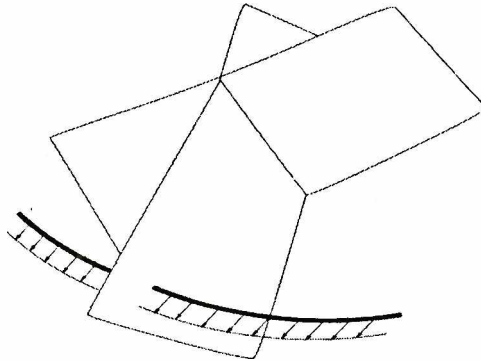
Figure 1.6. *Schematic picture of the space of the entire family of possible topological structures. Planes present the critical parameters when the bifurcations occur. The bold line is an example of one single family.*

Figure 1.6 schematically presents the space of the entire range of families where topological changes occur. The bold line is schematically one family (for instance it could be one critical point.) Each single object of the family can be, of course, moved to the general position with some change of parameter but the entire family cannot. The planes are the values of some parameters for which the changes of topological structures are present. It could be, for example, when the value of the non-degenerate critical point appears. For the entire range of cases in which the family of topological structures is considered, there always exist some critical values of parameters, called the bifurcation parameter, which cannot be removed. The small perturbation will only move the range of parameters a bit (see Figure 1.6.) It is also shown that the space of bifurcation parameters could have singularities, which in Figure 1.6 are presented as a cross-section of two planes. Such cases can be neglected when the considerations of family changing the topological structures is taken into account due to the fact that a small disturbance

of parameters will move the entire family (bold line in Figure 1.6) from this singular position. It is also described as a theorem that, when the k-dimensional family of parameters is considered, higher dimensional cases can be always reduced to the lower level — k. It will be possible now to understand the definition of the k-parameter family. This is the family of possible changes of topological structures in which the changes depend on the k-parameters. In Figure 1.6, the bold line is the one parameter family. The co-dimension of the singularity is the dimension of the k-parameter family and it is equal k. All higher parameter singularities, when k co-dimension is considered, can be reduced to the k- parameter case. On the other hand, in case of the k-parameter family, the non-removable will be singularities with dimension less than k.

With these definitions it is possible to concentrate on bifurcations. The methodology of analyzing the bifurcations of the family can be divided into two steps: the first one is to describe the co-dimension of the singularity and the next one is to show all possible bifurcations in this family.

Another problem connected with bifurcation is the question of what are the possible changes of specific structures. This is a question of how many points will split the non-degenerate critical point (or adequate cycles). This can be checked only by specific consideration about a chosen degenerate critical point. For example, the saddle-node point splits into two points: saddle and node.

$$\dot{x} = x^2;\tag{1.27}$$

$$\dot{y} = -y.\tag{1.28}$$

When the perturbation is added to the above equation

$$\dot{x} = x^2 - \varepsilon;\tag{1.29}$$

$$\dot{y} = -y;\tag{1.30}$$

it is easy to see that there are two non-degenerate critical points: saddle and node.

The k-parameters families have some global characteristic properties. One of these is the dimension of the bifurcation diagram. The bifurcation diagram is the diagram that presents the splitting of the space of parameters in the case of topological changes in a dynamical system.

Here are the three basic families of bifurcation:
— one parameter family; in such a case the characteristic matrix has one zero or a pair of imaginary — conjugate eigenvalues; examples: saddle-node bifurcation, transcritical bifurcation, Pitchfork bifurcation (real eigenvalue), Hopf bifurcation (pure imaginary eigenvalue).
— two parameters family; an example of the bifurcation diagram is shown in Figure 1.7.
— three parameters family.
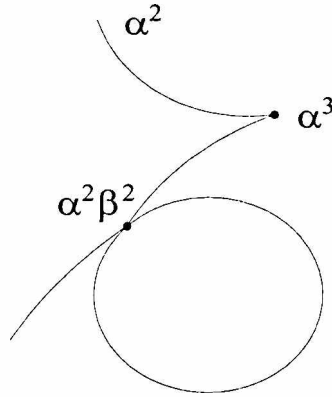
Figure 1.7. *The bifurcation diagram for two parameter family. Cusp — triple eigenvalue, crossing point — two double eigenvalues, line — one double eigenvalue, whole space — non-degenerate critical point.*
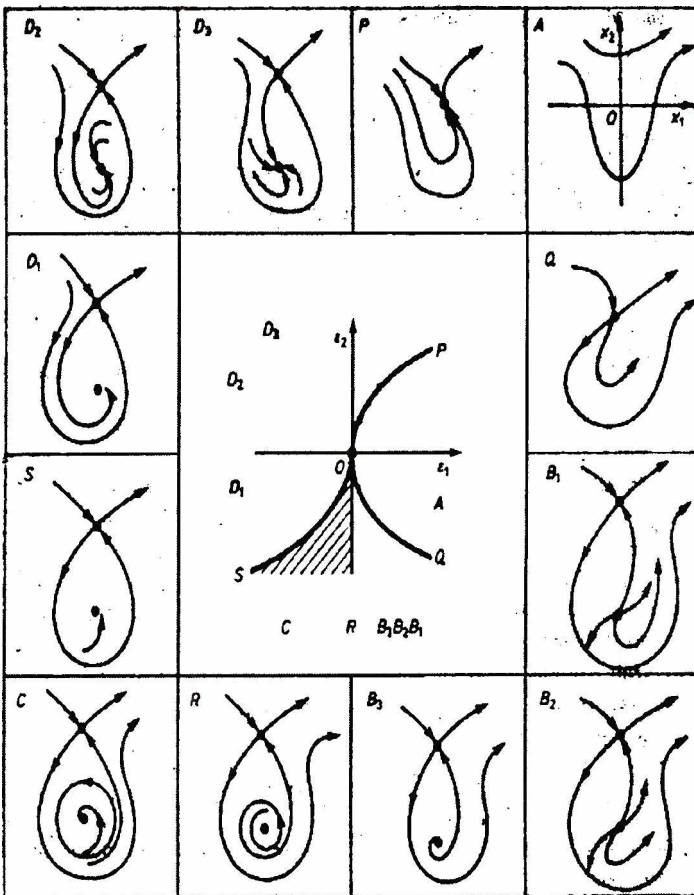
Figure 1.8. *Takens-Bogdanov bifurcation's diagram.*

The following consideration can be continued for the highest dimensional parameter families. It will become much more complicated and in the case of usefulness for Chapter 3, those considerations are not necessary.

For the purpose of Chapter 3, one specific bifurcation should be presented. This bifurcation is called the Takens-Bogdanov bifurcation. It is a two parameter family bifurcation and the standard form for it is:

$$\dot{x} = y; \tag{1.31}$$

$$\dot{y} = c_1 + c_2 x + x^2 + xy; \tag{1.32}$$

where c_1 and c_2 are parameters. In Figure 1.8 the bifurcation diagram and trajectories are presented. This specific bifurcation is mentioned, because very similar changes of critical points will be observed with changes in separation structures in Chapter Three.

1.4 Summary

— Two-dimensional structurally stable critical points are: node, saddle and focal point. The nodes and foci can be stable or unstable depending on the direction of the trajectories.

— Three-dimensional structurally stable critical points are: node, saddle and focal point. There are three types of focal points and two types of saddle points. Saddle point in three-dimensions in two cross-sections is two-dimensional saddle and in third direction is a two-dimensional node (stable or unstable). Due to this there are two types of saddle points in the three-dimensional space depending on the character of the two-dimensional node.

— Three-dimensional node can only exist for compressible flow.

— Some combination of critical points are not possible — like saddle saddle in two-dimension. The theorem regarding the index assure which combinations can be stable.

2. Turbulent boundary layer shock wave interaction — flow structure

2.1 Introduction

This chapter will be devoted to the turbulent boundary layer shock wave interaction. This phenomenon is very important for aviation and turbomachinery. First investigations of this subject were done in the 1940's. Such studies were connected with the growing speed of planes. It is especially important for supersonic aircraft in which the turbulent boundary layer separates due to interactions with the shock wave resulting in larger drag. Similar phenomenon exists at the rotor blades of helicopters in which the flow at the blade tip is transonic and for planes with transonic wings where local area on the wing is transonic. Boundary layer shock wave interaction is also important for reentry

vehicles where, due to the mentioned interaction, the turbulent boundary layer causes larger heating than a laminar boundary layer in the part of the vehicle where it appears. It is also significant for inner flows such as those in turbines where things are even more complicated by the reflection of the shock waves and there is a need to estimate the losses cased by the turbulent boundary layer shock wave interaction.

In this paper attention will be focused on transonic speed and the turbulent boundary layer. Separation that appeared due to this interaction is very interesting to study in terms of flow structures, which can be studied using methods presented in Chapter 1. Phenomena in such flow also have a very wide range of industrial applications.

The shock wave causes local discontinuity in parameters. In contact with the wall, the local area has to be subsonic and this jump cannot be discontinuous. Due to this fact, an increase of pressure has to take place along the wall in a continuous way. In the subsonic region the streamlines diverge due to pressure increase and move from the wall. The type of structure built of two shocks is called the λ-foot. This phenomenon depends on properties of the boundary layer as well as on the normal shock wave far from the wall. If the pressure jump is high the boundary layer separates. Also for larger pressure changes, the structures like the λ-foot are much wider and stronger. An example of the λ-foot is presented in Figure 2.1.
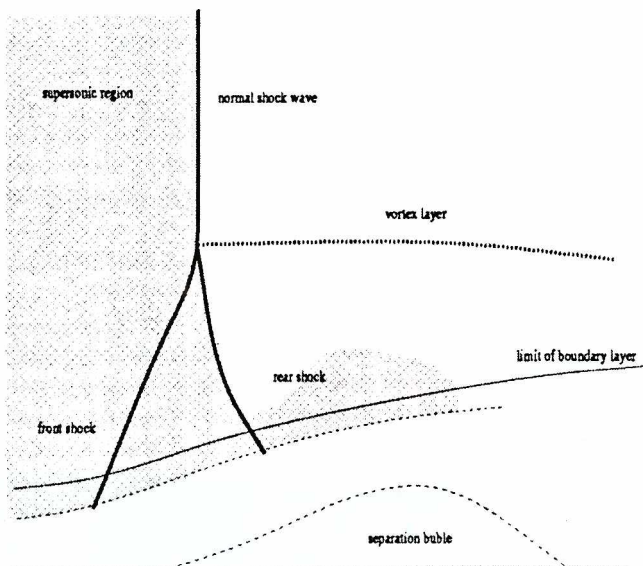
Figure 2.1. *The structure of the shock near the viscous wall. Grey area — supersonic region.*

The front oblique shock cross the normal shock dividing it to the normal shock and rear shock. At the triple point where this splitting occurs, the vortex layer is formed due to the different entropy production on a normal shock and λ-foot. The grey region in Figure 2.1 is supersonic.

The shock induced separation is very sensitive to the considered channel's geometry. Especially in the internal flows it is highly three-dimensional. This fact was confirmed by both experiments and computational results. In the case of the channel it was shown that the width of the channel had a large influence on the flow structure and separation size.

Due to this fact there was a necessity to compute three dimensional cases to check three-dimensional effects. The three-dimensional structures of separations are difficult to check with experiment. The computations will be compared with the experimental data presented in [45] and [46].

2.2 Flow in a nozzle

In this section the turbulent transonic three-dimensional flow in the nozzle will be presented. The main attention will be paid to the influence of the numerical schemes on the structures of the separation and λ-foot.

The geometry of the channel is given in Figure 2.2. For the computations the structural grid was generated. The number of mesh points on the highest level is $165\times65\times65$. The grid near the viscous wall is adequately chosen to render gradients within the turbulent boundary layer.

The computations were done using the Navier-Stokes solver **kappa** developed at Karlsruhe University and its open version is available at the Institute of Fluid Flow Machinery in Gda'nsk. More details about this solver are presented in [110].

The boundary conditions for this flow are: total pressure and temperature at the inlet and the static pressure at the outlet of the nozzle.

The computations were made for two different numerical schemes (slip and switch schemes) for turbulence model k-τ Launder Sharma [110]. More details about numerical schemes are available in Appendix C. To accelerate convergence the 3-level multigrid was used.

The difference in density for both schemes is shown in Figures 2.3. It can be seen that the difference occurs in the vicinity of the shock and is especially big where separation occurs for the switch scheme.
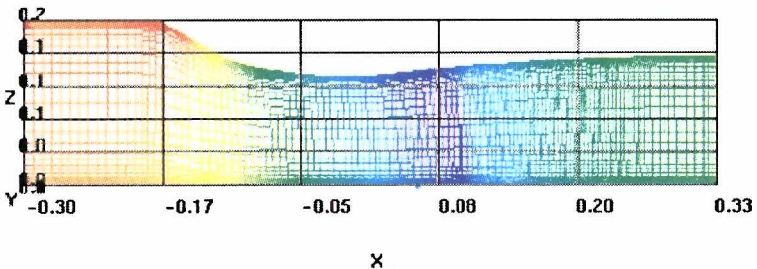
Figure 2.2. Mesh with the density distribution on the side wall. Flow direction is from left to right.
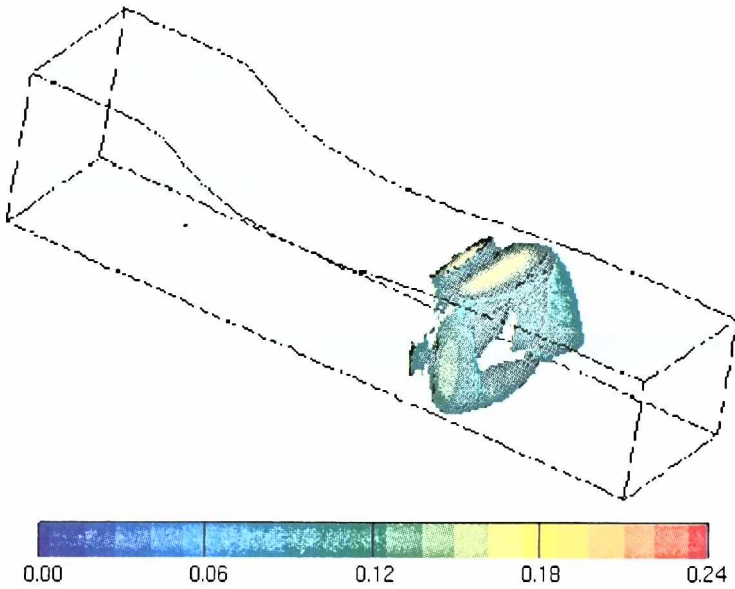
Figure 2.3. *Density difference between the switch and the slip scheme.*

Figures 2.4 and 2.5 present the Mach number isolines in the middle cross-section of the nozzle. The maximum Mach number in the case of the slip scheme is 1.44 and in the case of the switch scheme is 1.39 for the same boundary conditions. The difference again appears near the shock wave. For the slip scheme shock is stronger. As it was shown from experiments for stronger shock, the λ-foot is larger and also the separation region is longer but here there is no separation or λ-shock. Due to this fact the slip scheme will not be used for other cases although the convergence for this scheme is faster.
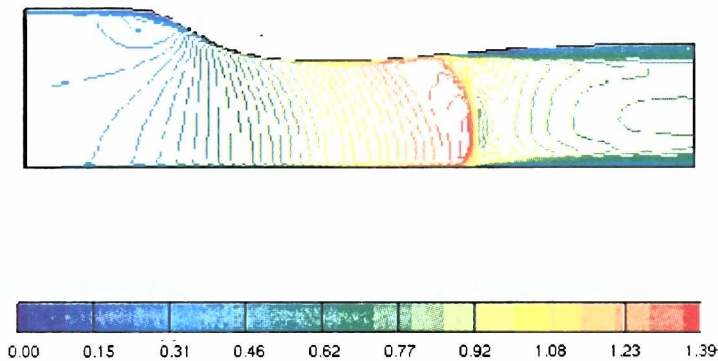
Figure 2.4. *Mach isolines for the switch scheme in the middle cross-section of the nozzle.*
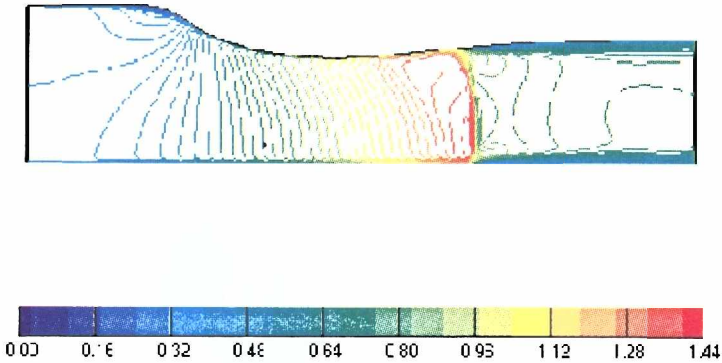
Figure 2.5. *Mach isolines for the slip scheme in the middle cross-section of the nozzle.*

In Figure 2.6 the l-foot near the bottom wall is presented. The grey region is the supersonic region. Mach isolines create a λ-foot only for the case of the switch scheme. Also it can be noted that there is a supersonic region spread downstream indicating an existence of a rear shock. The separation bubble is quite small, but still exists. The situation for the slip scheme is different — no separation and no λ-foot structure. The difference can be even easier noticed on the curved top wall of Figure 2.7. The λ-foot is very clear and also the supersonic area creates very characteristic structures like in Figure 2.1. In Figure 2.7 [a], for the switch scheme, the separation bubble is large and easy to notice. The case of the slip scheme again is different with no λ-foot or separation.

In Figure 2.8 the pressure distribution on the bottom wall in the middle of the nozzle is presented. The red curve presents pressure for the slip scheme and the green for the switch scheme. The difference downstream of the shock wave is caused by the presence of separation.
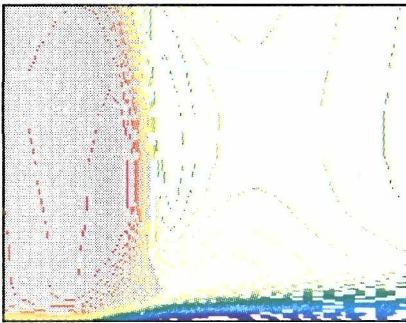
Figure 2.6 a
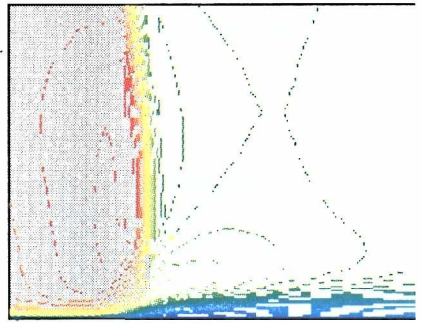
Figure 2.6 b

Figure 2.6. *Mach isolines for the switch [a] and slip [b] schemes in the middle cross-section of the nozzle near the bottom wall. The grey region is the supersonic region. In case [a] also the separation bubble can be seen.*

[a]   [b]
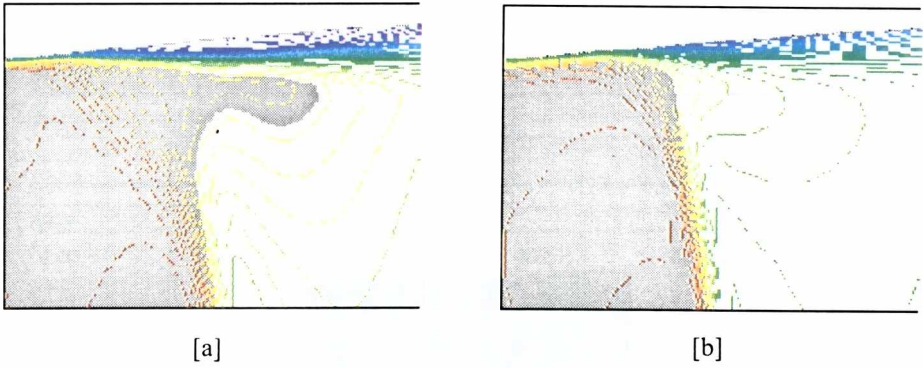
Figure 2.7. Mach isolines for the switch [a] and slip [b] schemes in the middle cross-section of the nozzle near the top wall. The grey region is the supersonic region. In case [a] also the separation bubble can be seen as well the supersonic region extends far downstream from the shock.

The conclusion of this section is that, for the computations of the turbulent boundary layer shock wave interaction, the switch scheme gives more acceptable results that are closer to experiment. To explain the differences in obtained results it is necessary to know a basic description of the schemes. The explanation of the differences between schemes can be found in Appendix C. Also in Appendix C, the possible reason for the results is presented.
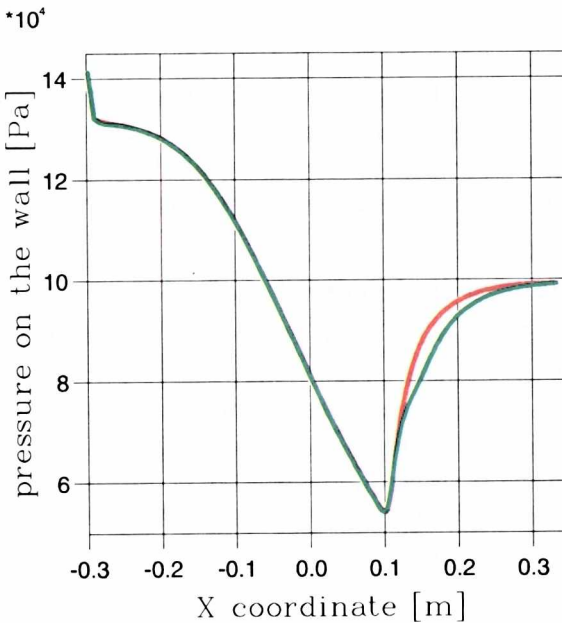
Figure 2.8. Pressure distribution on the bottom wall in the middle of the nozzle. Red curve — slip scheme, green curve — switch scheme.

[a]   [b]

[c]
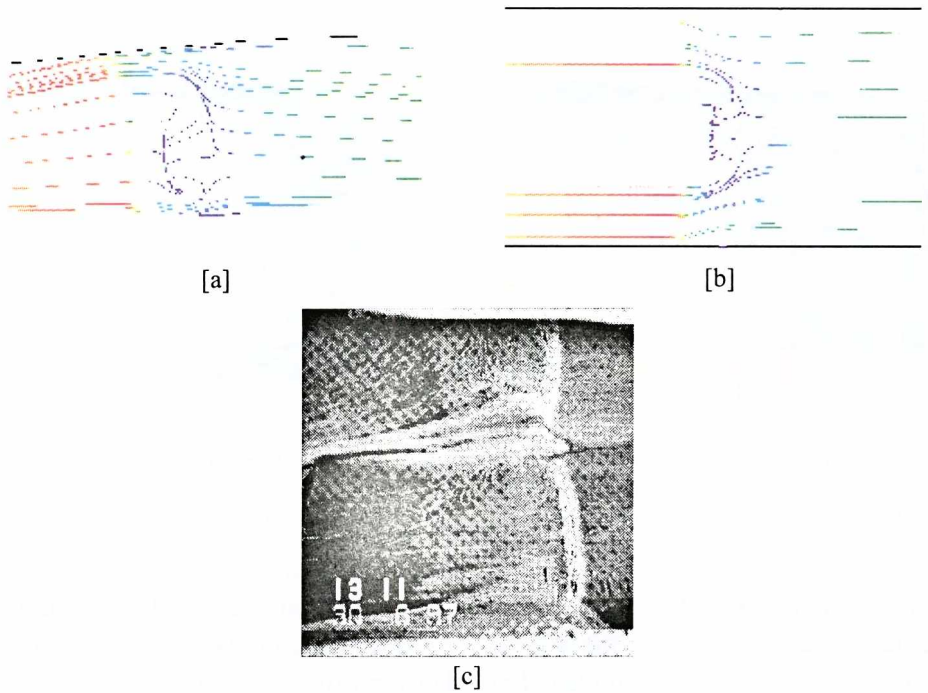
Figure 2.9. *Comparison between numerical calculations and experiments. Structures of the separation on [a] the side and [b] bottom wall for switch scheme. [c] The oil visualization for the similar case, the flow on the photograph is in the opposite direction to that in Figure [a] and [b]. The oil visualization is for $M_{is} = 1.47$ and numerical calculation for $M_{is} = 1.40$. This explains differences in the size of the region of separation.*

Figure 2.9 presents the comparison between the experimental visualization and the numerical computations. The experimental picture presents the oil visualization. The flow direction is from right to left, opposite that of computations. The velocity vector plot for the switch scheme presents very similar results to experiment. On the side wall the vortex can be seen. There is also the separation region on the bottom wall.

2.3 Two-dimensional flow in the curved channel

In a nozzle the shock wave spans across the whole channel and induces separation at all walls. Therefore such a flow case is very complex as far as separation structures are concerned. Due to this it was decided to investigate a curved passage flow. In such a case the supersonic region is adjacent to the convex wall and the shock wave is strong at this wall. In consequence the shock induced separation takes place only at the convex wall. Moreover there is sufficient experimental data for validation.

This section will be devoted to two-dimensional computations of transonic flow in a curved channel. The main aim of this section is to estimate the basic flow character in 2-D so that later it can be compared with similar computations for three dimensional flows.
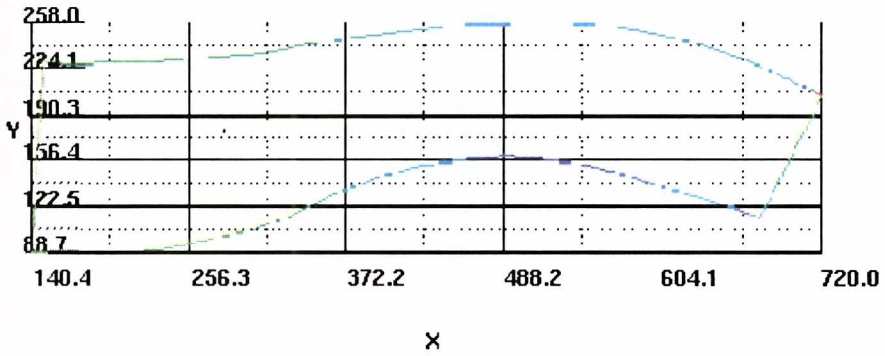
Figure 2.10. *The geometry of the curved channel.*

The geometry of the channel is given in Figure 2.10. The number of points in the grid for this case is 257×193.

The computations were performed for two different isentropic Mach numbers just upstream the interaction: $M_{is} = 1.35$ and $M_{is} = 1.47$ on the bottom wall, where the isentropic Mach number is defined as follow:

$$M_{is} = \sqrt{\frac{2}{\kappa - 1}\left[\left(\frac{p_0}{p}\right)^{\frac{\kappa-1}{\kappa}} - 1\right]}. \tag{2.1}$$

The required isentropic Mach number was obtained by the change of the outlet boundary condition — value of the pressure ratio.

The numerical schemes used for both cases were the slip and switch scheme. Due to difficulties (presented in the previous section) with the slip scheme to render the separation in the 3-D nozzle, it was necessary to check if for a very refine grid in 2-D such difficulties also existed. The turbulence model was the non-linear k-τ of Craft, Launder and Suga [22]. To obtain better convergence, a 3 level multigrid was used.
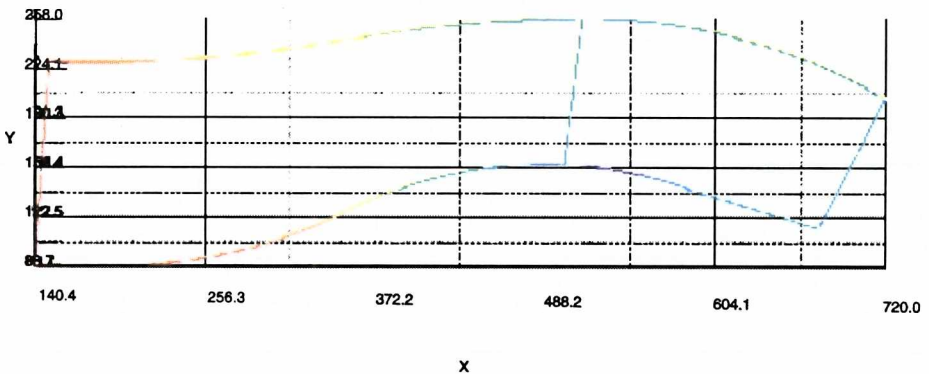
Figure 2.11. *The position of the cut with the geometry of the channel for an isentropic Mach number $M_{is} = 1.47$. The line perpendicular to the channel indicates the cut line.*

In Figure 2.11 the cut position in the channel is shown. At this position the boundary layer profiles have been studied. The velocity profiles for $M_{is} = 1.47$ in Figure 2.12 are presented. The figure shows profiles for the bottom and top wall. It proves that for the slip scheme the boundary layer is thicker. Table 2.1 shows the maximum velocities and boundary layer thickness for these cases. The boundary layer thickness was taken at a point where, $u / u_{inf} = 0.995$.
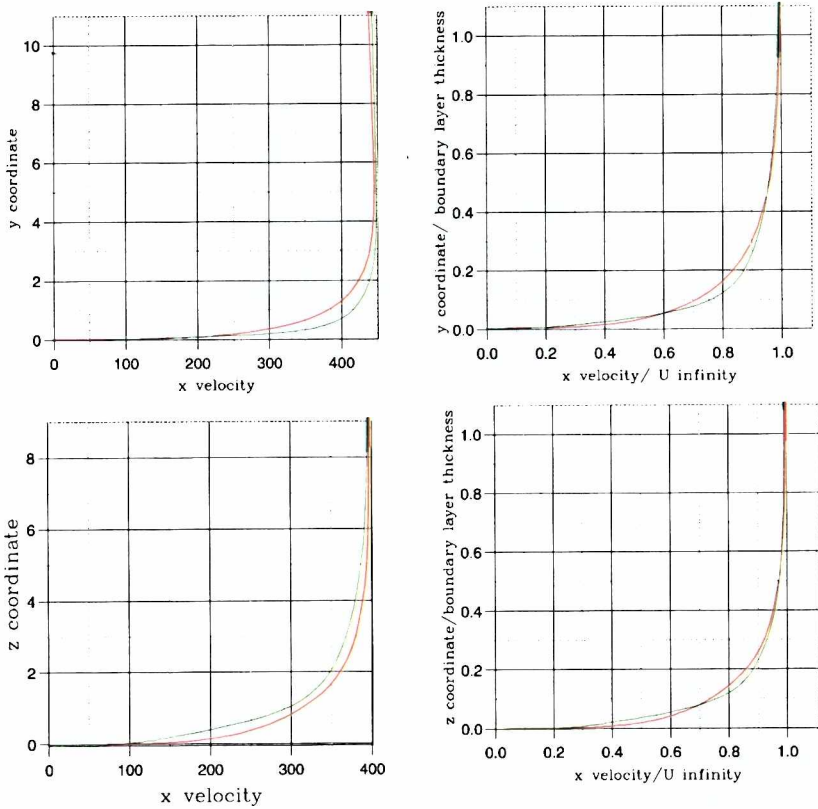
Figure 2.12. Velocity profiles; green — switch scheme, red — slip scheme; [a] Without normalization on bottom wall, [b] Normalized on bottom wall, [c] Without normalization on top wall, [d] Normalized on top wall.

Table 2.1. Boundary layer thickness for the slip and switch schemes.

scheme	max.velocity bottom	boundary layer thickness — bottom	max.velocity top	boundary layer thickness — top
switch	366 m/s	2.5 mm	318 m/s	4.5 mm
slip	368 m/s	3.5 mm	313 m/s	5.0 mm
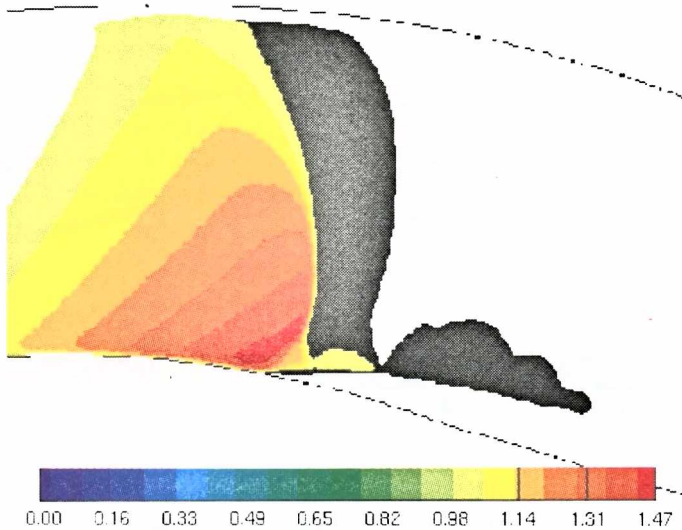
Figure 2.13. *Comparison between two schemes. Color contour (M > 1) — switch scheme. Black — slip scheme.*

In Figure 2.13 the comparison between two schemes for $M_{is} = 1.47$ is shown. It again can be seen that the λ-foot is larger for slip scheme.

Similar to the previous section, it can be seen that slip scheme has a different dissipation near the shock and predicts a bit different position for the shock and its strength. It seems though that the behavior of the schemes is independent of the turbulence modeling. The tendency is the same although in the previous section another turbulence model was used. Tatsumi, Martinelli and Jameson [172] have shown that for both schemes the parameters in the boundary layer are different and with growing points number within the boundary layer one cannot give a clear answer which scheme gives the better results. For cases computed here the switch scheme seems to be more accurate giving better agreement with experimental data considering the separation structures and the λ-foot size in three-dimensional computations.

Due to this fact, for further comparison, the switch scheme was used. In Figure 2.14 the Mach number isolines for isentropic Mach number $M_{is} = 1.35$ and $M_{is} = 1.47$ are presented. From this picture, changes in the position of the shock can be seen and also that the λ-foot structure changes with Mach number. The λ-foot is much smaller for lower Mach number.

In Figure 2.15 the pressure distribution on the bottom wall is shown. From this figure it can be noted again that the position of the shock and pressure drops are different for the two cases.

The separation bubble can be seen on the vector plot in Figure 2.16. The size of the separation bubble is for $M_{is} = 1.35$ — 18 mm, for $M_{is} = 1.47$ — 27 mm. The λ-foot height respectively 10 mm, 18 mm.

The two-dimensional results presented in this section are an introduction to the three dimensional flow computations in the same geometry of the channel.

| 0.00 | 0.15 | 0.30 | 0.46 | 0.61 | 0.76 | 0.91 | 1.06 | 1.21 | 1.37 |

[a]

| 0.00 | 0.16 | 0.33 | 0.49 | 0.66 | 0.82 | 0.99 | 1.15 | 1.32 | 1.48 |

[b]
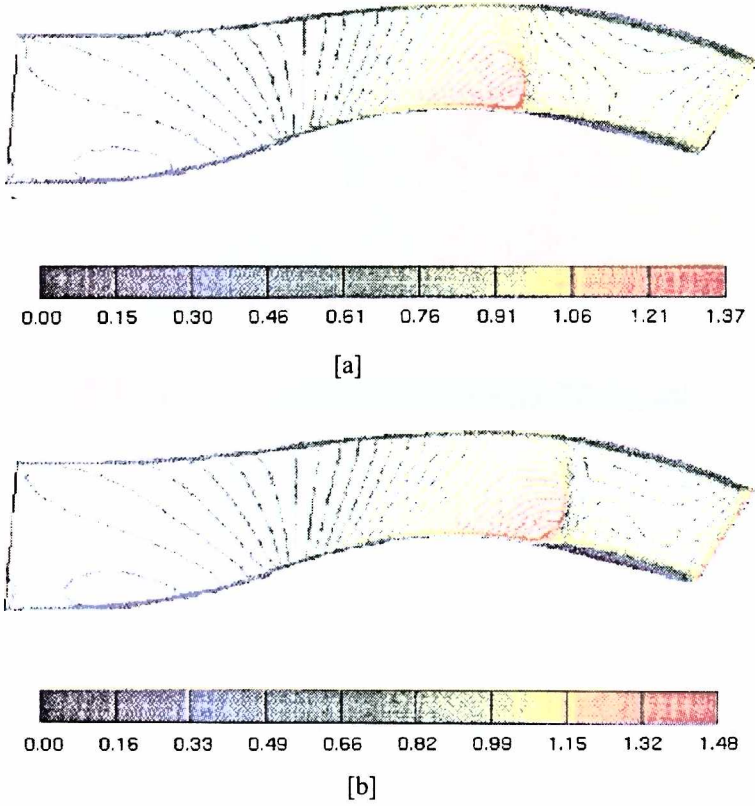
Figure 2.14. Mach number isolines in curved two-dimensional channel. [a] $M_{is} = 1.35$ [b] $M_{is} = 1.47$.
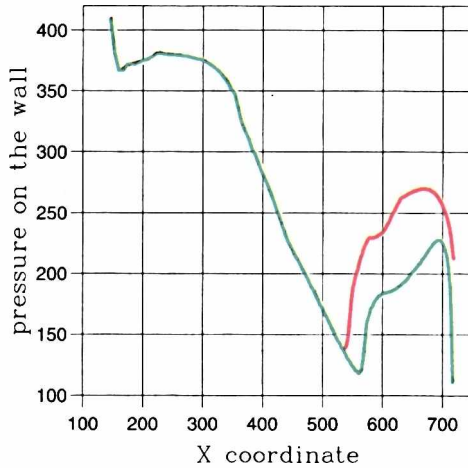
Figure 2.15. Pressure distribution on the wall. Red curve — $M_{is} = 1.35$, green — $M_{is} = 1.47$.

[a]   [b]
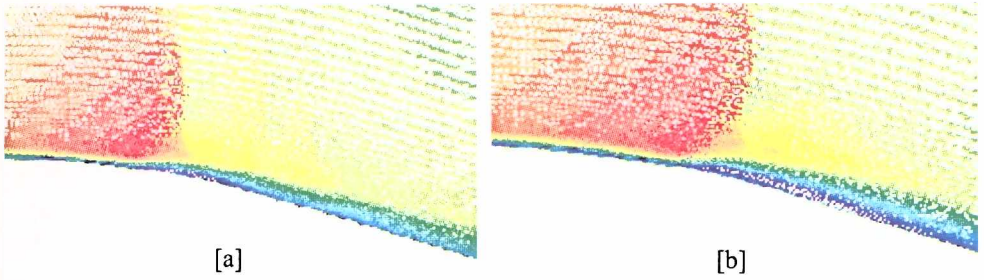
Figure 2.16. *Velocity vector plots near the bottom wall. [a] M_{is}= 1.35, [b] M_{is}= 1.47.*

2.4 Three-dimensional flow in the curved channel. Effect of width of the channel

The geometry of the channel is the same as in Figure 2.10. The third dimension has been added while taking into account two different widths of the channel: 150 mm (later it will be called the wide channel) and 50 mm (called the narrow channel). The number of mesh points is 129×97×65. The symmetry condition was

[a]

[b]
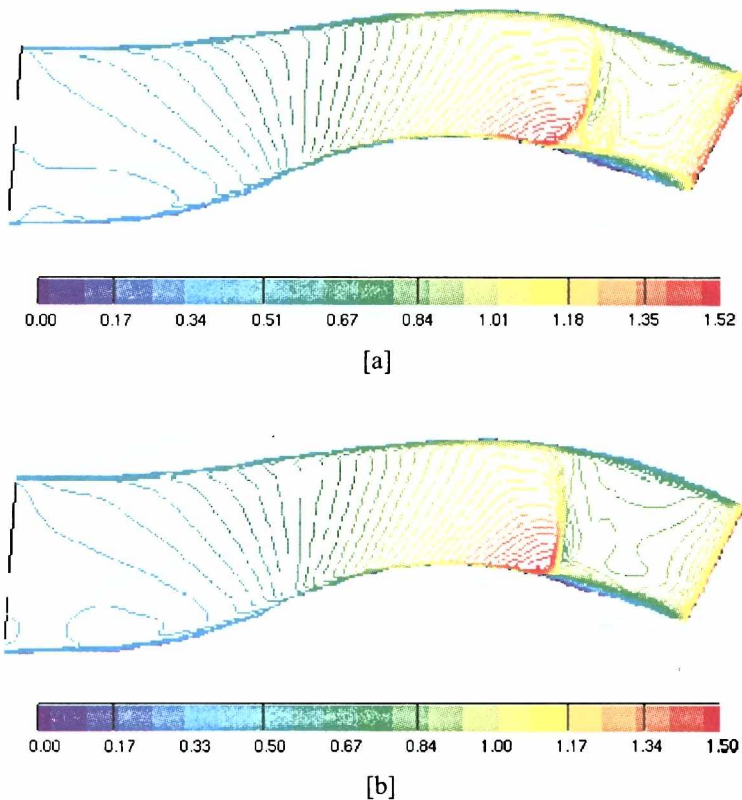
Figure 2.17. *Mach number isolines in curved three-dimensional channel for M_{is}=1.47 [a] narrow channel [b] wide channel.*

used, but also whole channel has been calculated for grid 129×97×97. The computations were done using the switch scheme which behaves more accurately in the separation region. The turbulence model used in the computations was the non-linear k-τ model of Craft-Launder and Suga [22].

In Figure 2.17 the Mach number isolines for $M_{is} = 1.47$ in the middle cross-section of the channel are presented. Figure [a] shows the distribution for the narrow channel and [b] for the wide one. The shock wave structure in both cases is very different. For the wide channel the λ-foot is much smaller and also the separation is smaller. This is in reference to the boundary layer thickness. For the narrow channel a second smaller shock also appears. It will be shown later that such structures are also present in experiment. The position of the shock is nearly the same, which can be also noticed from Figure 2.45 [a] and 2.47 [a].

In Figure 2.18 the Mach number isolines for $M_{is} = 1.35$ in the middle cross-section of the channel are presented. The shock waves for lower Mach numbers are of course weaker and the λ-foot is much smaller than for $M_{is} = 1.47$ but still the difference between the wide and narrow channel can be seen. Again, in the narrow channel, the second smaller shock wave has appeared, although very weak.

[a]

[b]
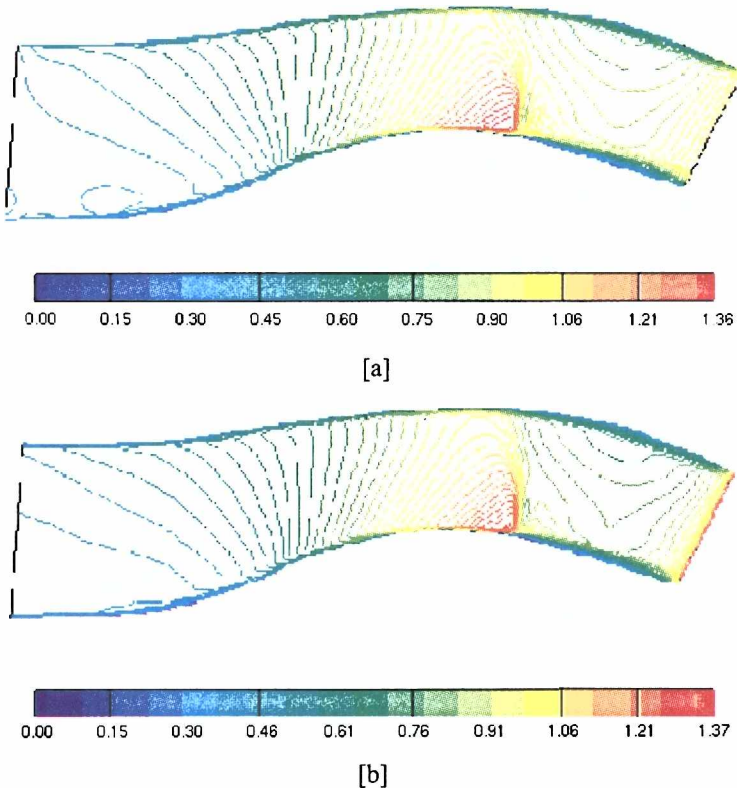
Figure 2.18. Mach number isolines in curved three-dimensional channel for $M_{is} = 1.35$
[a] narrow channel [b] wide channel.

The next sections will provide details concerning flows in these two channels. There will be a study of the boundary layer influence, shock wave structures and also separation structures. Also the width of the channel, as well as the changes due to the growing Mach number will be taken into account.

2.4.1. Boundary layer profiles

In this section the main attention will be paid to describing basic parameters of the boundary layer for all computed cases. The boundary layer parameters influence the λ-foot structure and also the separation further downstream from the shock. The investigation of the boundary layer will be done upstream of the shock to check what is the influence of the boundary layer for the wide and narrow channel.

In Figure 2.19 the location of the cut for the isentropic Mach number $M_{is} = 1.47$ where the boundary layer has been checked is shown.

Figure 2.20 shows the location for $M_{is} = 1.35$. The cut is made in the grid points so that locally near the wall it is perpendicular to the wall. Due to this fact, the velocity is parallel to the wall (in the boundary layer without separation) so changes in velocity occur mainly in the y-direction. Changes in the perpendicular velocity are much smaller at around 1/100 of x-velocity. This confirms the assumption used below that profiles of the boundary layer are studied based on the x-velocity distribution, although there is some curvature of the channel.
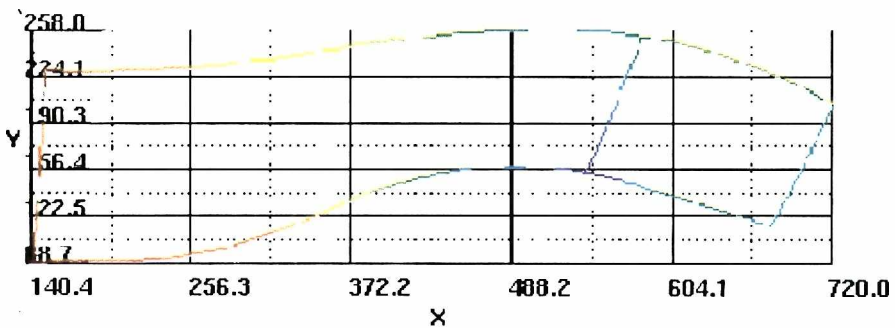
Figure 2.19. *The location of cut with the geometry of the channel for isentropic Mach number $M_{is} = 1.47$.*
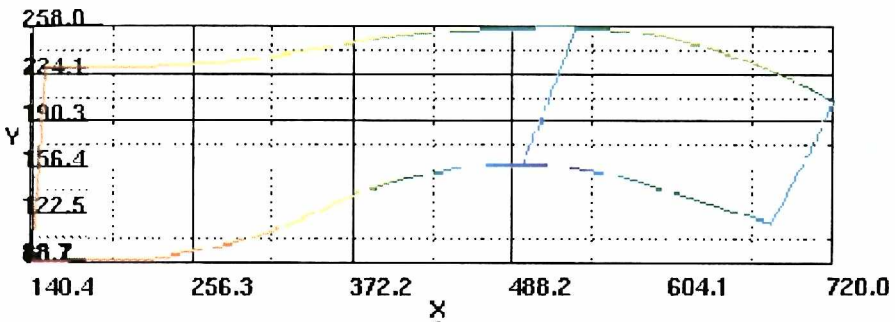
Figure 2.20. *The location of cut with the geometry of the channel for isentropic Mach number $M_{is} = 1.35$.*

In Figure 2.21 the velocity profiles within the boundary layer for $M_{is} = 1.47$ are presented.

Figure 2.22 presents the velocity profiles for $M_{is} = 1.35$. The velocity profiles are obtained for cuts presented in Figure 2.19 and 2.20.

Figures 2.21 and 2.22 present velocities for the bottom, side and top wall. The green line corresponds to velocity in the wide channel while respectively the red line corresponds to the narrow channel. The velocity is normalized to velocity in infinity and the y-coordinate to the boundary layer thickness (see Table 2.2). The boundary layer thickness is different for $M_{is} = 1.47$ for different widths of the channel although the character remains the same.

In Table 2.2 the maximum velocities and boundary layer thickness for both widths of the channel are presented. The maximum velocities are about the same on the side and bottom wall. The biggest difference is present on the top wall for high Mach number. Also for high Mach number the difference in the boundary layer thickness for a side wall is large. For all cases, two different Mach numbers and two different widths of the channel, the condition on the isentropic Mach number in the middle of the channel on the bottom wall was the basic requirement. Due to this the outlet conditions were different. This can explain why there are differences on the side wall boundary layer and the maximum velocity.

Table 2.2.   *Maximal velocity and boundary layer thickness for wide and narrow channel for $M_{is} = 1.47$ and $M_{is} = 1.35$.*

	bottom $M_{is}=1.47$	side $M_{is}=1.47$	top $M_{is}=1.47$	bottom $M_{is}=1.35$	side $M_{is}=1.35$	top $M_{is}=1.35$
maximal velocity wide channel	451 m/s	400 m/s	320 m/s	396 m/s	367 m/s	336 m/s
maximal velocity narrow channel	448 m/s	399 m/s	360 m/s	401 m/s	372 m/s	332 m/s
boundary layer thickness wide channel	3.1 mm	11 mm	6.9 mm	4.2 mm	7 mm	7.5 mm
boundary layer thickness narrow channel	4.5 mm	7.5 mm	7.1 mm	4.2 mm	6.5 mm	7.5 mm

Considering Figures 2.17 and 2.18 and Table 2.2 the dependence between the boundary layer thickness and the height of the λ-foot can be noticed. This will be investigated further in the next subsection.
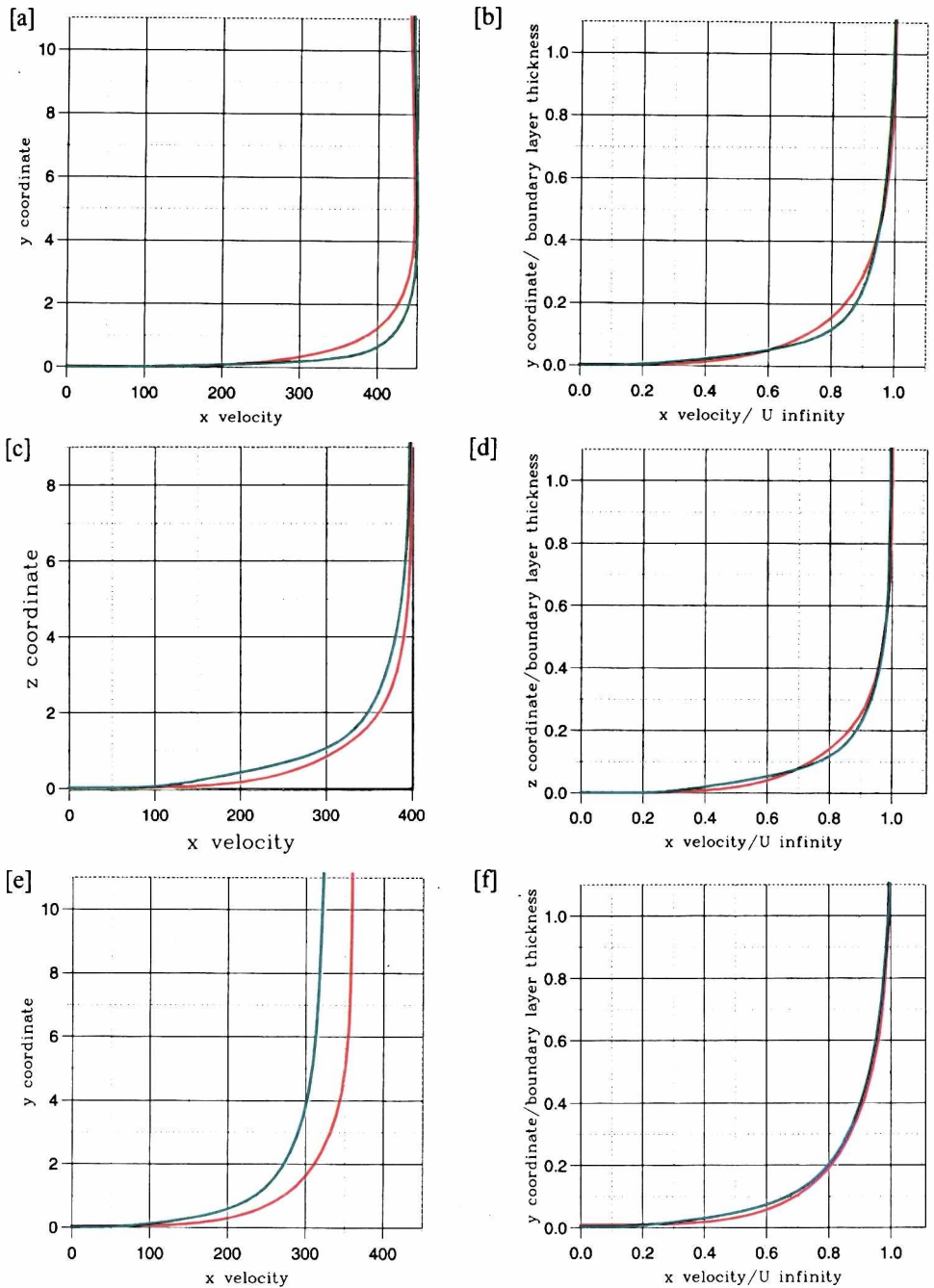
Figure 2.21. *Velocity profiles for $M_{is} = 1.47$; green -wide channel, red - narrow channel [a] Without normalization on bottom wall, [b] Normalized on bottom wall, [c] Without normalization on side wall, [d] Normalized on side wall, [e] Without normalization on top wall, [f] Normalized on top wall.*
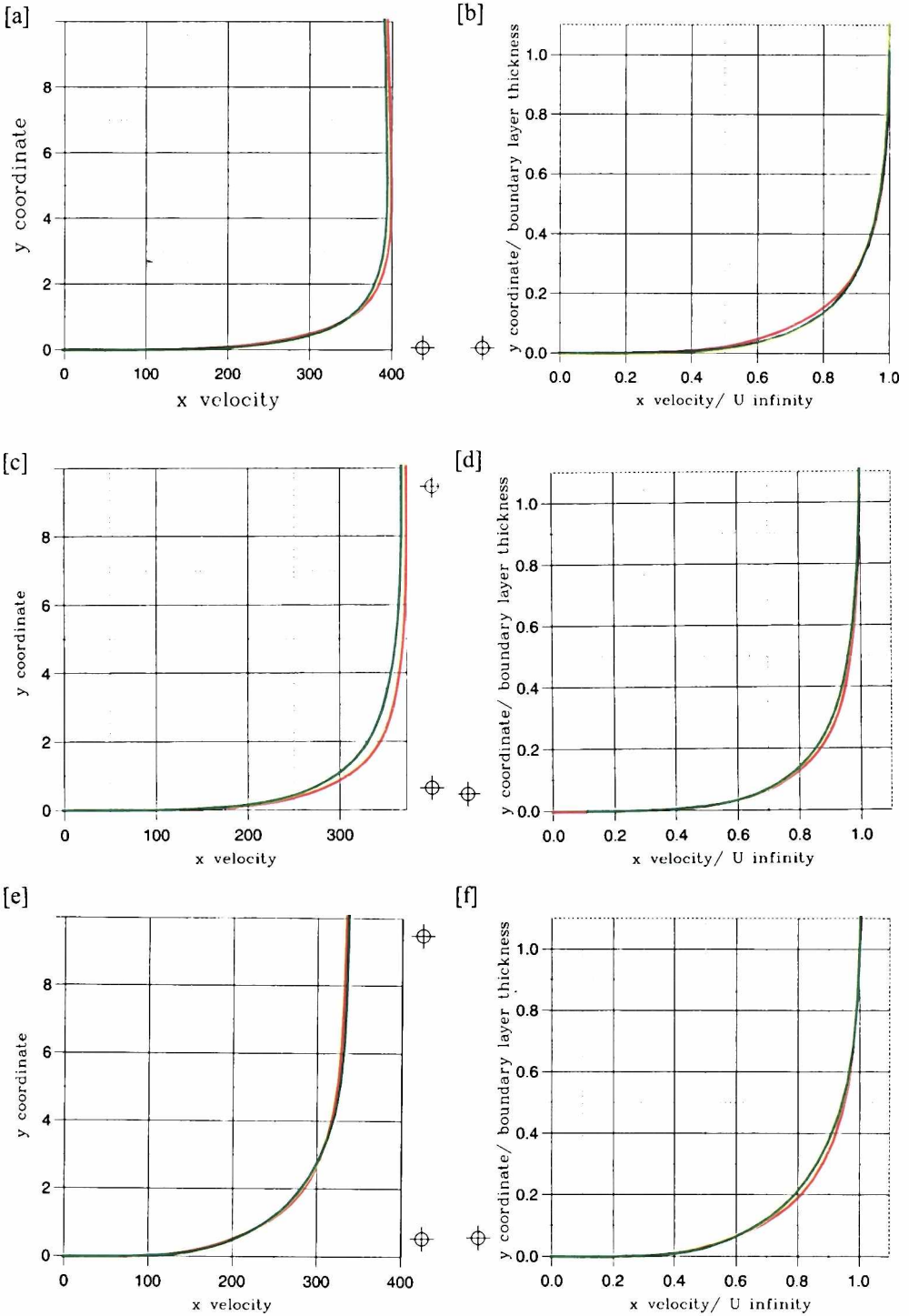
Figure 2.22. Velocity profiles for $M_{is} = 1.35$; green — wide channel, red — narrow channel [a] Without normalization on bottom wall, [b] Normalized on bottom wall, [c] Without normalization on side wall, [d] Normalized on side wall, [e] Without normalization on top wall, [f] Normalized on top wall.

2.4.2 The shock wave characteristic

Figures 2.23-2.28 show the flow region near the shock wave for both channels with $M_{is} = 1.47$. The grey area is the supersonic region (M > 1). Cuts are done in the grid points and the numbers associated with them represent the node numbers that correspond to the distance from the side wall. Table 2.3 shows the position of these nodes in the wide and narrow channel.

Table 2.3. *Node positions for the wide and narrow channels. The table presents the node numbers and corresponding positions from the side wall.*

node	wide channel [mm]	narrow channel [mm]
38	2.9519	0.9643
40	3.8105	1.2452
42	4.9156	1.6069
44	6.3369	2.0725
46	8.1637	2.6715
48	10.5091	3.4415
50	13.5167	4.4393
52	17.3670	5.6985
54	22.2856	7.3226
56	28.5521	9.3979
58	36.5086	12.0430
60	46.5667	15.4031
62	59.2119	19.6531
64	75.0000	25.0000

Figures 2.23-2.28 allow the study of both the changes in the separation region size and the λ-foot structure. The λ-foot is smaller for the wide channel. For the narrow channel, a smaller second shock can be seen. The flow is supersonic in the entire region upstream the shock. From Table 2.3 and the following Figures, it can also be concluded that the shock penetrates the boundary layer near the side wall. Another result from analysis of the figures is that for the narrow channel, the position of the shock changes more with the cut position than for the wide channel.

Figures 2.29-34 show the same cuts but for $M_{is} = 1.35$. It can be seen here that the λ-foot is similar for the two channel types. In addition, the supersonic region is smaller than for higher Mach number, and for the narrow channel, the second smaller shock exists. In the case of a small isentropic Mach number, the supersonic region for the narrow channel only exists near the shock.
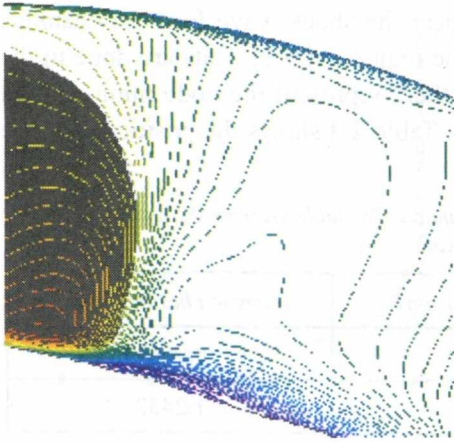
Figure 2.23 a
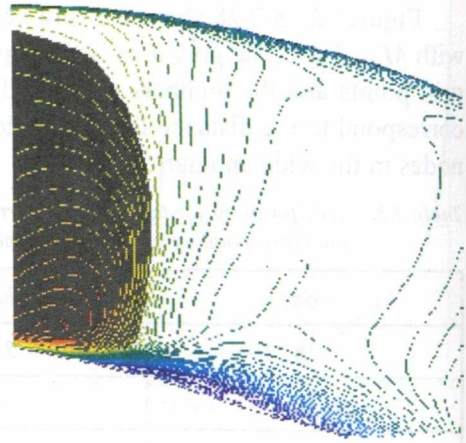
Figure 2.23 b
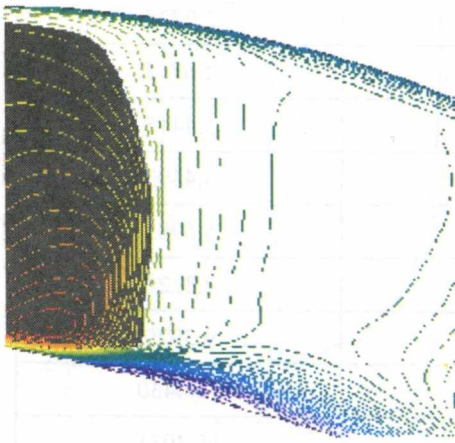
Figure 2.23 c
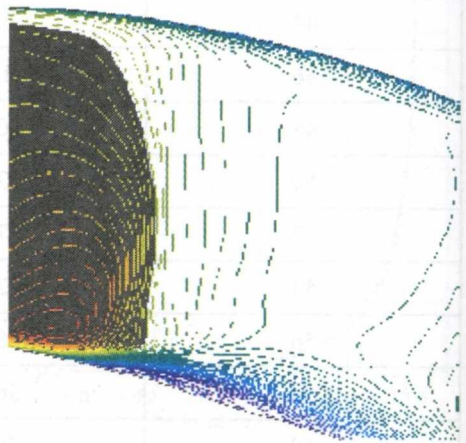
Figure 2.23 d
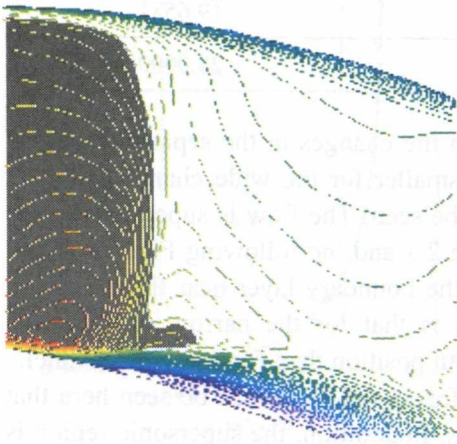
Figure 2.23 e
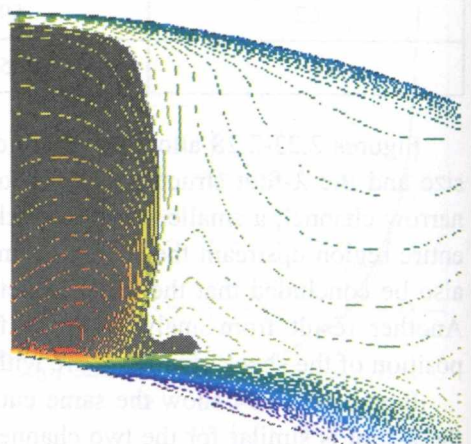
Figure 2.23 f

Figure 2.23. *Mach isolines for $M_{is} = 1.47$ for the wide channel [a] 38, [b] 40, [c] 42,*
[d] 44, [e] 46, [f] 48.
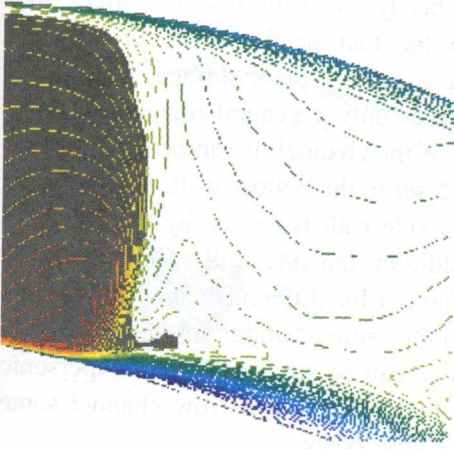
Figure 2.24 a
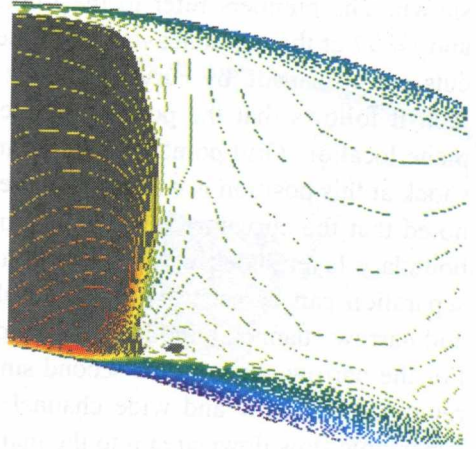
Figure 2.24 b
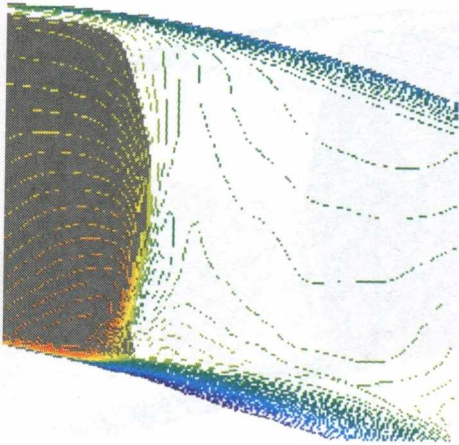
Figure 2.24 c
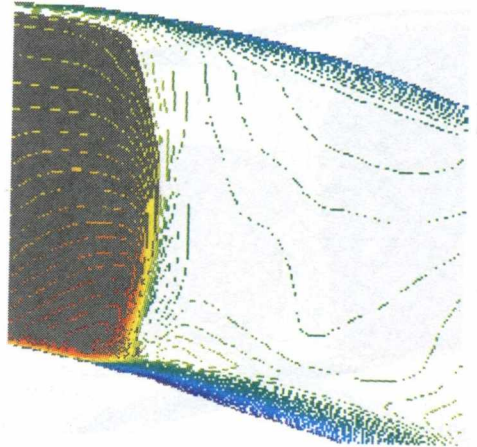
Figure 2.24 d
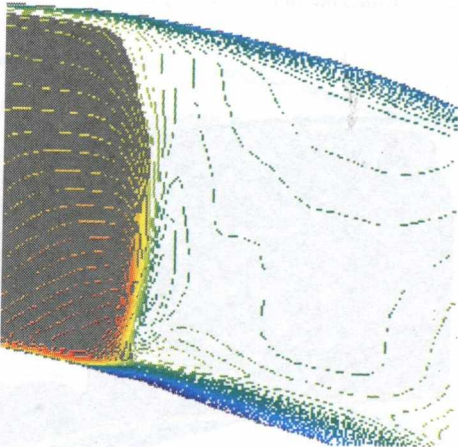
Figure 2.24 e
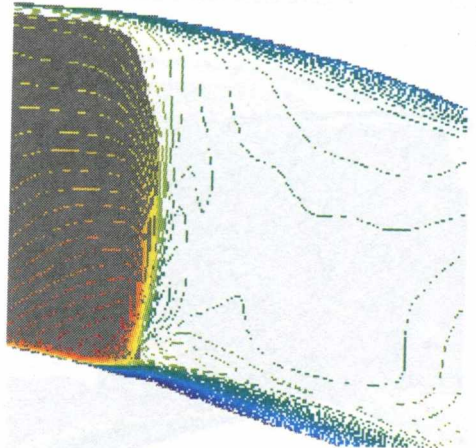
Figure 2.24 f

Figure 2.24. *Mach isolines for $M_{is} = 1.47$ for the wide channel [a] 50, [b] 52, [c] 54, [d] 56, [e] 58, [f] 60.*

In Figures 2.35-2.40 the Mach isolines for the spanwise-streamwise cuts are shown. The numbers refer to the j-node number ($j = 1$ at the bottom convex wall and $j = 97$ at the top concave wall). Due to the fact that the channel is curved, these cuts are also made by curved surfaces projected onto a plain surface. Noting this fact, it follows that the position of the cut gives only a general orientation about plane location. Grid point 48 is in the middle of the channel. It can be seen that the shock at this position is weaker than the one closer to the bottom wall. It can also be noted that the curvature of the shock near the side wall is caused by the side wall boundary layer shock wave interaction. In addition, the side wall structures of the separation can be seen. The Mach isolines have a bit different behavior for wide and narrow channel, although cuts are done in the same positions for both channels. For the narrow channel, the second small shock can be seen again. The supersonic regions for narrow and wide channel are different. For the narrow channel some supersonic flow downstream to the main shock also exists.

[a]   [b]
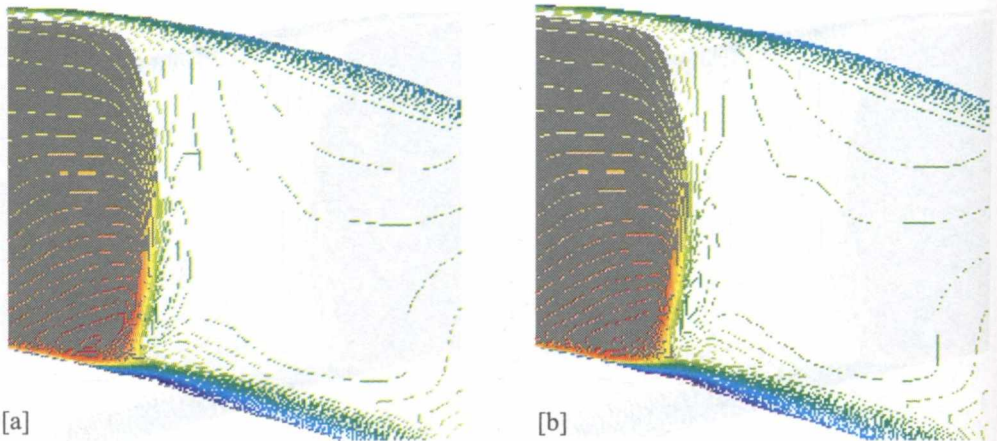
Figure 2.25. *Mach isolines for $M_{is} = 1.47$ for the wide channel [a] 62, [b] 64.*

[a]   [b]
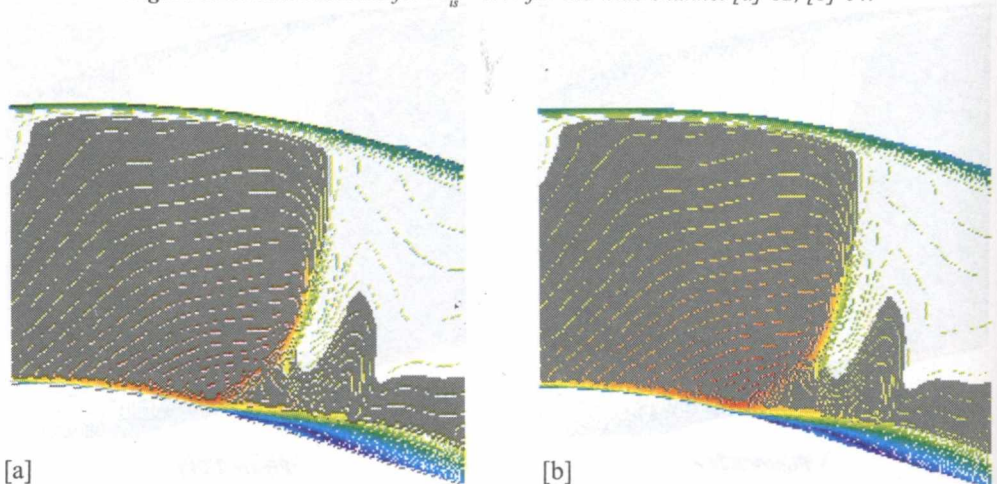
Figure 2.26. *Mach isolines for $M_{is} = 1.47$ for the narrow channel [a] 62, [b] 64.*
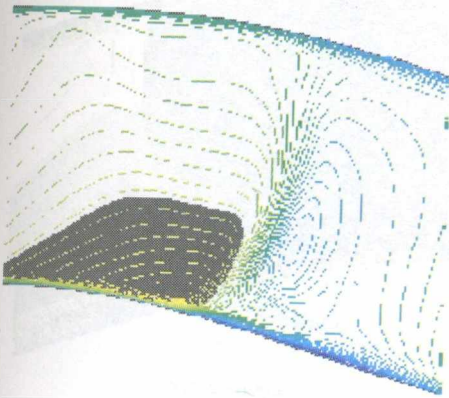
Figure 2.27 a
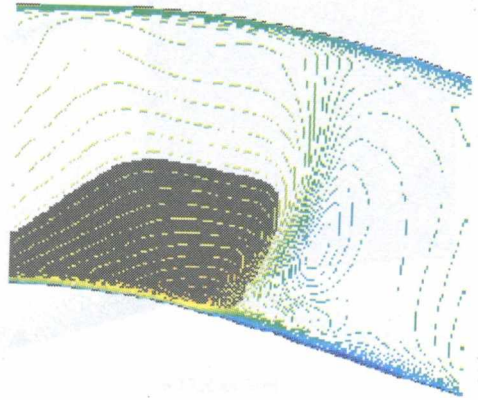
Figure 2.27 b
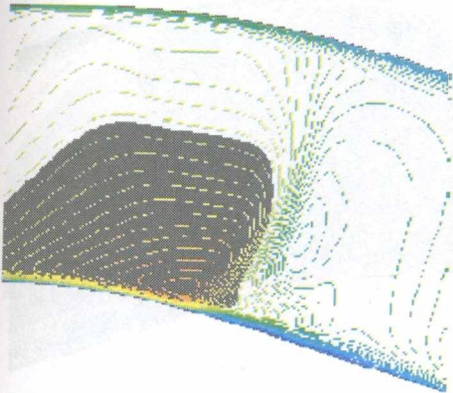
Figure 2.27 c
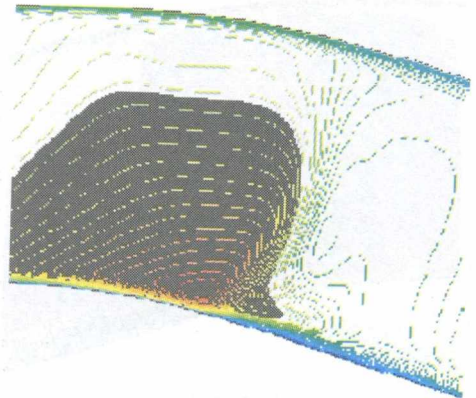
Figure 2.27 d
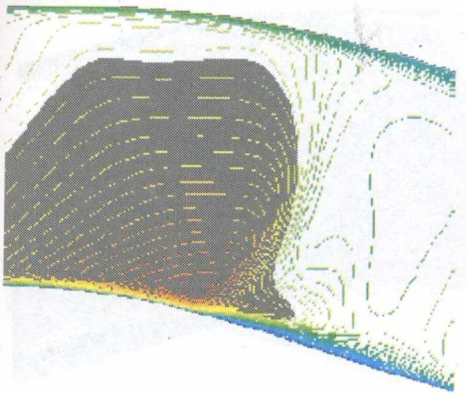
Figure 2.27 e
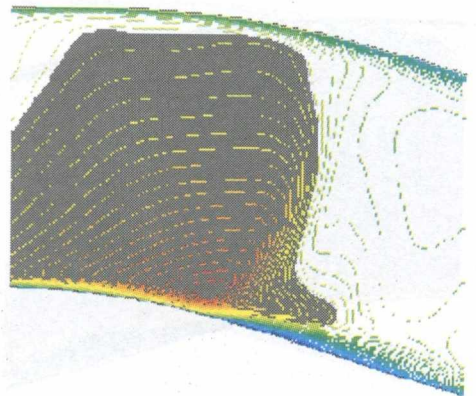
Figure 2.27 f

Figure 2.27. *Mach isolines for M_{is} = 1.47 for the narrow channel [a] 38, [b] 40, [c] 42, [d] 44, [e] 46, [f] 48.*
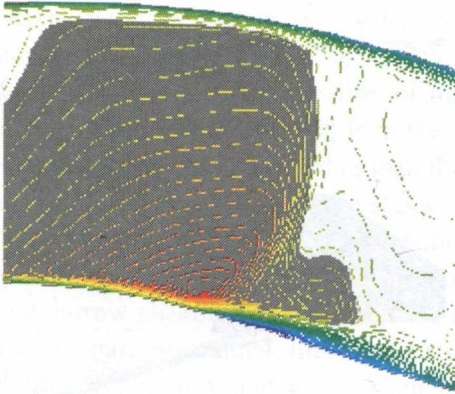
Figure 2.28 a
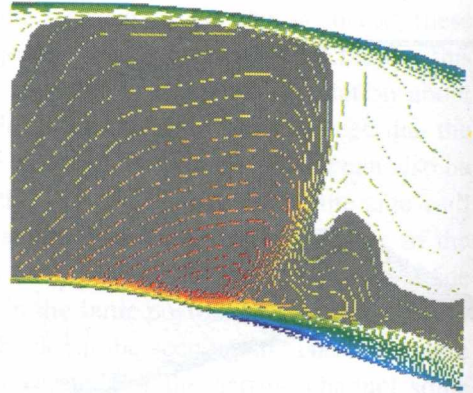
Figure 2.28 b
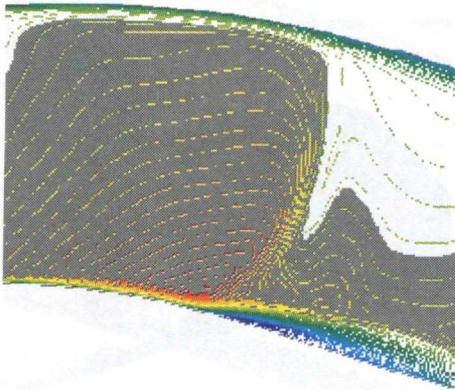
Figure 2.28 c
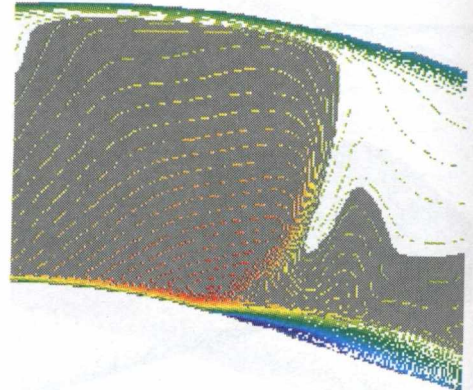
Figure 2.28 d
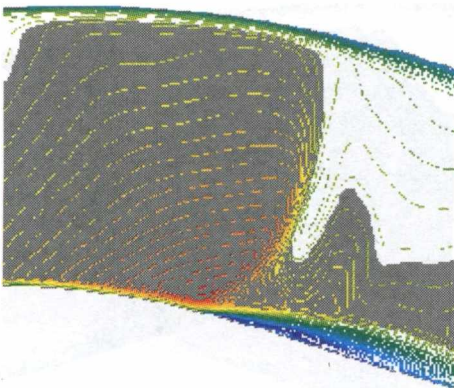
Figure 2.28 e
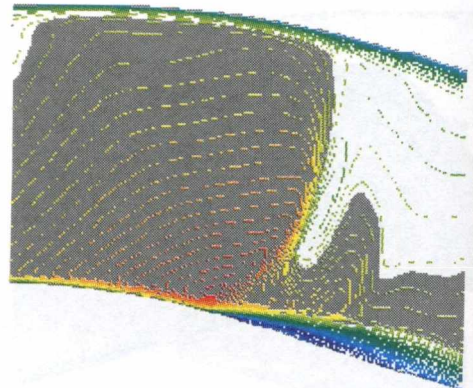
Figure 2.28 f

Figure 2.28. *Mach isolines for $M_{is} = 1.47$ for the narrow channel [a] 50, [b] 52, [c] 54, [d] 56, [e] 58, [f] 60.*
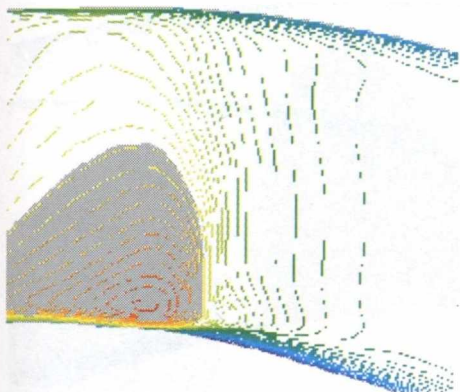
Figure 2.29 a
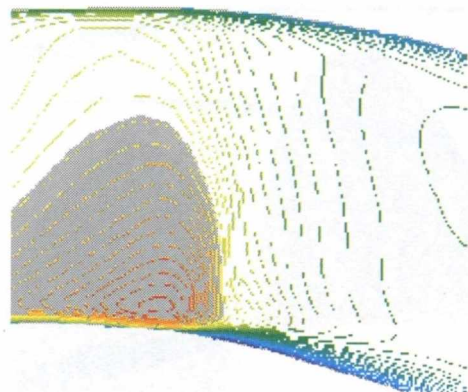
Figure 2.29 b
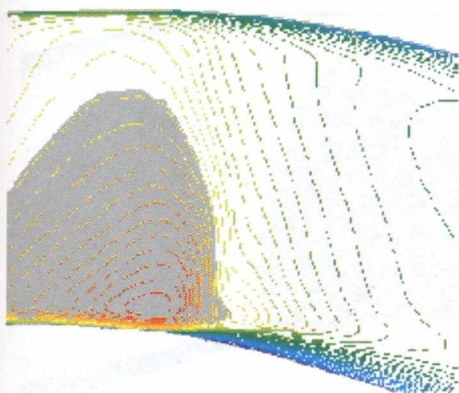
Figure 2.29 c
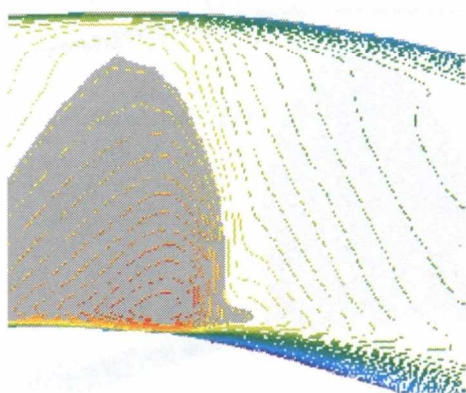
Figure 2.29 d
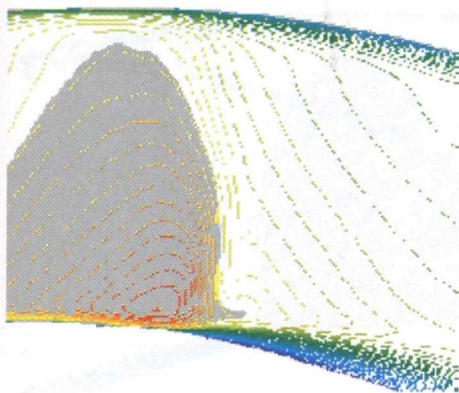
Figure 2.29 e
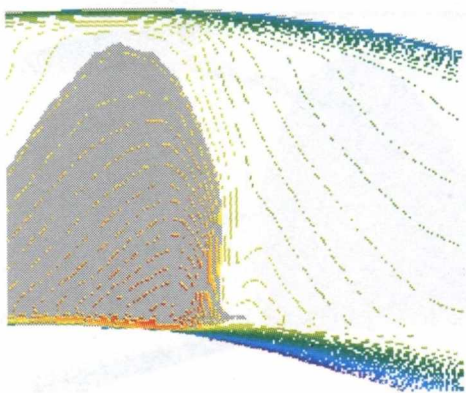
Figure 2.29 f

Figure 2.29. *Mach isolines for $M_{is} = 1.35$ for the wide channel [a] 38, [b] 40, [c] 42, [d] 44, [e] 46, [f] 48.*
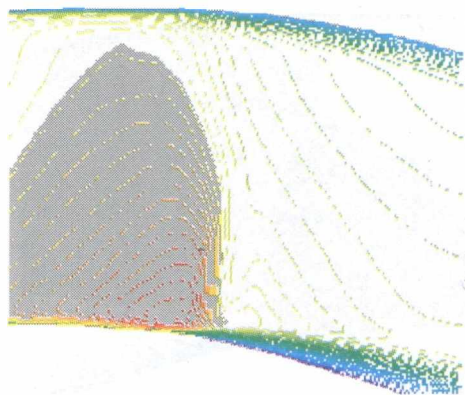
Figure 2.30 a
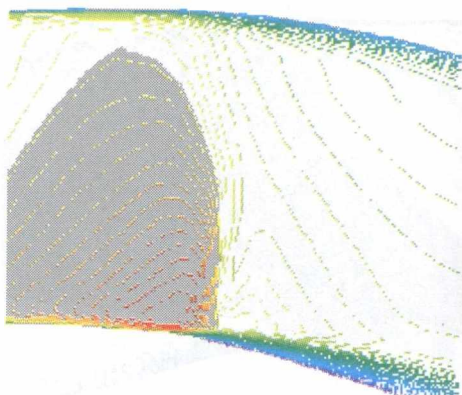
Figure 2.30 b
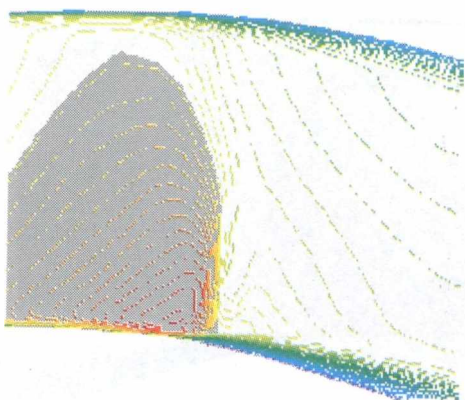
Figure 2.30 c
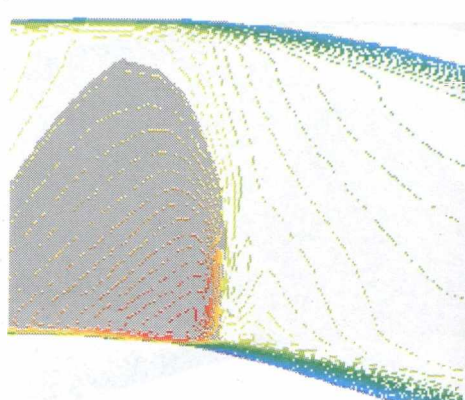
Figure 2.30 d
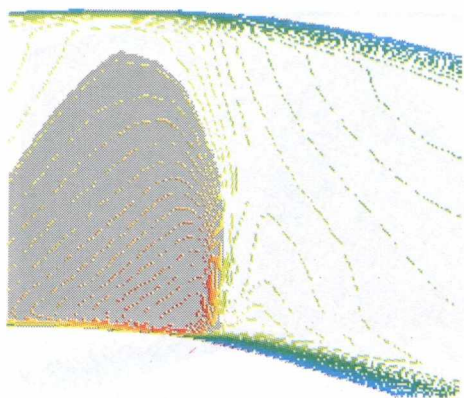
Figure 2.30 e
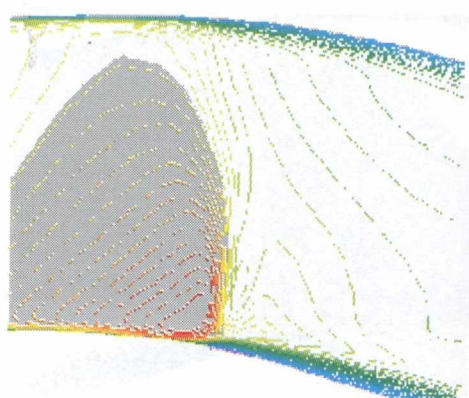
Figure 2.30 f

Figure 2.30. Mach isolines for $M_{is} = 1.35$ for the wide channel [a] 50, [b] 52, [c] 54, [d] 56, [e] 58, [f] 60.
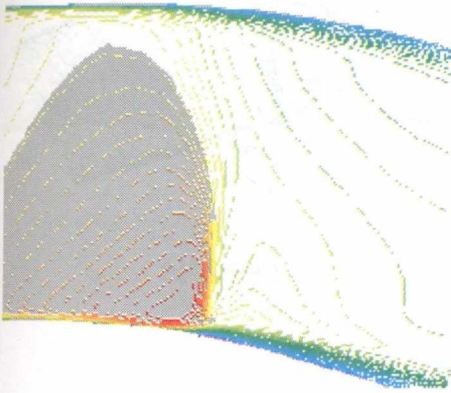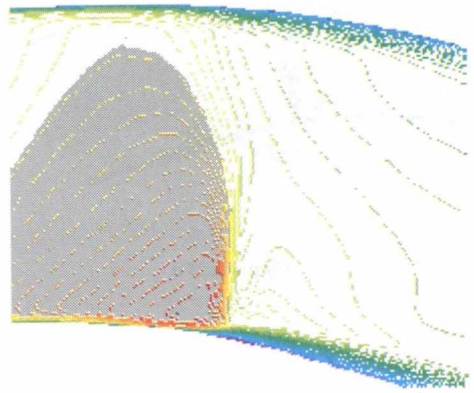
Figure 2.31 a   *Figure 2.31 b*

Figure 2.31. *Mach isolines for M_{is} = 1.35 for the wide channel [a] 62, [b] 64.*
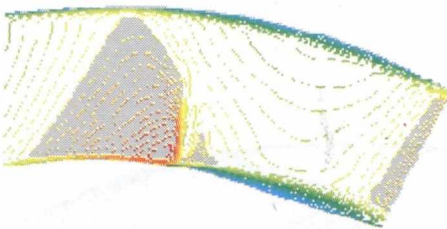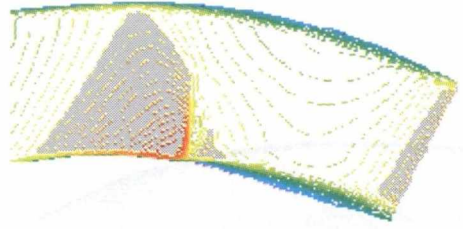
Figure 2.32 a   *Figure 2.32 b*

Figure 2.32. *Mach isolines for M_{is} = 1.35 for the narrow channel [a] 62, [b] 64.*
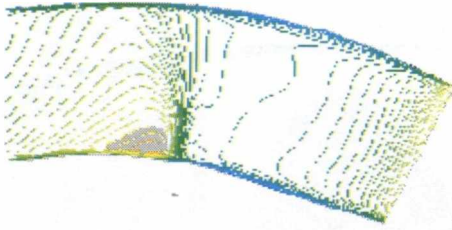
Figure 2.33 a
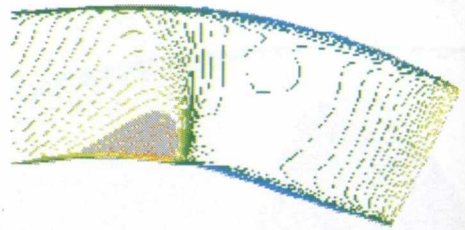
Figure 2.33 b
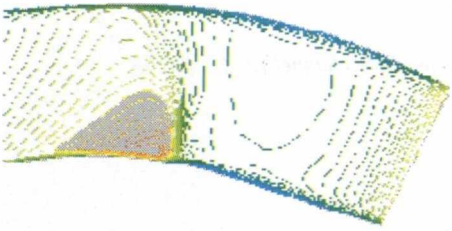
Figure 2.33 c
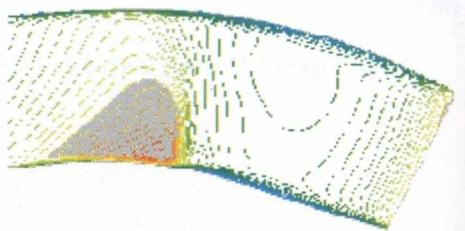
Figure 2.33 d
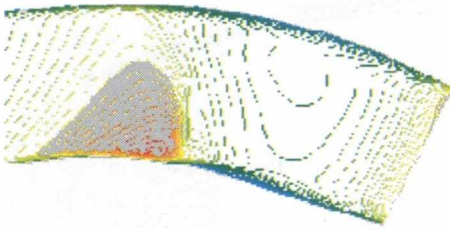
Figure 2.33 e
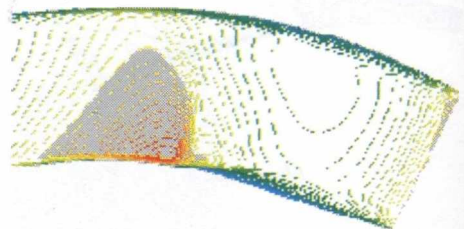
Figure 2.33 f

Figure 2.33. Mach isolines for $M_{is} = 1.35$ for the narrow channel [a] 38, [b] 40, [c] 42, [d] 44, [e] 46, [f] 48.
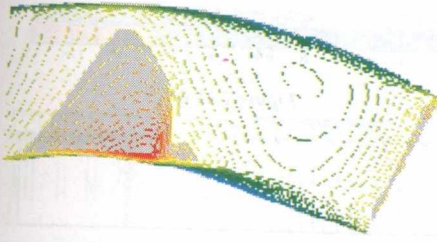
Figure 2.34 a
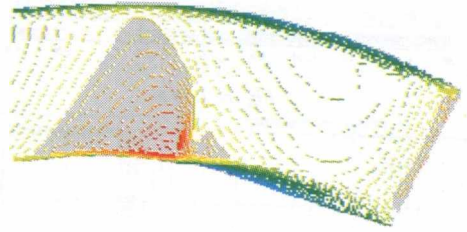
Figure 2.34 b
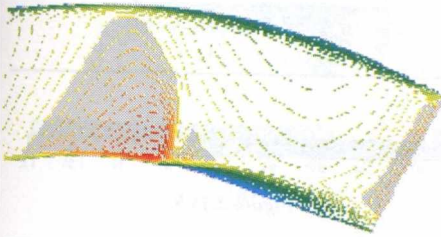
Figure 2.34 c
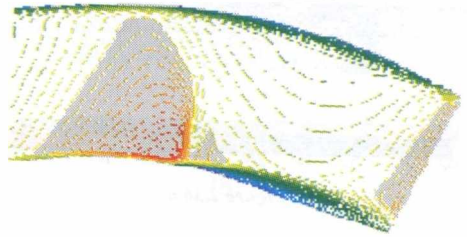
Figure 2.34 d
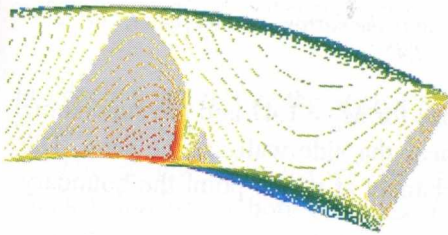
Figure 2.34 e
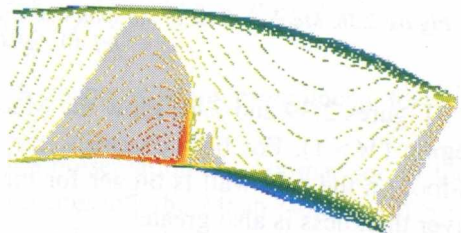
Figure 2.34 f

Figure 2.34. *Mach isolines for $M_{is} = 1.35$ for the narrow channel [a] 50, [b] 52, [c] 54, [d] 56, [e] 58, [f] 60.*

Figure 2.35 a

Figure 2.35 b

Figure 2.35 c
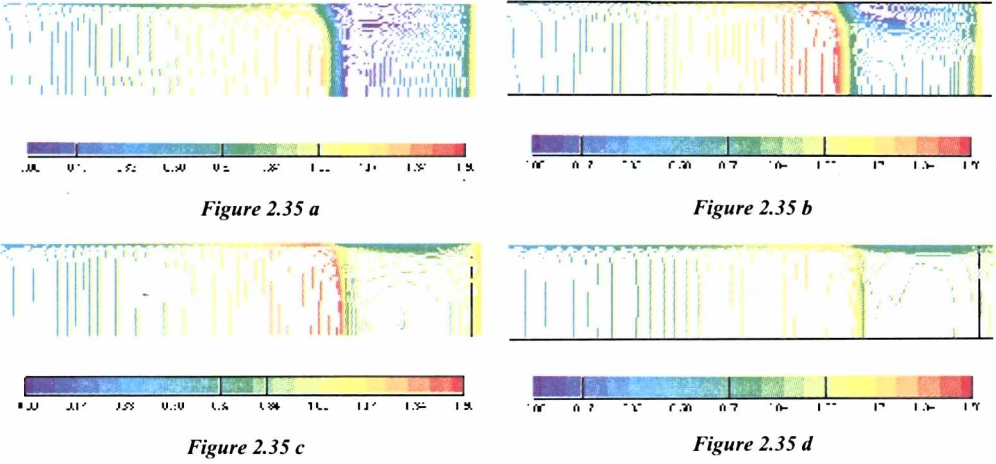
Figure 2.35 d

Figure 2.35. Mach isolines of the spanwise-streamwise cut in the wide channel [a] 24, [b] 32, [c] 40, [d] 48 for M_{is} = 1.47.

Figure 2.36 a

Figure 2.36 b

Figure 2.36 c
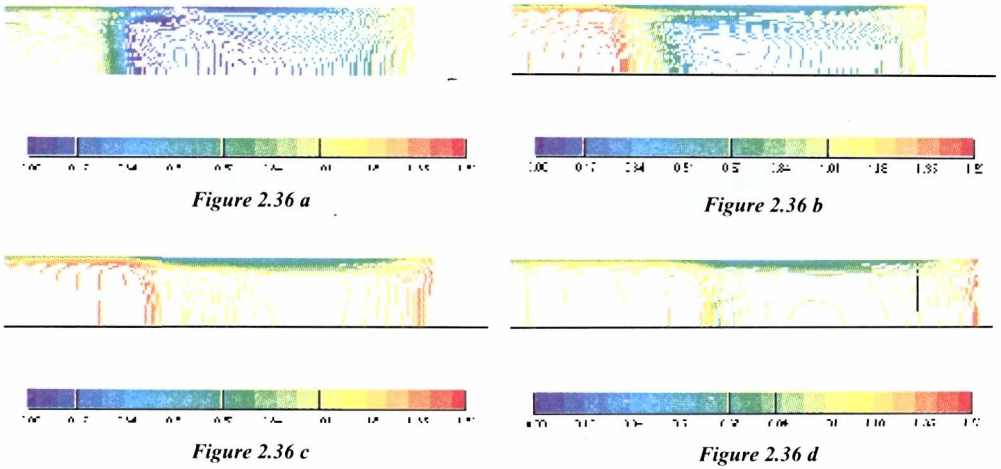
Figure 2.36 d

Figure 2.36. Mach isolines of the spanwise-streamwise cut in the narrow channel [a] 24, [b] 32, [c] 40, [d] 48 for M_{is} = 1.47.

Figures 2.39 and 2.40 show the Mach isolines for M_{is} = 1.47 and the supersonic region ($M > 1$). For both channels, the l-foot near the side wall can be seen. The λ-foot on the side wall is bigger for the wide channel at which point the boundary layer thickness is also greater.

Figure 2.41 shows the sonic contour ($M > 1$) for the wide channel while Figure 2.42 shows the sonic contour ($M > 1$) for the narrow channel. Both presented cases are for M_{is} = 1.47.

Figure 2.43 shows the sonic contour ($M > 1$) for the wide channel while Figure 2.44 shows the sonic contour ($M > 1$) for the narrow channel. Both presented cases are for M_{is} = 1.35. In both, the supersonic region grows for a corresponding growth
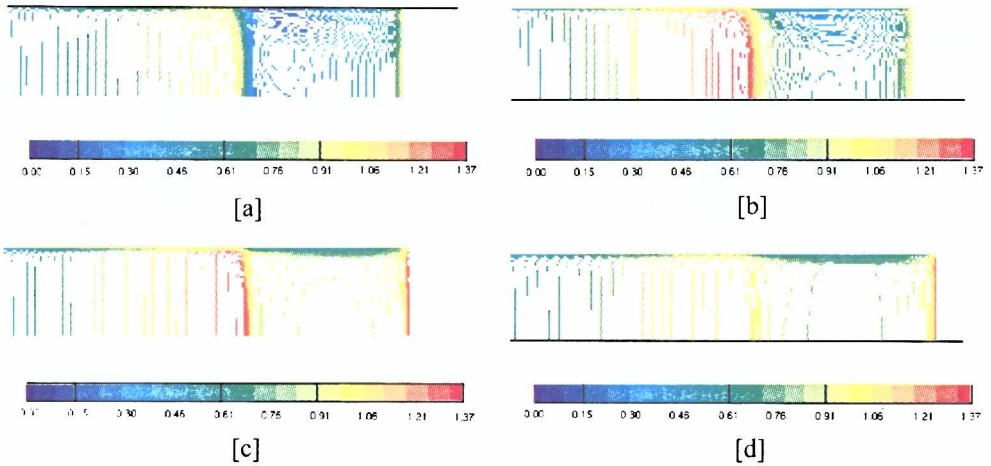
Figure 2.37. *Mach isolines of the spanwise-streamwise cut in the wide channel [a] 24, [b] 32, [c] 40, [d] 48 for M_{is} = 1.35.*
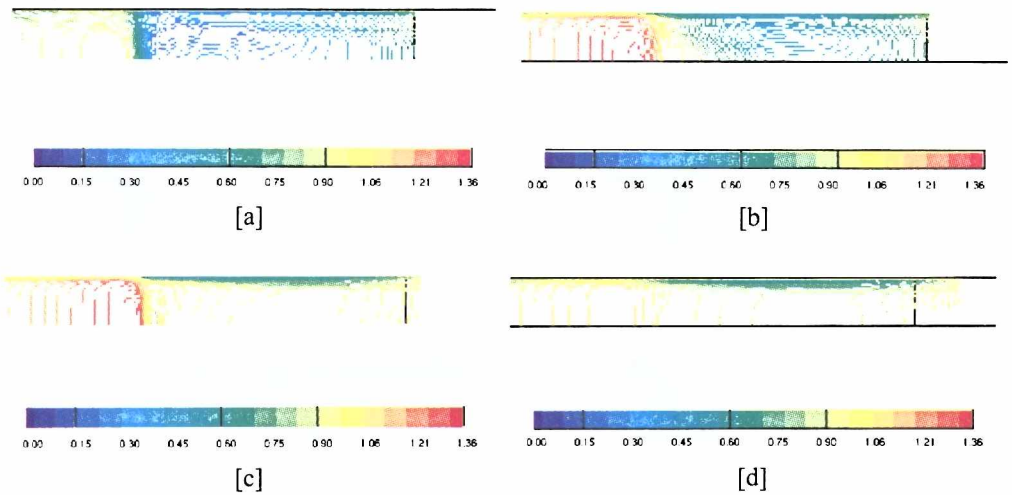
Figure 2.38. *Mach isolines of the spanwise-streamwise cut in the narrow channel [a] 24, [b] 32, [c] 40, [d] 48 M_{is} = 1.35.*

in Mach number but the region's change in shape is more pronounced for the narrow channel.

This review of results will be closed with a presentation and comparison of the shock behavior for both channels. Figure 2.45 presents the Mach isolines ($M > 1$) for both channels. Figure [a] presents the case for M_{is} = 1.47 while Figure [b] shows the case for M_{is} = 1.35. All cases are studied in the middle cross-section of the channel. The figures show the large height of the λ-foot — for the narrow channel. The position of the shock is much different for higher Mach number but the angle of interaction (the angle where the flow separates from the wall) is the same for both channels.
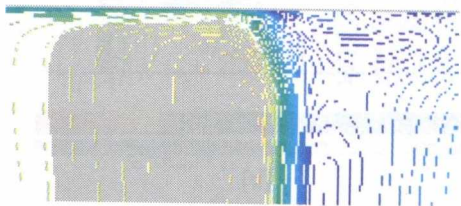
Figure 2.39 a
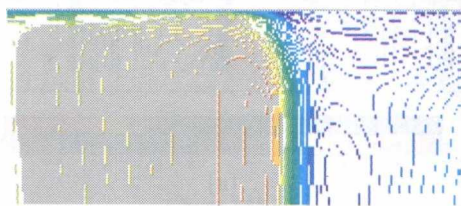
Figure 2.39 b
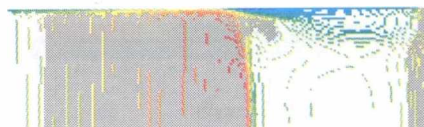
Figure 2.39 c
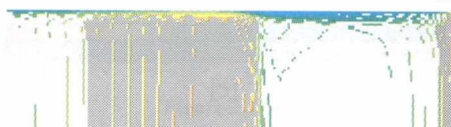
Figure 2.39 d

Figure 2.39. *Mach isolines in a spanwise-streamwise cut of the wide channel [a] 23, [b] 25, [c] 38, [d] 48 M_{is} = 1.47.*

Figure 2.40 a

Figure 2.40 b

Figure 2.40 c
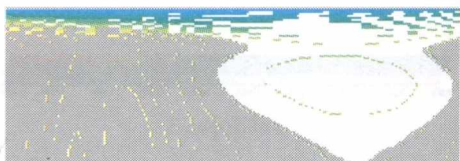
Figure 2.40 d

Figure 2.40 e

Figure 2.40 f

Figure 2.40. *Mach isolines in a spanwise-streamwise cut of the narrow channel [a] 24, [b] 25, [c] 26, [d] 38, [e] 45, [f] 48 M_{is} = 1.47.*
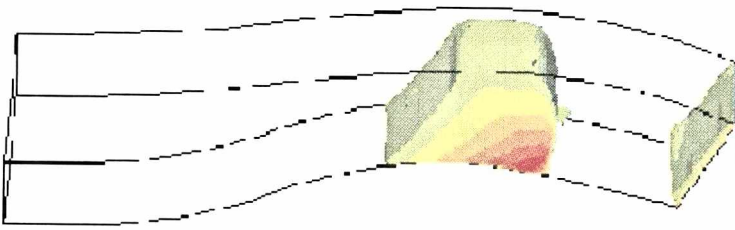
Figure 2.41. *The sonic contour for the wide channel with* $M_{is} = 1.47$.
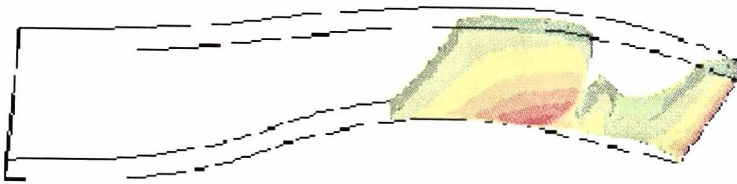
Figure 2.42. *The sonic contour for the narrow channel with* $M_{is} = 1.47$.
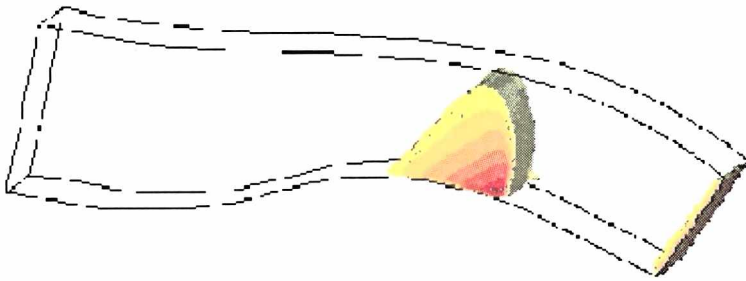
Figure 2.43. *The sonic contour for the wide channel with* $M_{is} = 1.35$.
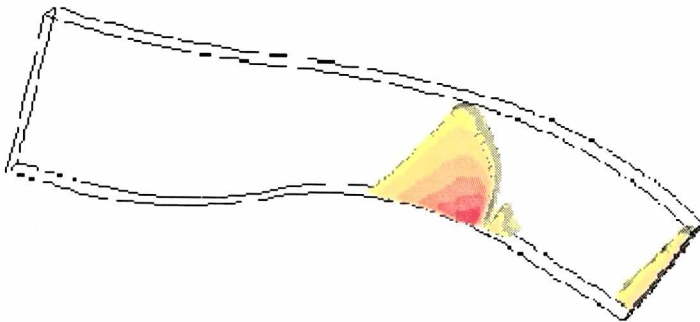
Figure 2.44. *The sonic contour for the narrow channel with* $M_{is} = 1.35$.
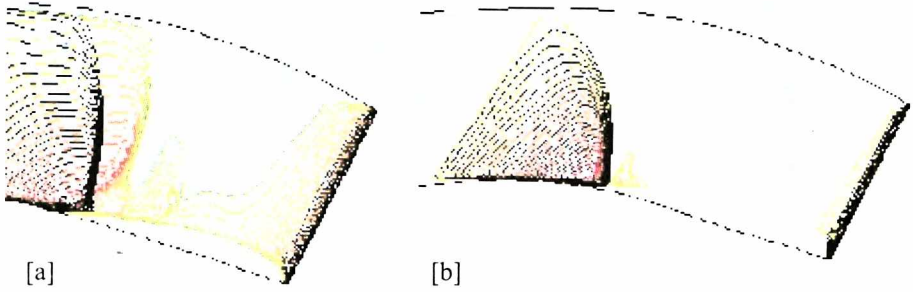
Figure 2.45. Mach isolines (Ma>1) for both channels. Black — wide channel, color — narrow channel; [a] M_{is} = 1.47, [b] M_{is} = 1.35.
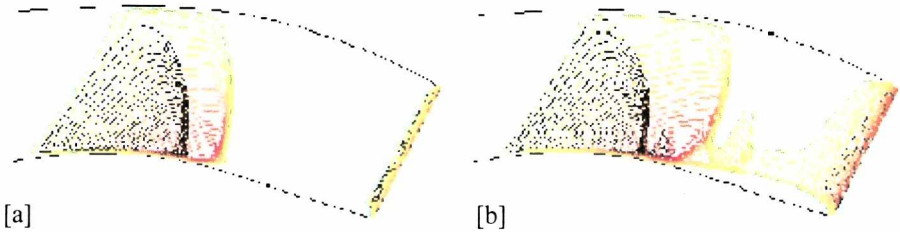
Figure 2.46. Mach isolines (Ma > 1). Black — M_{is}=1.35 color — M_{is}=1.47; [a] wide channel; [b] narrow channel.

Figure 2.46 presents Mach isolines. Figure [a] is for the wide channel with both Mach numbers and Figure [b] is for the narrow channel with both Mach numbers. Most notable from these figures is the difference in the shock position evident due to a growing Mach number.

Finally, to specify the position of the shock on the bottom wall the pressure distribution in the middle of the channels is shown in Figure 2.47. Table 2.4 presents the values of the height of the λ-foot.

Table 2.4. Normalized height of λ-foot and Reynolds number based on the boundary layer thickness for the narrow and wide channel.

	Re (M_{is}=1.47)	h/δ (M_{is}=1.47)	Re (M_{is}=1.35)	h/δ (M_{is}=1.35)
wide channel	71600	5.86	93090	2.11
narrow channel	105000	5.77	93090	2.35
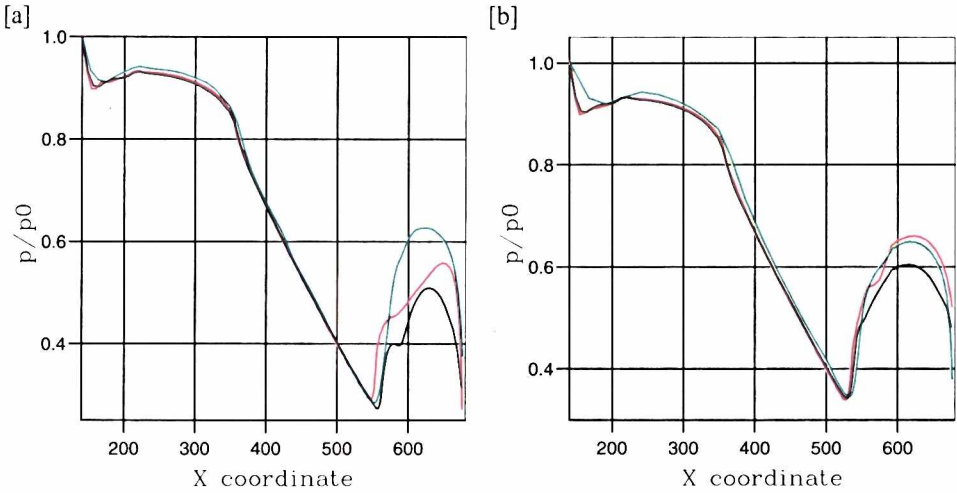
Figure 2.47. *The normalized pressure distribution on the bottom wall in the 2D channel (red); and in the middle of the bottom wall in 3D: narrow channel (black), wide (green). It can be seen the changes in position of the shock and differences in pressure distribution downstream. [a] M_{is} = 1.47; [b] M_{is} = 1.35.*

2.4.3 Shock structure — comparison with experiment

In this section, a comparison with experimental data will be presented. Attention will be paid to the basic shock parameters including the height of the λ-foot structure and its connection with the boundary layer thickness.

In the Karslruhe experiments of Doerffer [45] the narrow channel was investigated. The wide channel was studied in experiments carried out in Warsaw [46].

Boundary layer thicknesses for both cases, as well as for computations, are presented in Table 2.5.

Table 2.5 *Boundary layer thickness for experiments and numerical calculations.*

	M_{is}=1.47	M_{is}=1.35
boundary layer thickness wide channel experiment [mm]	2.36	2.31
boundary layer thickness wide channel calculations [mm]	3.1	4.2
boundary layer thickness narrow channel experiment [mm]	3.16	3.21
boundary layer thickness narrow channel calculations [mm]	4.5	4.2

The thickness of the boundary layer in experiments is different for narrow and wide channels. The same tendency in numerical calculations can also be seen but the numerical boundary layer is thicker than experimental one. There are several causes for this difference. One can be connected with the numerical boundary conditions. The inlet boundary layer, which has its origin in the pressure conditions, is different than the experimental one. Downstream, the boundary layer can be modified by the flow but it cannot be efficient enough. The best way to assure that the inlet boundary layer has no influence would be to give the same boundary layer profile at the inlet as in experiment. Such data was not available. Another reason for the difference in the boundary layer profiles can be connected with the thickness of the boundary layer at the side walls. The measurements of such quantities were not done. Both the cases for the narrow and wide channels show that the side wall boundary layer has a large influence on both the shock structure and separation region. Due to this, information about the side wall boundary layer would be helpful in the comparison of numerics to experiment.

Table 2.6 presents the λ-foot height normalized by the boundary layer thickness. The tendency that the λ-foot grows for larger Mach numbers is the same for both experiments and calculations.

Table 2.6 *Normalized height of λ-foot for experiments and numerical calculations for narrow and wide channel.*

	h/δ ($M_{is}=1.47$)	h/δ ($M_{is}=1.35$)
wide channel experiments	4.98	1.8
wide channel calculations	5.86	2.11
narrow channel experiments	6.87	2.97
narrow channel calculations	5.77	2.35

Figure 2.48 presents another way of comparison. The function of Mach number and Reynolds number is considered. The function is given by the relation [45, 46]:

$$f(M,Re) = \frac{\left(M^2 - 1\right)Re^{-0.17}}{\left(1 + \dfrac{\kappa - 1}{2}M^2\right)^{\frac{\kappa}{\kappa-1}}} \tag{2.2}$$

The normalized λ-foot height is plotted as a function of Mach and Reynolds number. The solid line presents experiments for the narrow channel, triangles are points from experiments in the wide channel and circles present numerical calculations. The results are in quite good agreement. It can be seen that the points from calculations are a bit higher then experiments. The reason for this can be the difference of the boundary layer on the side walls. Also, information about

turbulence in the experiment are missing and thus could be helpful for choosing the proper turbulence model or setting boundary conditions for turbulence level or length scale.
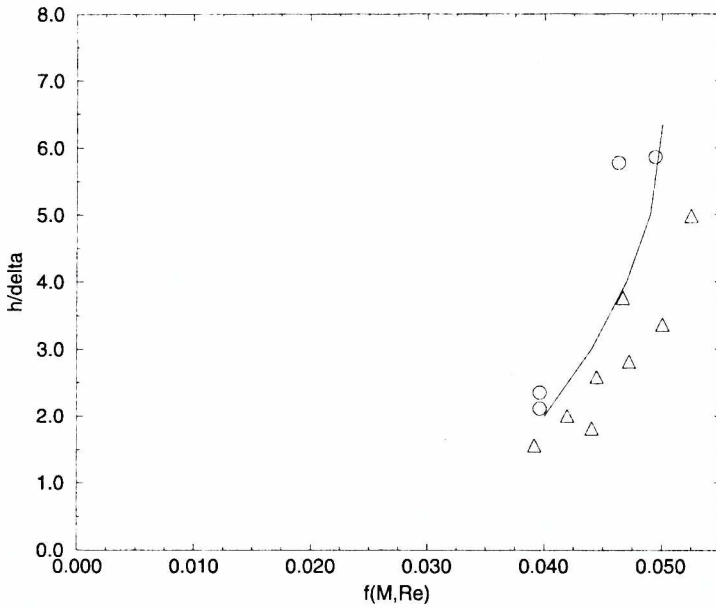
Figure 2.48. *Comparison between experimental data and computations; triangles — experiments in wide channel; solid line — experiments in narrow channel; circles — numerical results.*
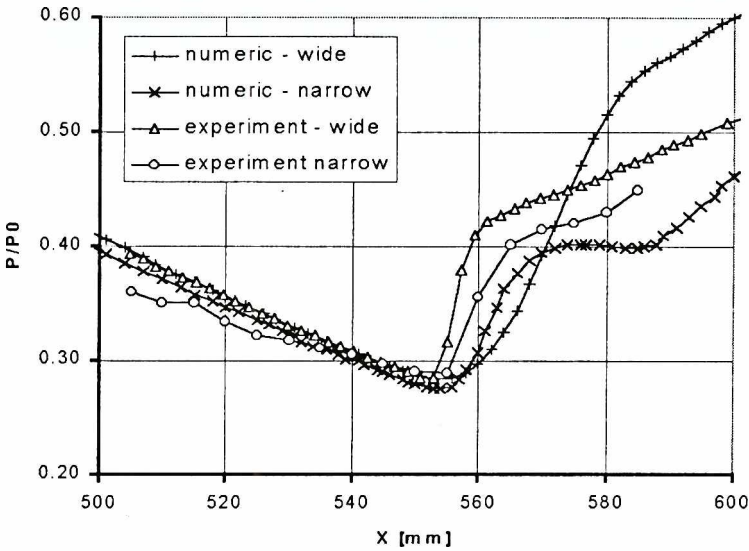
Figure 2.49. *Comparison between experimental data and computations — pressure distribution on the bottom wall in the middle cross-section.*

Figure 2.49 shows the pressure distribution in the middle of the channel for the wide and narrow channels. The considered isentropic Mach number is $M_{is} = 1.47$. The differences in distribution after the shock are caused by the separation. The turbulence modeling still could not precisely predict the behavior of the separation region although the tendency (angle of the curve) is similar for experiment and calculations.

The last comparison of this section will be the presentation of the shock wave structure obtained by Schlieren photography. Figure 2.50 shows pictures for the narrow [a] and wide [b] channels with an isentropic Mach number $M_{is} = 1.47$. This Figure can be compared with the Mach isolines of Figure 2.17.

Two differences between the narrow and wide channels can be noticed:

— The λ-foot in the middle of the wide channel is smaller than in the narrow one

— In the narrow channel, a second shock (connected with after expansion) is observed while only a single one is observed in the wide channel

Both above observations were true for experiment and numerical calculations.
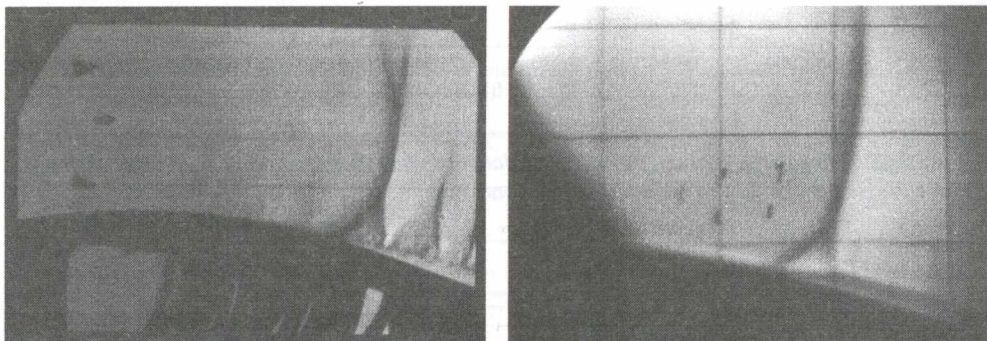
Figure 2.50. Schlieren visualization; [a] wide; [b] narrow channel.

2.4.4. Influence of the symmetric boundary condition on the structure of the shock wave

In the previous section, computations used the symmetry condition. The structure analysis, which will be presented in Chapter 3, shows that this condition has an influence on the structures of the flow. Due to this, calculations were done without an assumption of symmetry. The numeric simulation used a grid of size of 129×97×97.

Because of this it was necessary to show, the influence of that condition on the global flow parameters.

In Figure 2.51 Mach, isolines for isentropic Mach number $M_{is} = 1.47$ in the middle cross-section of the curved channels are presented. Again in the narrow channel, the λ-foot is larger and the second smaller shock exists.

[a]


```
0.00    0.17    0.33    0.50    0.67    0.83    1.00    1.17    1.33    1.50
```

[b]


```
0.00    0.16    0.33    0.49    0.66    0.82    0.98    1.15    1.31    1.48
```
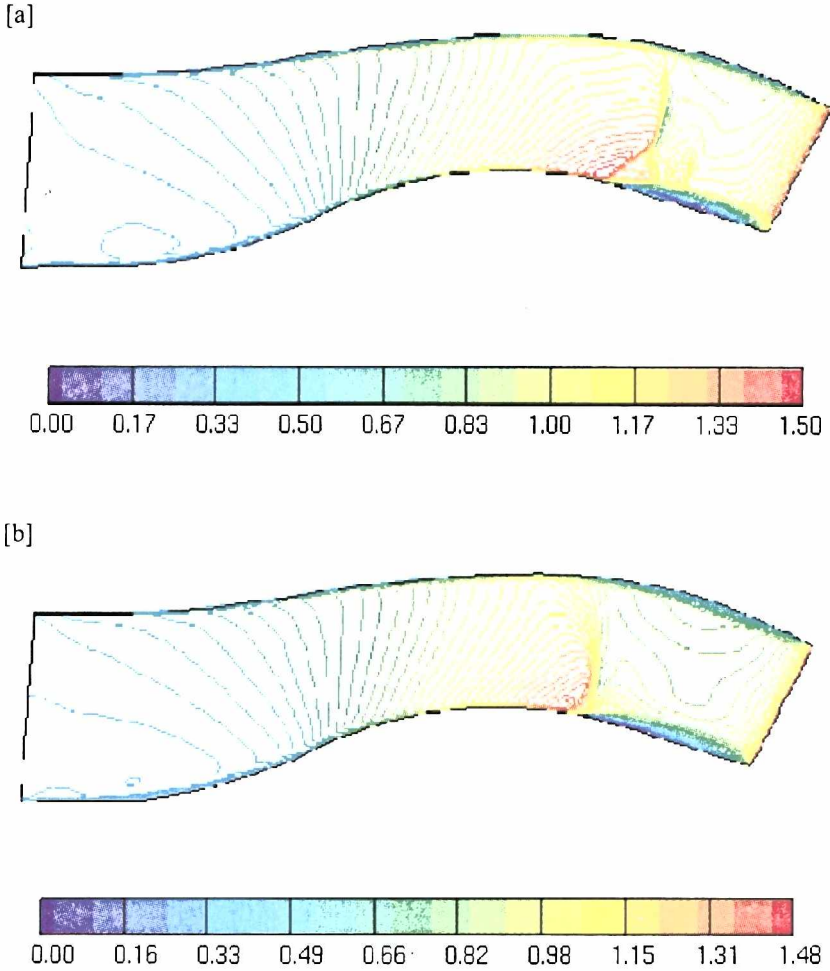
Figure 2.51. *Mach number isolines in the curved three-dimensional channel for $M_{is} = 1.47$ and the middle cross-section. Calculations were done without the condition of symmetry. [a] narrow channel [b] wide channel.*

Figure 2.52 show the pressure distribution on the bottom of the channel in the middle cross-section for the wide and narrow channels. The red lines represent pressure resulting from the calculation in the middle of the channel with the assumption of symmetry while the black lines show results of the computation with no assumption of symmetry. he difference between the two can only be seen in the region of separation.

In Chapter 3 the structures of the separation will be studied for both boundary conditions. A significant difference in separation for each of the two computations will be shown. The current section shows that there is no difference in the shock and flow structures for the two cases, as was expected.

[a]   [b]
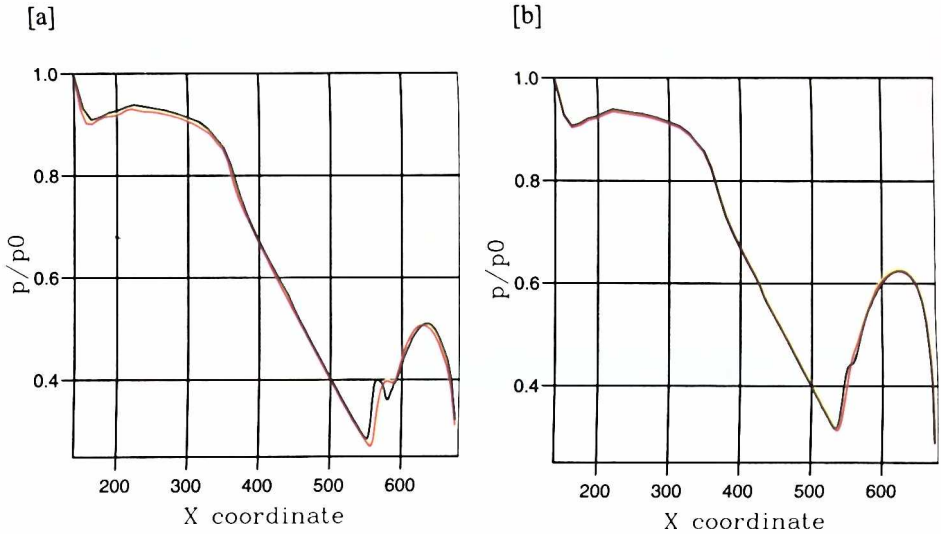
Figure 2.52. *Pressure distribution in the middle of the curved three-dimensional channel for*
$M_{is} = 1.47$ *on the bottom wall. The red curve corresponds to the computations with the symmetry*
condition while the black corresponds to the computations done on the whole channel.
[a] narrow channel [b] wide channel.

2.5 Summary

— The λ-foot height depends on the boundary layer. With a thicker boundary layer, the λ-foot is larger. This tendency is similar for both experiment and numerical calculations.

— The λ-foot height depends on the Mach number. Larger Mach numbers result in a growth of the λ-foot. This is observed in both calculation and experiment.

— The width of the curved channel has a large influence on the λ-foot structure. In the narrow channel, the λ-foot is larger due to the thicker boundary layer and there is also a second smaller shock due to the stronger interaction of the side walls boundary layers. Calculations agree with the experimental data.

— The symmetry condition in the middle of the channel has no influence on the shock and flow structure.

— The numerical scheme used can cause large differences in the shock structure. The switch scheme gives better agreement to experimental data than the slip scheme.

— Two-dimensional calculations are more similar to the calculations in the wide channel (pressure distribution). Three-dimensional effects cannot be properly rendered by two-dimensional calculations.

3. Shock induced separation

3.1 Introduction

In this Chapter the flow structures induced by the normal shock boundary layer separation will be studied. Consideration will be restricted to the three-dimensional curved channel computations presented in Chapter 2. The separation region for that type of channel occurs only at the bottom wall and some small structures can be seen near the bottom on the side walls.

The aim will be to study the two-dimensional structures on the walls and the three-dimensional structures of the separation. The structures obtained by computations will be compared with experimental photographs of oil visualization. The influence of the isentropic Mach number, width of the curved channel and the symmetry conditions on the separation structures will be studied.

3.2. Computations using the symmetry condition

In this section the separation structures for $M_{is} = 1.35$ and $M_{is} = 1.47$ will be presented. Attention will be focused on computations carried out on a grid of size ($129 \times 97 \times 65$) with the use of the symmetry condition in the middle of the channel. For all Figures in this section the flow direction is from left to right.

3.2.1 Separation structures for $M_{is} = 1.35$

Figure 3.1 presents flow for $M_{is} = 1.35$ in the wide channel. The side wall and bottom wall are shown. Observation of the side wall shows a saddle point and bifurcation line. These are the first structures which occur and are connected with shock induced separation. Such structures extent normal to a wall are characteristically small with comparison to the geometry of the channel. Shock wave causes a sudden inclination of lines towards the bottom wall (Figure 3.1 [a]).

All these lines run into a bifurcation line above the bottom wall.The bifurcation line is connected with the corner vortex which appears due to the shock's interaction with the boundary layer.The corner vortex will continue to exist for a higher Mach number and its presence will be shown in further Figures. Figure 3.1 [b] shows the structures occurring on the bottom wall. Here, the beginning of separation occurs near the side wall.In Figure 3.1 [b] upper limit is a center line and the lower one is the side wall.

In Figure 3.2 the structures for the narrow channel with $M_{is} = 1.35$ are plotted. The bottom wall structures look quite similar to those for the wide channel. The only difference is that near the saddle point the origin of the focal point can be seen. Similar to the wide channel, separation on the bottom wall occurs near the side wall. The influence of the side wall is bigger for the narrow channel.

Both Figures 3.1 and 3.2 illustrate that for $M_{is} = 1.35$ the separations induced by the shock wave boundary interaction starts to appear, but it is restricted to the vicinity of the bottom-side wall corner.

[a]

[b]
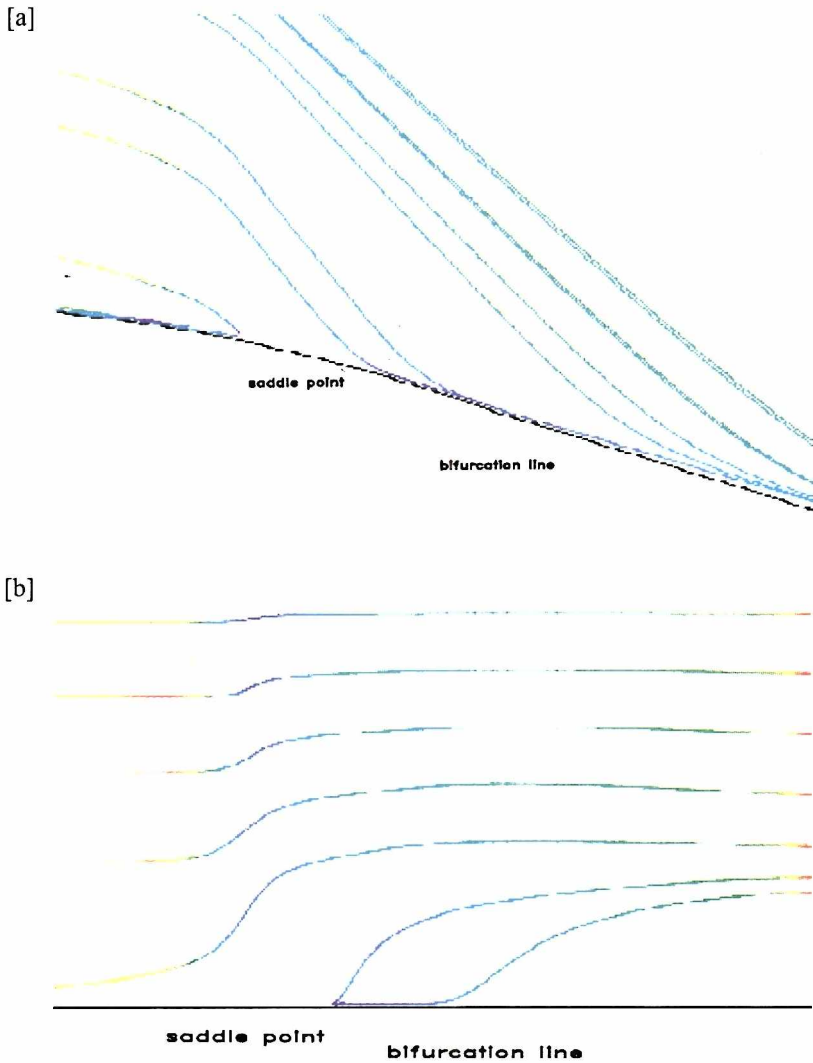
Figure 3.1. Structures of the separation for the wide channel for $M_{is} = 1.35$ [a] side wall [b] bottom wall.

3.2.2 Separation structures for $M_{is} = 1.47$

For Mach number $M_{is} = 1.47$ the shock induced separation is much larger. In Figure 3.3 [a] the side wall for the wide channel is shown. This picture looks very similar to figure 3.1 [a] except that the angle of the lines is more steep. The topological structures on the side wall for $M_{is} = 1.35$ and $M_{is} = 1.47$ are the same. Figure 3.3 [b] presents the middle cross-section of the channel (where the symmetry boundary condition was assumed). Here the vortex can be seen which is present in

[a]

[b]
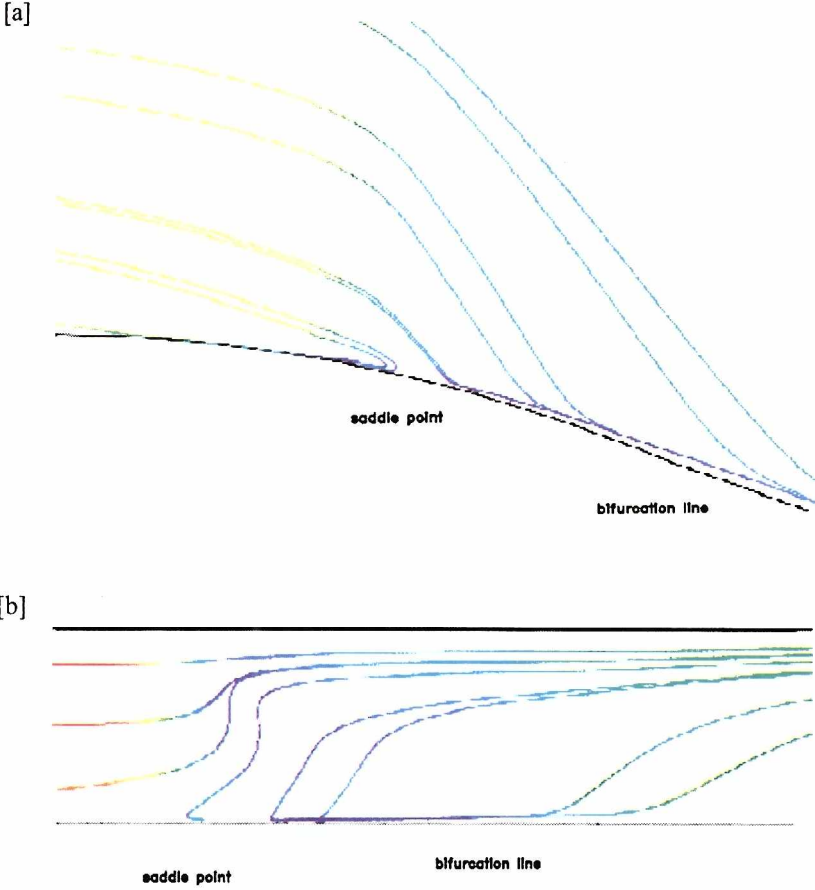
Figure 3.2. *Structures of the separation for the narrow channel for M_{is} = 1.35 [a] side wall*
[b] bottom wall.

the middle of the channel. Figure 3.4 [a] presents the bottom of the channel. The separation for this case of Mach number is present even in the middle of the channel. Structures at the side wall (bottom line on the Figure) are similar to those seen for M_{is} = 1.35. In the middle of the channel there are two points: node and saddle. They correspond to two saddle points in figure 3.3 [b]. As it was shown in Chapter 1, the three-dimensional saddle point is represented as a saddle point in two planes and in one plane as a node. Due to this the saddle point from the middle of the channel in Figure 3.4 [a] in the third cross-section, perpendicular to the middle line is a node. Other points will be similar. There is one more interesting observation. Due to the symmetry condition the flow upstream and within separation is slightly directed to the center of the channel. Figure 3.4 [b] shows the three-dimensional structures and includes a vortex in the middle of the channel. The
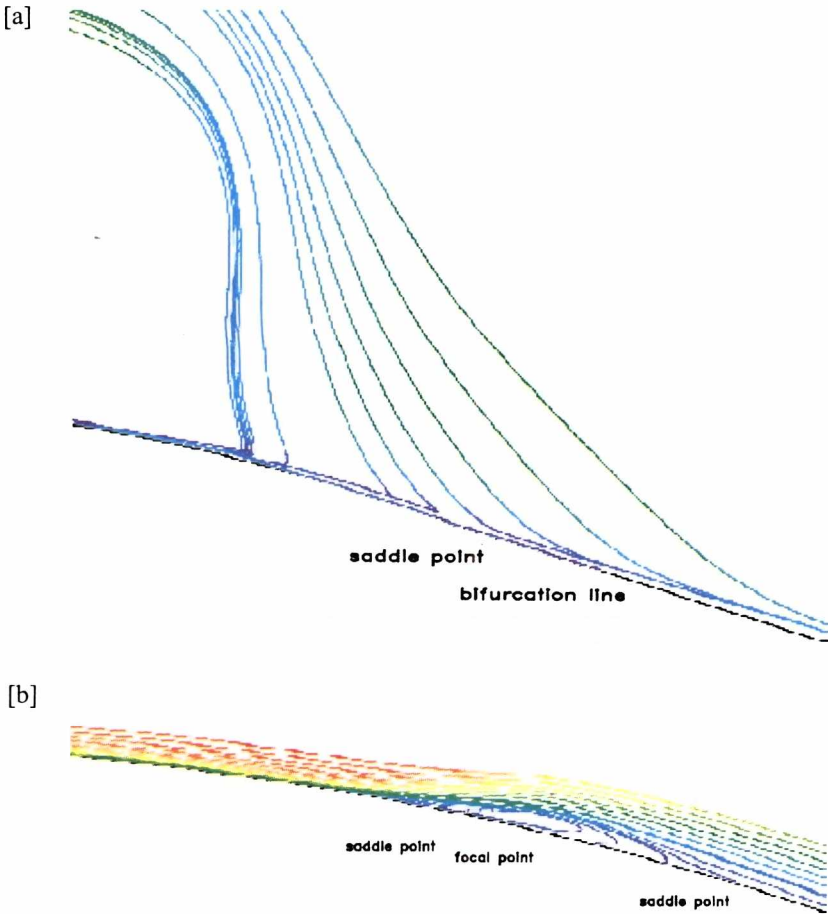
Figure 3.3. *Structures of the separation for the wide channel for* $M_{is} = 1.47$ *[a] side wall [b] middle cross-section wall.*

view is from the outlet end of the channel. This vortex is not seen in Figure 3.4 [a], but the reverse flow flow in the separated area is caused by its presence. It can be observed that the flow from the side wall moves in the direction of the bottom wall where it causes the vortex. Also from this Figure it can be noted that the side boundary layer has a large influence on the global behavior of the flow. Again it can be observed that the separation structures are very flat compared to their width.

Figure 3.5 presents the side wall and middle cross-section for the narrow channel. The side wall structures are different than those for either $M_{is} = 1.35$ or the wide channel. On the side wall the vortex can be seen. The middle cross-section is similar to the wide channel. In Figure 3.6 the bottom wall structures are presented. The structure seen there is much different than for the wide channel. Near the side wall (bottom line in Figure) two focal points and one saddle point appear. The

[a]

[b]
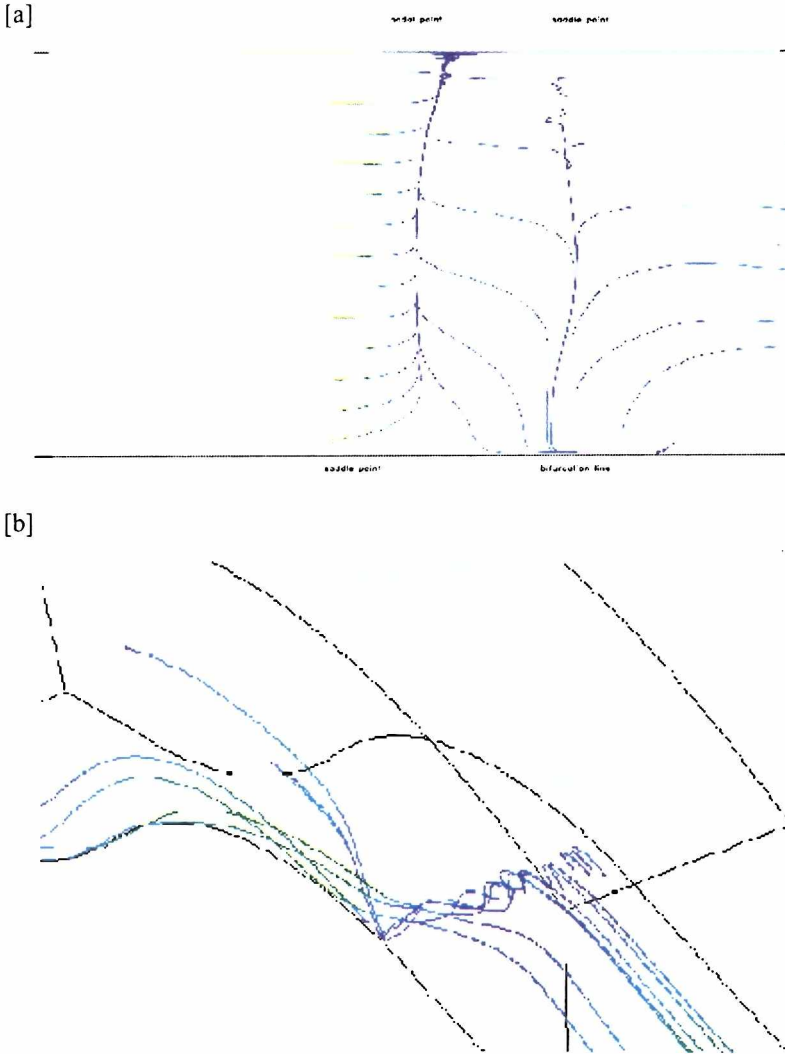
Figure 3.4. Structures of the separation for the wide channel for M_{is} = 1.47 [a] bottom wall [b] three-dimensional structures.

center line structures are the same as for the wide channel. The flow direction before the separation is again forced by the symmetry condition so that the flow is directed towards the node. Due to the presence of the focal points, to fulfill all conditions, the saddle point appears. Figure 3.7 shows the three-dimensional structures in two views.The lines are obtained by integration forward and backward starting from points near the bottom wall. It can be seen that part of the flow near the bottom wall has its origin at the side boundary layer. Similar influence of the side wall was observed for the wide channel. Due to the vortices on the bottom wall, the three-dimensional structures of the narrow channel are again different than those for the wide channel.

[a]

[b]
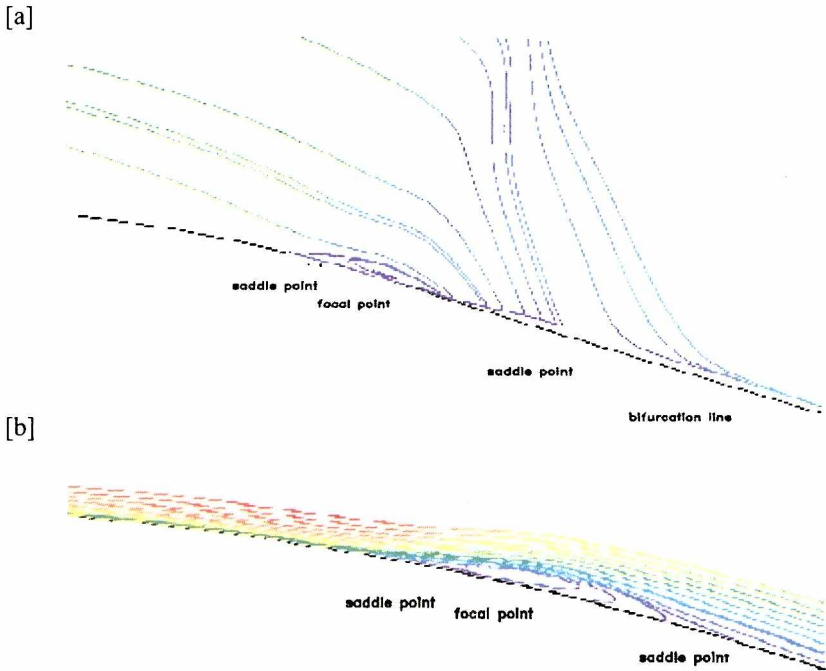
Figure 3.5. Structures of the separation for the narrow channel for M_{is} = 1.47 [a] side wall [b] middle cross-section wall.
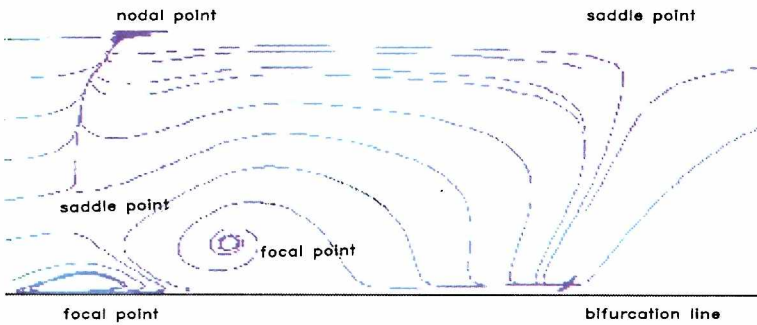
Figure 3.6. Structures of the separation for the narrow channel for M_{is} =1.47 on the bottom wall.

In Figure 3.8 the structures for isentropic Mach number M_{is} = 1.47 for a course grid (eight times less points) are presented. For the narrow channel the grid renders the general character of the separation region while, for the wide channel, the separations is not present in the middle of the channel.
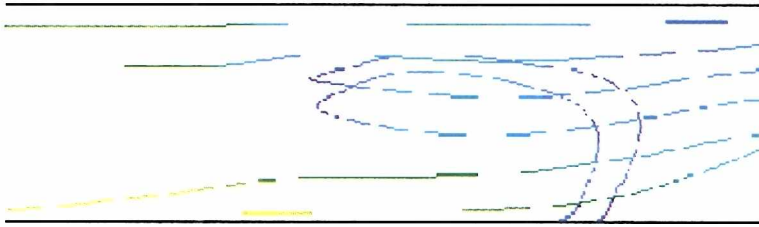
Figure 3.7 a
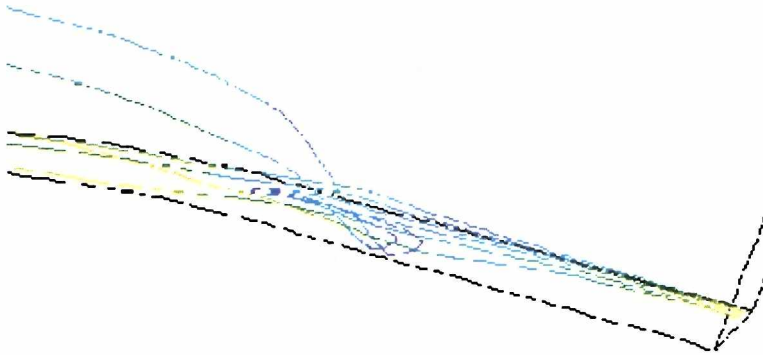
Figure 3.7 b

Figure 3.7. *Three-dimensional structures of the separation for the narrow channel for $M_{is} = 1.47$ [a] view from the top; [b] view from the side wall.*
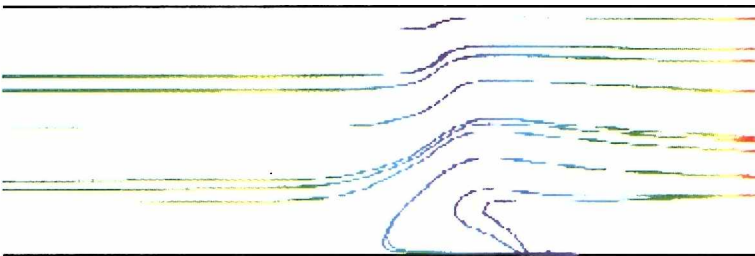
Figure 3.8 a

Figure 3.8 b

Figure 3.8. *Coarse grid influence on the separation structures for $M_{is} = 1.47$ [a] wide channel [b] narrow channel.*

3.3 The computations of the entire curved channel

This section will show the differences in the structures which occur due to the assumption of the symmetry condition for the flow. The grid for computing the entire channel was 129×97×97. Only the case for the developed separation at Mach number M_{is} = 1.47 will be considered.

In Figures 3.9, 3.10 and 3.11 the structures for the wide channel for M_{is} = 1.47 are shown. Figure 3.9 [a] presents the middle cross-section, 3.9 [b] presents the bottom wall, 3.10 presents the cut across the channel and 3.11 presents the two side

[a]
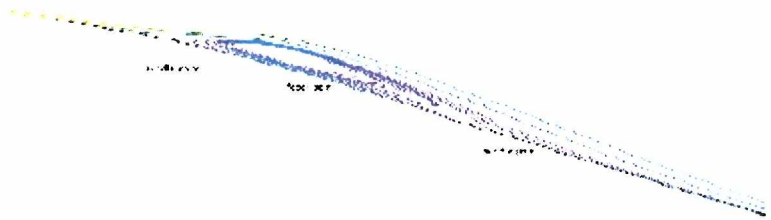
Figure 3.9 a

[b]
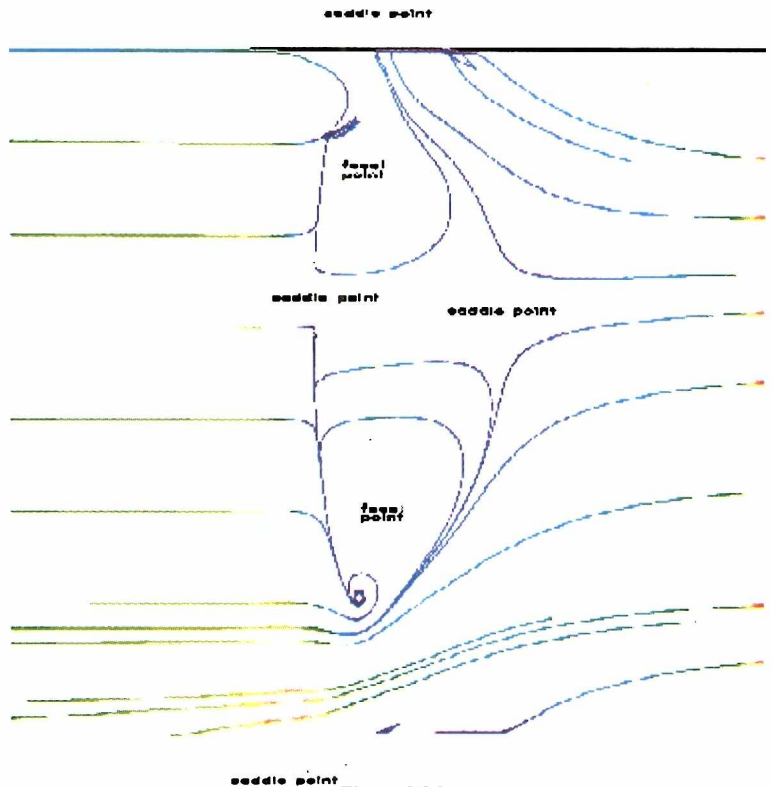
Figure 3.9 b

Figure 3.9. *Structures of the separation for the wide channel for M_{is} = 1.47 [a] middle cross-section [b] bottom wall.*

walls. Figure 3.11 [a] presents the side wall which is a line on top of figures 3.9 [b]. The side wall from Figure 3.11 [b] is indicated by the bottom line in Figure 3.9 [b]. The middle cross-section (see Figure 3.9 [a]) is similar to the case computed with the symmetry condition (Figure 3.3 [b]). The bottom wall structure is completely different from Figure 3.4 [a]. The entire separation region is not symmetric. In the middle of the channel a separation saddle appears instead of a separation node (see Figure 3.4 [a]). It was stated in Chapter 1 that connection of saddle points is structurally unstable. In Figure 3.9 [b] the saddles are not connected and, due to

[a]

Figure 3.10 a

[b]
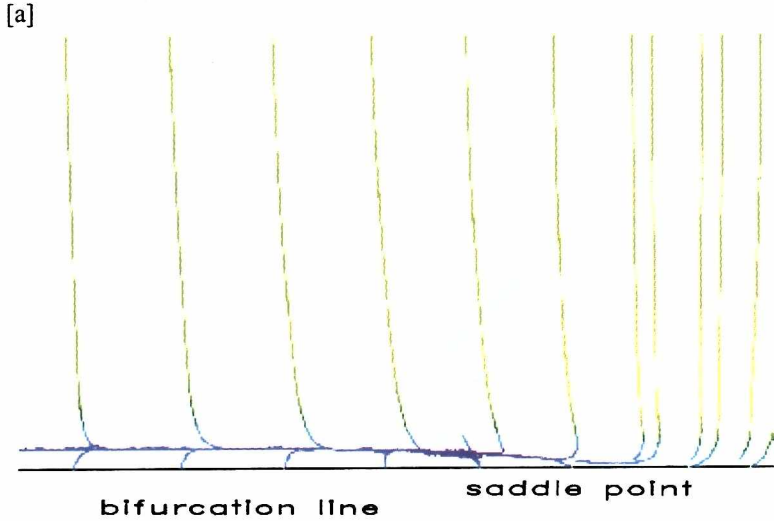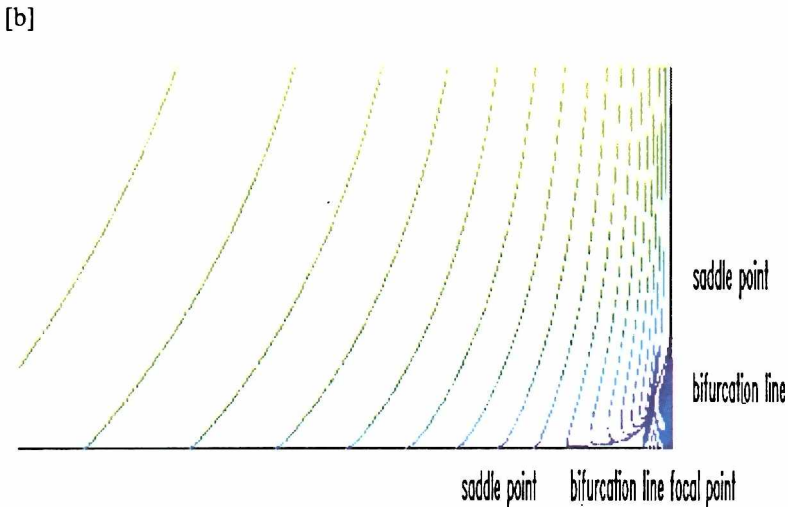
Figure 3.10 b
Figure 3.10. *Structures of the separation for the wide channel for* $M_{is} = 1.47$ *[a] downstream the separation region [b] vortex in the bottom corner.*

this, they are slightly non symmetric. In computations for the wide channel with the symmetry conditions the direct connection between separation and reattachement critical points is imposed. Therefore a node-saddle combination is forced by symmetry. Flow near the middle of the channel upstream of the separation region for the entire channel is directed away from the center. A change of the character of a point in one cross-section causes a change of the character of a point in another cross-section. This means that the general three-dimensional character of the structure is also changed and it follows that focal points appeared for computations of the entire curved channel.

saddle point

bifuroation line

Figure 3.11 a

nodal point

saddle point
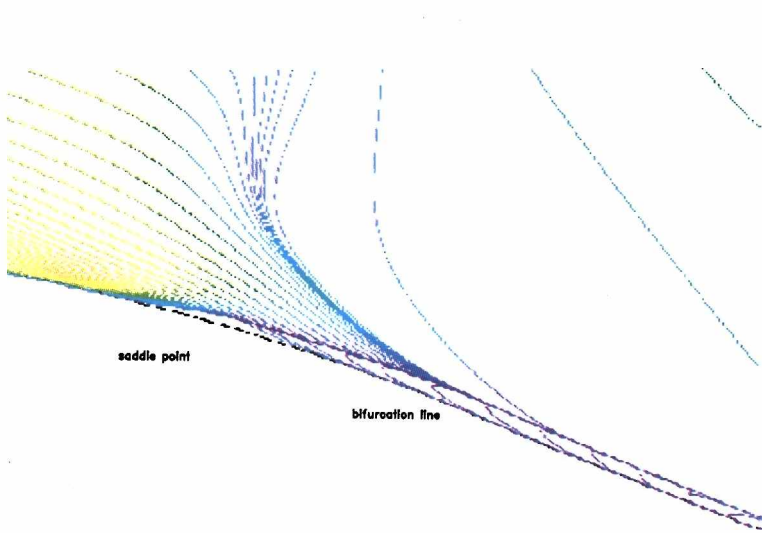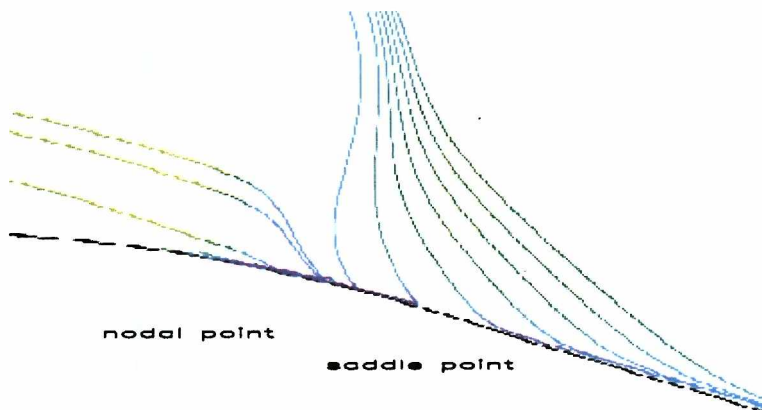
Figure 3.11. Structures of the separation on the side walls for the wide channel for M_{is} = 1.47 [a] wall on top in Figure 3.9 [b] down wall in Figure 3.9.

In Figure 3.10 the cut across the channel is presented. Figure 3.10 [a] shows the separation size compared to the width of the channel while Figure 3.10 [b] shows the corner vortex. Figure 3.11 presents the side walls. The structures are topologically similar to the computations for the wide channel with the symmetry condition.

Figures 3.12, 3.13 and 3.14 present the structures for the narrow channel. In F igure 3.12 [a] the middle cross-section is shown. The topological structures are the same as for the narrow channel with the symmetry condition. The bottom wall structures are different than those of Figure 3.6. The direction of the upstream separation region is connected with the saddle point in the center and it is different than for calculations with the symmetry condition. The entire structure is slightly non-symmetric. This Figure also shows the sizes of the separation region. There are lines which indicate the size of separation region in the center for the wide channel (59 mm). The size of the wide channel separation is 70 mm. The separation region for the narrow channel is larger.

[a]

focal point

separation point

reattachment point

[b]

focal point   bifurcation line
    focal point

    saddle point   saddle point

        focal point
focal point   bifurcation line

separation size for the wide channel
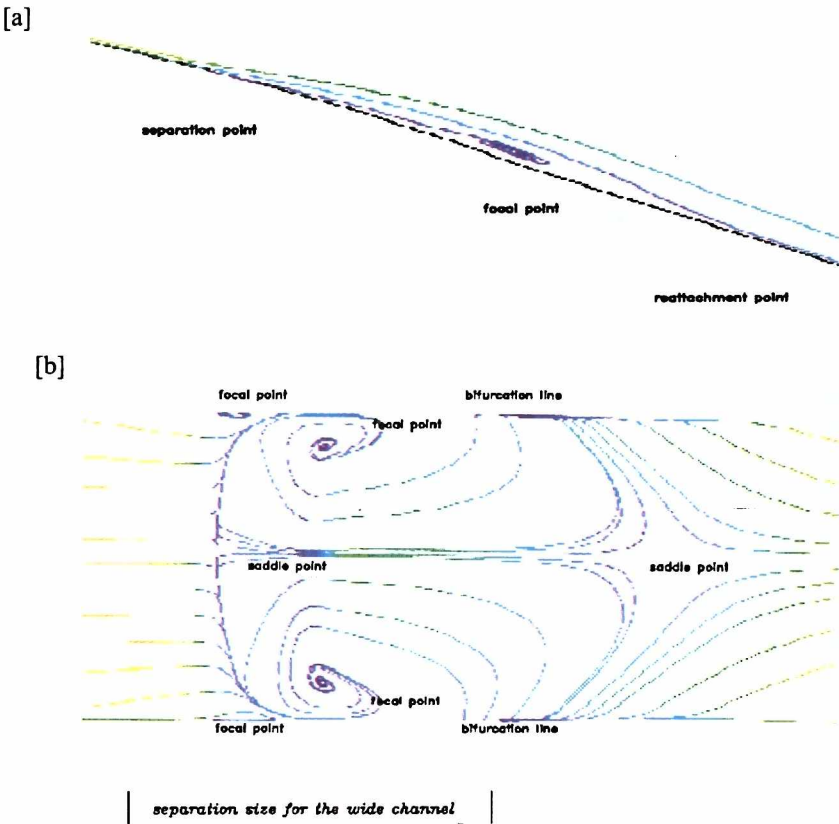
*Figure 3.12. Structures of the separation for the narrow channel for M_{is} = 1.47
[a] middle cross-section [b] bottom wall.*

Compared to the width of the channel, the area occupied by separation for the narrow channel is much larger than for the wide channel. This is connected with the fact that the boundary layer on the side wall has a large influence on the separation region. It can also be noted that the separation appears further upstream for the wide channel. In Figure 3.13 the cut across the channel is presented. Downstream towards the separation region the node can be seen (Figure 3.13 [a]) while Figure 3.13 [b] again shows a corner vortex. Figure 3.14 [a] presents the side wall for the wall indicated as a top line in Figure 3.12 [b] and Figure 3.14 [b] with the side wall which is the bottom line of Figure 3.12 [b]. Both structures are topologically the same and agree with the structure for the narrow channel computed with the symmetry condition (see Figure 3.5 [a]).

[a]

nodal point

Figure 3.13 a

[b]
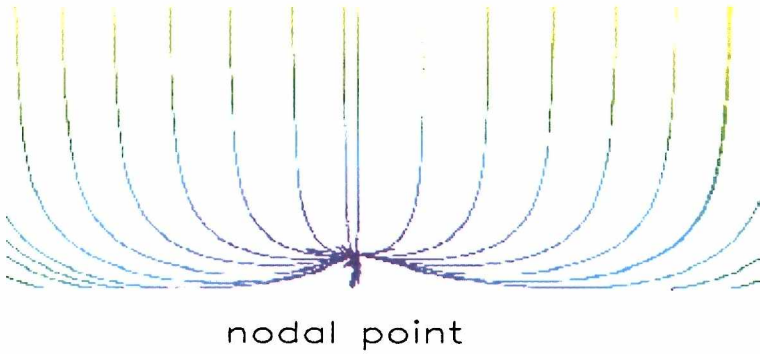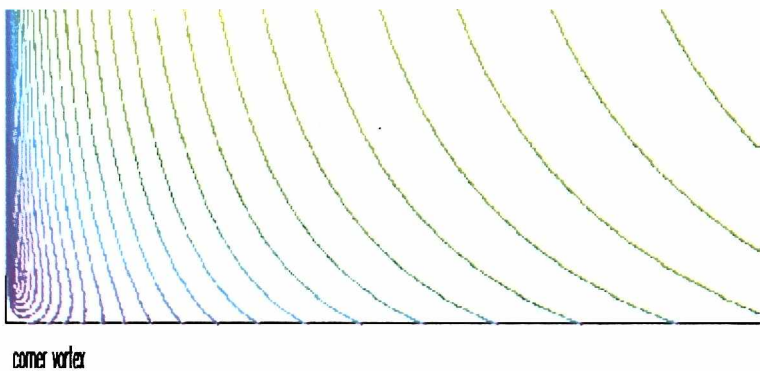
corner vortex

Figure 3.13 b

Figure 3.13. *Structures of the separation for the narrow channel for* $M_{is} = 1.47$
[a] downstream of the separation region [b] vortex in the bottom corner.

Figures 3.15 and 3.16 present the three-dimensional structures. In Figure 3.15 the three dimensional structures for the narrow channel are shown. The vortex has an origin on the bottom wall and the core of the vortex is directed towards the center. At the bottom wall it spirals in and in the middle of the channel it spirals out. Due to this, it must go through the critical point which is shown in Figure 3.15 [b]. This critical point is the vortex of type [g] or [e] from Figure 1.5 in Chapter 1 while the vortices on the bottom wall and middle cross-section are of type [f] in Figure 1.5. In the wide channel it is similar except that the change of the character of the vortex appears closer to the center. This causes larger non-symmetry for the wide channel (See Figure 3.16).

[a]
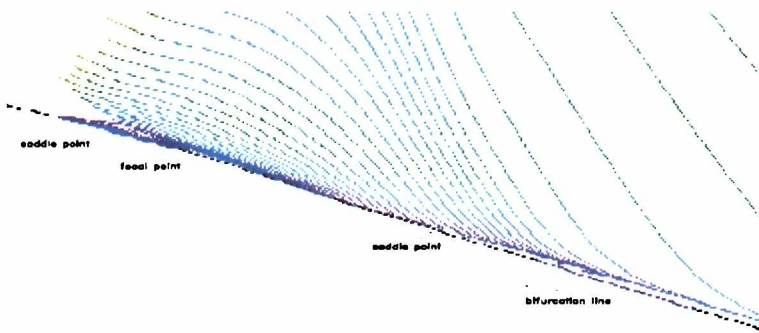
Figure 3.14 a

[b]
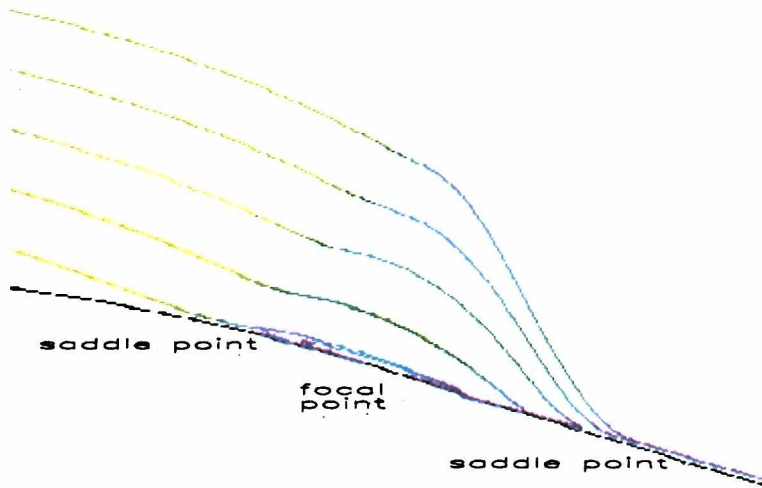
Figure 3.14 b

Figure 3.14. Structures of the separation on the side walls for the narrow channel for $M_{is} = 1.47$ [a] wall on top in Figure 3.12 [b] down wall in Figure 3.12.
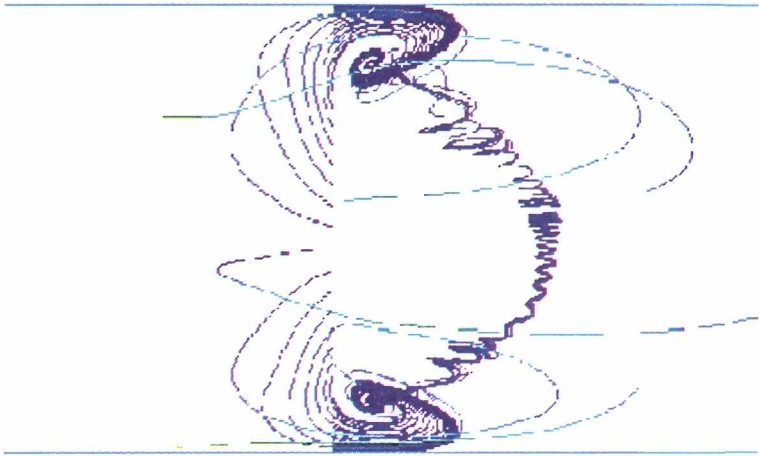
Figure 3.15 a
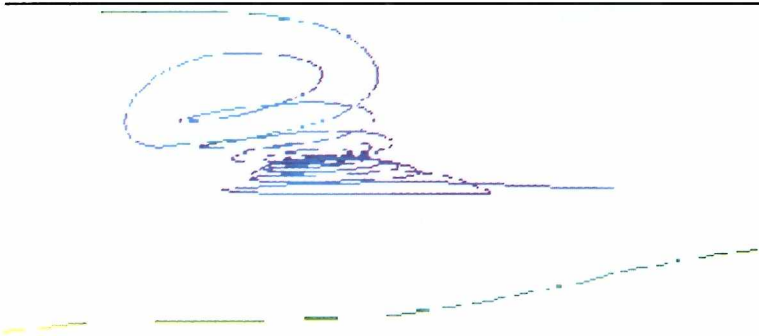
Figure 3.15 b

Figure 3.15. *Three-dimensional structures of the separation for the narrow channel for M_{is} = 1.47 [a] center vortex [b] flow patterns.*

A better understanding of the changes of the structures which occur due to the changes of the width of the channel or to the influence of the symmetry condition is aided by the diagram of the Takens-Bogdanov bifurcation. This shows the possible changes of the critical points including the appearance of the node, node saddle points or saddle focal points. This diagram is presented in Chapter 1 in Figure 1.8. It can explain, for instance from a topological point of view, the appearance of the vortex on the side wall for the narrow channel. It shows that on the bifurcation between one single saddle point, one saddle and one focal point that a saddle node connection can appear. This could be checked by making the computations for the channel with a width between the two considered cases.
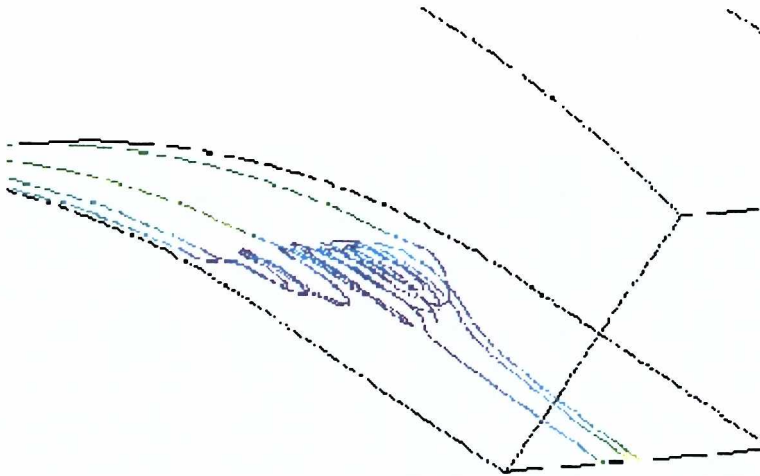
Figure 3.16. *Three-dimensional structures of the separation for the wide channel for $M_{is} = 1.47$.*

3.4 Comparison with experiment

In Figure 3.17 oil visualization pictures for an isentropic Mach number $M_{is} = 1.35$ are shown. For the wide channel, no structures can be recognized. For the narrow channel, some vortices are present but similar to the wide channel there is no separation in the middle of the channel. It can be observed that the behavior is similar for computations. The first separation occurs on the side wall. For the narrow channel in computations there are no vortices but the tendency for flow patters to create vortices can be noted (see Figure 3.2).

Figure 3.18 presents the flow for the isentropic Mach number $M_{is} = 1.47$. Considering the computations of the entire channel, the structures for the wide channel are the same as in the experiment. There are differences in the computations for the narrow channel. It can be noticed that the vortex occurred on the side wall in both computations and experiment. Such a vortex is not present for the wide channel. The tendency for the size of the separation region (larger for the narrow channel) can also be seen. The difference is that the structure for computations is closer to the wall and also less detailed. This is not connected with grid size because for the narrow channel the same grid was sufficient to render flow structure similar to the experiment. The same is true with the turbulence model. It gave results with good agreement for the wide channel. Due to this it seems that the reason for this fact could be the differences in the boundary layer on the side wall for experiments and numerics. The information about the boundary layer for the

experiment is not available. The computations and also experiments proved that shock induced separation in the curved channel is sensitive to the side wall boundary layer. It follows that this parameter is necessary for a correct comparison between numerics and experiment.

[a]   [b]
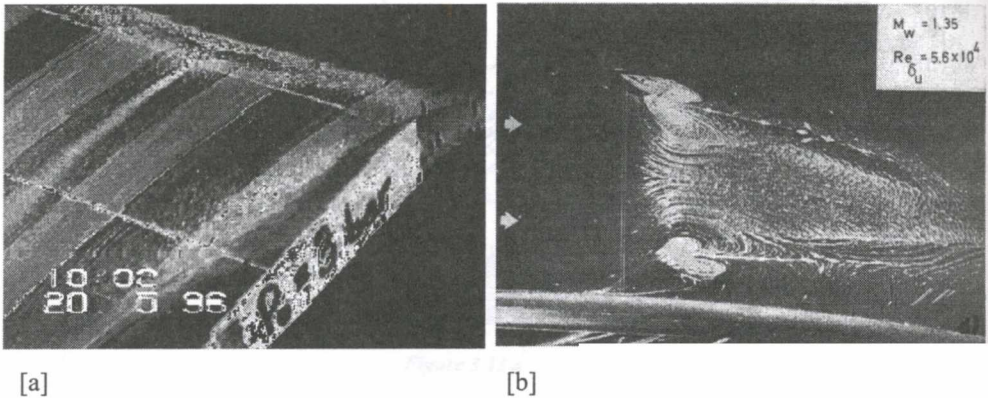
Figure 3.17. Oil visualization for $M_{is} = 1.35$ [a] wide channel; flow direction is from right to left; [b] narrow channel.

[a]   [b]
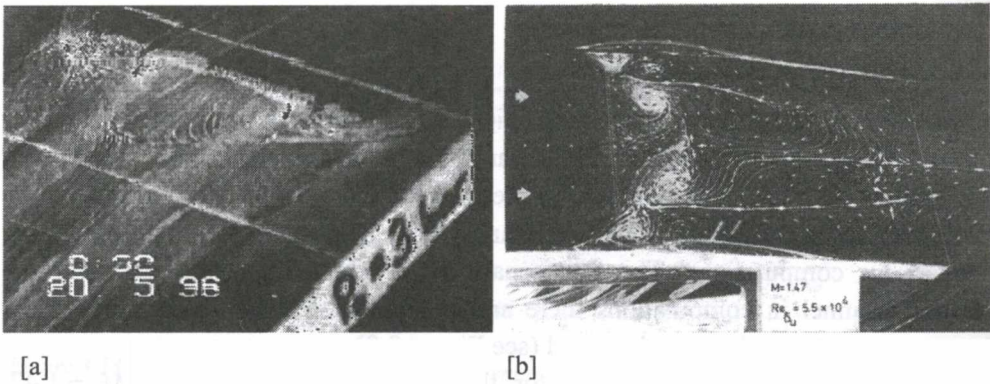
Figure 3.18. Oil visualization for $M_{is} = 1.47$ [a] wide channel; flow direction is from right to left; [b] narrow channel.

3.5 Summary

— The structures of separation depend on the Mach number for both experiment and computation. The separation is larger for $M_{is} = 1.47$. With an increasing Mach number, separation appears first on the side walls- bottom wall corner.

— The structures of separation depend on the width of the channel.

— The separation region is longer for a narrow channel for both experiment and computation. The size of the separation region relating to the width of the channel is also larger for the narrow channel than for the wide channel.

— The computed structures for the wide channel are similar to experiment. The direction of the non-symmetry of the computations can be caused by small numerical disturbance and for instance for a bit different grid it can changed for opposite.

— The computed structures of the narrow channel are a bit different than those obtained experimentally. This is probably caused by the differences in the side boundary layer between numerics and experiment. Information about the experimental boundary layer thicknesses are not available. It was shown that the side boundary layer has an influence on the structures of separation near the side and bottom walls. Due to this, information about the side boundary layer is very important for comparison.

— There is a very large influence of the symmetry condition on the structures of separation. The symmetric flow due to the separation became non-symmetric. The global separation structures are non-symmetric because of topological rules.

— It seems that the resolution of the grid was enough to render structures similar to experiment

— The used numerical scheme and turbulence model proved to be sufficiently efficient for an analysis of such highly complicated three-dimensional separation structures.

4. Conclusion

The boundary layer shock wave interaction is a complex phenomenon to study. The experimental and numerical investigations help in better understanding of this interaction. Due to the existence of three-dimensional effects the numerical study demands the application of as advanced numerical methods as it is possible. Any kind of restriction, like for instance the symmetry condition with the symmetric geometry, has a large influence on the computation results as it was shown in the presented thesis. The tree-dimensional effects especially for the shock and separation structures are so strong that widely used assumption about two--dimensionality for nominally two-dimensional geometry, cannot provide correct understanding of the boundary layer shock wave interaction.

It was shown that recent numerical methods are capable to predict the flow structure and shock induced separation structure with quite a good agreement with experiments. For the considered cases a large influence of the numerical scheme on the λ-foot structure and separation was obtained. Analysis carried out allowed to indicate which one is adequate for the investigated flow.

The topological methods help to analyse the complex structures of the flow. In some cases, like for the computations with the symmetry condition, they give the answer why such condition cannot be realized in real flow. The non-symmetry of the flow is forced by the nature of shock induced separation structures.

The future work could concentrate on the better understanding of influence of the parameters of the boundary layer or turbulence on the shock induced separation structures.

Appendix A

Classification of critical points

In this appendix the basic mathematical calculations for obtaining the linear classification of critical points are presented. First, the two-dimensional case will be considered. The equations are given as follows:

$$\dot{x} = ax + by; \tag{A.1}$$

$$\dot{y} = cx + dy. \tag{A.2}$$

The characteristic matrix looks like:

$$\begin{vmatrix} a - \lambda & b \\ c & d - \lambda \end{vmatrix}. \tag{A.3}$$

The solution of the system of ordinary differential equations is:

$$x = x_0 + K_1 exp(\lambda_1 t) + K_2 exp(\lambda_2 t); \tag{A.4}$$

$$y = y_0 + K_3 exp(\lambda_1 t) + K_4 exp(\lambda_2 t); \tag{A.5}$$

where x_0 and y_0 are the coordinates of the critical point. The classification of the critical point is based on the values of the eigenvalues λ_1 and λ_2:

1. $\lambda_1 < 0$ and $\lambda_2 < 0$ and $\lambda_1 \neq 0$ stable node

2. $\lambda_1 = \lambda_2 = \lambda$ and $\lambda < 0$ and the array of coefficients is proportional to the identity matrix — star stable node. Any small perturbation can cause a change in the stable node or focus

3. $\lambda_1 = \lambda_2 = \lambda$ and $\lambda < 0$ and the matrix of coefficient is not proportional to the identity matrix — degenerate stable node. Any small perturbation can cause a change to the stable node or focus

4. $\lambda_1 > 0$ and $\lambda_2 > 0$ and $\lambda_1 \neq \lambda_2$ unstable node $\lambda_1 = \lambda_2 = \lambda$ and $\lambda < 0$

5. $\lambda_1 = \lambda_2 = \lambda$ and $\lambda > 0$ and the matrix of coefficients is proportional to the identity matrix — unstable star node. It is not structurally stable and any small

perturbation causes a change in the unstable node or focus

6. $\lambda_1 = \lambda_2 = \lambda$ and $\lambda > 0$ and the matrix of coefficients is not proportional to the identity matrix — degenerated unstable node. It is not structurally stable and any small perturbation causes a change in the unstable node or focus

7. $\lambda_1 > 0$ and $\lambda_2 < 0$ or $\lambda_1 < 0$ and $\lambda_2 > 0$ saddle

8. $\lambda_{1,2} = \alpha \pm i\beta$ and $\alpha < 0$ — stable focus

9. $\lambda_{1,2} = \alpha \pm i\beta$ and $\alpha > 0$ — unstable focus

10. $\lambda_{1,2} = \pm i\beta$ and $\alpha = 0$ — center. It not structurally stable and any small perturbation causes a change in the stable and unstable focus

11. $\lambda_1 = 0$ and $\lambda_2 < 0$ The trajectories in phase space are parallel straight lines. It is not structurally stable and any small perturbations causes a change in the stable node or saddle

12. $\lambda_1 = 0$ and $\lambda_2 > 0$ The trajectories in the phase plane are the parallel straight lines. It is not structurally stable and any small perturbation causes changes in the unstable node or saddle

13. $\lambda_1 = 0$ and $\lambda_2 = 0$ and the matrix of coefficients is equal to zero — all points are points of equilibrium. It is not structurally stable and any small perturbation changes the system to the system with one point of equilibrium — star node

14. $\lambda_1 = 0$ and $\lambda_2 = 0$ and the matrix of coefficient is different from zero — the system is not structurally stable and any small perturbation changes the system to the system with one critical point — degenerated stable or unstable node

All the above cases were presented in Chapter 1. The next part of the appendix will consider three-dimensional critical point classification also regarding linear ordinary differential equations theory. The equations are given as follows:

$$\dot{x} = a_1 x + a_2 y + a_3 z; \tag{A.6}$$

$$\dot{y} = b_1 x + b_2 y + b_3 z; \tag{A.7}$$

$$\dot{x} = c_1 x + c_2 y + c_3 z. \tag{A.8}$$

The characteristic matrix looks like:

$$\begin{vmatrix} a_1 - \lambda & a_2 & a_3 \\ b_1 & b_2 - \lambda & b_3 \\ c_1 & c_2 & c_3 - \lambda \end{vmatrix}. \tag{A.9}$$

The solutions of the system of ordinary differential equations are:

$$x = x_0 + K_1 exp(\lambda_1 t) + K_2 exp(\lambda_2 t) + K_3 exp(\lambda_3 t); \tag{A.10}$$

$$y = y_0 + K_4 exp(\lambda_1 t) + K_5 exp(\lambda_2 t) + K_6 exp(\lambda_3 t); \tag{A.11}$$

$$z = z_0 + K_7 exp(\lambda_1 t) + K_8 exp(\lambda_2 t) + K_9 exp(\lambda_3 t); \tag{A.12}$$

The classification of critical point is based on the values of the eigenvalues λ_1 and λ_2 and λ_3:

1. $\lambda_1, \lambda_2, \lambda_3 > 0$ unstable node
2. $\lambda_1, \lambda_2, \lambda_3 < 0$
3. $\lambda_1, \lambda_2 > 0$ and $\lambda_3 < 0$ saddle type one
4. $\lambda_1, \lambda_2 < 0$ and $\lambda_3 > 0$ saddle type two
5. $\lambda_1 = \lambda_2 = \lambda_3 = \lambda$ and $\lambda > 0$ and the coefficient matrix is different than the identity matrix – unstable degenerate node. It is not structurally stable and any small perturbation causes a change in the unstable node or focal point
6. $\lambda_1 = \lambda_2 = \lambda_3 = \lambda$ and $\lambda < 0$ and the coefficient matrix is different than the identity matrix — stable degenerate node. It is not structurally stable and any small perturbation causes a change in the stable node or focal point
7. $\lambda_1 = \lambda_2 = \lambda_3 = \lambda$ and $\lambda > 0$ and the coefficient matrix is equal to identity matrix — unstable star node. It is not structurally stable and any small perturbation causes a change in the unstable node or focal point
8. $\lambda_1 = \lambda_2 = \lambda_3 = \lambda$ and $\lambda < 0$ and the coefficient matrix is different than the identity matrix — stable star node. It is not structurally stable and any small perturbation causes a change in the stable node or focal point
9. $0 < \lambda_1 < \alpha \; \lambda_{2,3} = \alpha \pm i\beta$ unstable focal point type one
10. $\alpha < \lambda_1 < 0$ and $\lambda_{2,3} = \alpha \pm i\beta$ stable focal point type one
11. $\lambda_1 < 0$ and $\alpha > 0$ and $\lambda_{2,3} = \alpha \pm i\beta$ unstable on the plane, but stable in three-dimensional space focal point type two
12. $\lambda_1 > 0$ and $\alpha < 0$ and $\lambda_{2,3} = \alpha \pm i\beta$ stable on the plane, but unstable in the three dimensional plane focal point type two
13. $0 < \alpha < \lambda_1$ and $\lambda_{2,3} = \alpha \pm i\beta$ unstable focal point type three
14. $\lambda_1 < \alpha < 0$ and $\lambda_{2,3} = \alpha \pm i\beta$ stable focal point type three
15. $\lambda_1 > 0 \; \lambda_{2,3} = \pm i\beta$ unstable center
16. $\lambda_1 < 0$ and $\lambda_{2,3} = \pm i\beta$ stable center
17. $\lambda_1 = 0$ and $\lambda_2, \lambda_3 > 0$ and $a_1 = 0$ unstable node two dimensional
18. $\lambda_1 = 0$ and $\lambda_2, \lambda_3 < 0$ and $a_1 = 0$ stable node two dimensional
19. $\lambda_1 = 0$ and $\lambda_2 > 0$ and $\lambda_3 < 0$ and $a_1 = 0$ or $\lambda_1 = 0$ and $\lambda_2 < 0$ and $\lambda_3 > 0$ and $a_1 = 0$ saddle two dimensional
20. $\lambda_1 = 0 \; \alpha < 0$ and $\lambda_{2,3} = \alpha \pm i\beta$ and $a_1 = 0$ stable focal point two dimensional
21. $\lambda_1 = 0 \; \alpha > 0$ and $\lambda_{2,3} = \alpha \pm i\beta$ and $a_1 = 0$ unstable focal point two dimensional
22. $\lambda_1 = 0$ and $\lambda_{2,3} = \pm i\beta$ and $a_1 = 0$ center two dimensional
23. $\lambda_1 = 0$ and $\lambda_2, \lambda_3 > 0$ and matrix of coefficients different than identity matrix – – unstable degenerate node

24. $\lambda_1 = 0$ and λ_2, $\lambda_3 < 0$ and matrix of coefficients different than the identity matrix — stable degenerate node

25. $\lambda_1 = 0$ and $\lambda_2 > 0$ and $\lambda_3 < 0$ or $\lambda_1 = 0$ and $\lambda_2 < 0$ and $\lambda_3 > 0$ and matrix of coefficients different than the identity matrix — degenerate saddle

26. $\lambda_1 = 0$ $\alpha < 0$ and $\lambda_{2,3} = \alpha \pm i\beta$ and matrix of coefficients different than the identity matrix stable degenerate focal point

27. $\lambda_1 = 0$ $\alpha > 0$ and $\lambda_{2,3} = \alpha \pm i\beta$ and matrix of coefficients different than the identity matrix unstable degenerate focal point

28. $\lambda_1 = 0$ and $\lambda_{2,3} = \pm i\beta$ and matrix of coefficients different than the identity matrix — degenerate center

29. $\lambda_1 = \lambda_2 = 0$ and $\lambda_3 > 0$ trajectories are parallel straight lines. The system is not structurally stable and any small perturbation causes a change in the unstable node or saddle

30. $\lambda_1 = \lambda_2 = 0$ and $\lambda_3 < 0$ trajectories are parallel straight lines. The system is not structurally stable and any small perturbation causes a change in the stable node or saddle

31. $\lambda_1 = \lambda_2 = \lambda_3 = 0$ and the matrix of coefficients is different from zero. The system is not structurally stable and any small perturbation causes changes to the degenerate node (stable or unstable)

Most of the considered cases are presented in Figures 1.2 and 1.5 in Chapter 1.

Appendix B

Dynamical systems on the manifold

This chapter will be devoted to the presentation of basic definitions and theorems connected with the dynamical systems on the manifold. This will complete considerations presented in Chapter 1 where the knowledge of all the definitions was assumed. The present chapter helps to understand better the considerations of Chapter 1.

First, the attention will be paid to the definition of the compact manifold.

Definition of the manifold:

The differentiable n-dimensional manifold is an arbitrary set M, whose elements are called points, together with the structure on it. The set M is the union of a finite or countable by infinite collection of subset with properties.

1. Each system has a defined local coordinate systems, which is identifiable with the Euclidean coordinate systems in Euclidean space.

2. Each non empty intersection of a pair of subsystems of the manifold has defined on it at least two coordinate systems, the restriction of first and second one. It is necessary that each of the coordinate system's intersections are identifiable with Euclidean n-space and each of these coordinate systems can be expressed in terms of the other in a one-to-one differentiable manner.

Definition of the compact manifold:

The topological space X is compact if every countable collection of open sets covering X contains sub-collections already covering X.

The next part will contain the definition of the dynamical system and some aspects of the critical point theory.

Definition of the dynamical system:

A dynamical system on a manifold is the smooth vector field on it.

Definition of the critical (singular) point:

The x_0 is called a critical (singular point) of the field $y = y(x)$ if $y(x_0) = 0$.

Definition of the isolated critical (singular) point:

The singular point is an isolated singular point, if for all other points of some small neighborhood of it, $y(x)$ does not vanish.

Definition of the non-degenerate critical (singular) point:

The critical (singular) point is non-degenerate if

$$\left(\frac{\partial y^\alpha}{\partial x^\beta}\right) \neq 0 \tag{B.1}$$

The non-degenerate singular point of the vector field is necessarily isolated.

Definition of the index of the singular point:

The index of the critical (singular) point is

$$sgn\ det\left(\frac{\partial\ y^\alpha}{\partial\ x^\beta}\right)\Big|_{x=x_0} = sgn(\lambda_1,\ldots,\lambda_n) \tag{B.2}$$

Appendix C

Numerical schemes: switch and slip

In this section the following equation will be considered:

$$\frac{\partial v}{\partial t} + \frac{\partial f(v)}{\partial x} = 0. \tag{C.1}$$

It can be approximated at the grid node i in conservation form by the scheme:

$$\Delta x \frac{dv_i}{dt} + \left(h_{i+\frac{1}{2}} - h_{i-\frac{1}{2}}\right) = 0. \tag{C.2}$$

$h_{i+\frac{1}{2}}$ is the numerical flux between cell i and $i+1$ and Δx is the mesh interval. The first order scheme, which satisfies the local extremum diminishing principle

(the local maxima do not increase and local minima do not decrease,) is obtained by approximating the flux as:

$$h_{i+\frac{1}{2}} = \frac{1}{2}(f_{i+1} - f_i) - d_{i+\frac{1}{2}},$$ (C.3)

where $d_{i+\frac{1}{2}} = \frac{1}{2}|d_{i+\frac{1}{2}}|\Delta v_{i+\frac{1}{2}} = a_{i+\frac{1}{2}}(v_{i+1} - v_i)$ is the first order diffusive flux computed at the cell interface $i+1$. Wave speed is $a(v) = \partial f / \partial v$.

Higher order non-oscillatory schemes are derived by introducing anti diffusive terms in a controlled manner, introducing approximate switch or by using limiters.

C.1 High-Resolution switched schemes

As was mentioned before, high-resolution switch schemes require that an anti diffusive term be introduced. By subtracting neighboring differences, the third order diffusive flux can be obtained as follows:

$$d_{i+\frac{1}{2}} = \alpha_{i+\frac{1}{2}}\Delta v_{i+\frac{1}{2}} - \left(\Delta v_{i+\frac{3}{2}} + \Delta v_{i-\frac{1}{2}} \right).$$ (C.4)

This scheme produces substantial oscillation in the vicinity of shock waves, which can be eliminated by switching locally to the first order scheme. The switch scheme given above can be improved as follows:

$$d_{i+\frac{1}{2}} = \varepsilon_{i+\frac{1}{2}}^{(2)}\Delta v_{i+\frac{1}{2}} - \varepsilon_{i+\frac{1}{2}}^{(4)}\left(\Delta v_{i+\frac{3}{2}} - 2\Delta v_{i+\frac{1}{2}} + \Delta v_{i-\frac{1}{2}} \right)$$ (C.5)

where

$$\varepsilon_{i+\frac{1}{2}}^{(2)} = min(\alpha_1, \alpha_2 S)\left| a_{i+\frac{1}{2}} \right|,$$ (C.6)

$$\varepsilon_{i+\frac{1}{2}}^{(4)} = max\left(0, \beta_1 \left| a_{i+\frac{1}{2}} \right| - \beta_2 \varepsilon_{i+\frac{1}{2}}^{(2)} \right).$$ (C.7)

S is the maximum of Q in the chosen neighborhood where Q is as follows:

$$Q_i = \left| \frac{\Delta v_{i+\frac{1}{2}} - \Delta v_{i-\frac{1}{2}}}{P_0 + (1-\varepsilon)P_1 + \varepsilon P_2} \right|,$$ (C.8)

$$P_1 = \left| \Delta v_{i+\frac{1}{2}} \right| + \left| \Delta v_{i-\frac{1}{2}} \right|,$$ (C.9)

$$P_2 = |\Delta v_{i+1}| + 2|\Delta v_i| + |\Delta v_{i-1}|. \tag{C.10}$$

The value of epsilon is usually taken as ½, P_0 is a threshold to assure that the denominator cannot be zero. $\alpha_1 = \frac{1}{2}$, $\beta_1 = \frac{1}{4}$ is chosen to scale diffusion to the level corresponding to up-winding. α_2, β_2 are chosen to switch the diffusion term from third to first order fast enough near the shock waves.

C.2 Symmetric limited positive scheme

Another method for obtaining a high order non-oscillatory scheme is to introduce flux limiters. In this scheme, third order diffusion defined by equation (D.2) is modified by introducing a limiter which produces an equivalent three point scheme with positive a coefficient. The limiter L(u, v) must have following properties:

1. L(u, v) = L(v, u);
2. $L(\alpha u, \alpha v) = \alpha L (u, v)$;
3. L(u, u) = u;
4. L(u, v) = 0 if u and v have opposite signs.

The diffusive flux for a scalar conservation law is

$$d_{i+\frac{1}{2}} = \alpha_{i+\frac{1}{2}} \left[\Delta v_{i+\frac{1}{2}} - L\left(\Delta v_{i+\frac{3}{2}}, \Delta_{i-\frac{1}{2}} \right) \right]. \tag{C.11}$$

The main restriction for this case is that the limiter must be zero when the $\Delta_{i+\frac{3}{2}}$ and $\Delta_{i-\frac{1}{2}}$ have opposite signs. This means that there is a local extremum at i or $i+1$. If they have the same sign and $\Delta_{i+\frac{1}{2}}$ has the opposite, the damping is similar to the central difference formula. In the case of a shock when the upstream flow is constant, then $\Delta_{i-\frac{1}{2}} = 0$ and $\Delta_{i+\frac{3}{2}}$ prevent canceling any part of $\Delta_{i+\frac{1}{2}}$, because it is limited by $\Delta_{i-\frac{1}{2}}$.

A limiting function can be used such as:

$$L(u,v) = S(u,v)min(|u + v| / 2, \alpha|u|, \alpha|v|), \tag{C.12}$$

where

$$S(u,v) = \frac{1}{2} sign(u) + sign(v). \tag{C.13}$$

Comparison of both schemes shows that the slip scheme has different dissipation near the shock waves than the switched scheme. It can also be noted that the vicinity of the λ-foot structure and separation region is characterized by a few

local extrema. Due to this fact, the grid in this area should have much higher density otherwise slip scheme limitation causes damping that is too large (extrema cannot be caught so easily) and no separation occurs. Because of this, the number of grid points near the shock wave and boundary layer interaction for the slip scheme should be very high. This is not so easy to obtain for three-dimensional calculations due to computer memory limitation. The switch scheme seems more advisable, because it gives more accurate results, for the considered grid resolution for the flows with shock waves and separations.

Bibliography

[1] Agrawal S., Robinsosn B. A., Barnett R. M., *Prediction of vortex breakdown on a D wing*, 5th Sym. on Num. and Phys. Aspects of Aerodynamic Flows, California Sate University, January 13-15, 1992

[2] G.A.Allen Jr., *A general method for solving the Navier-Stokes equation analytically for jets*, DFVLR Interner Bericht IB 222-85 A 43

[3] Almosnino D., *Topology of vortices in conical flow*, AIAA 16th Fluid and Plasma Dyn. Conf, Danvers Massachusetts, July 12-14, 1983

[4] Auerbach D., *Vortex generation at sharp edges, two and three dimensional effects*, MPI, ISSN 0436-1199, Bericht 12, 1985

[5] Bastedo W. G. Jr., Mueller T. J., *The spanwise variation of laminar separation bubbles on finite wings at low Reynolds numbers*, AIAA 18th Fluid Dyn. and Plasma Dyn. and Laser Conf., Cincinatti Ohio, July 10-18, 1985

[6] Bauker P. G., *On the bifurcation phenomenae in conical flow patterns*, Report Delft Univ. of Tech. LR-378, April 1983

[7] Bauker P.G., de Winkel U.E.M., *On the topology of three-dimensional separated flow structures and local solutions of the Naver-Stokes equations*, IUTAM Symp. on Topological Fluid Mech., Cambridge U.K., pp. 1318-1818, 1989

[8] Belotserkovskiy O. M., *Numerical simulation of flow separation*, Fluid Mech. Soviet Research, vol. 16, no. 6, November-December, 1987

[9] Bernard P. S., Thomcy J. M., Handler R. A., *Vortex dynamics and the production of Reynolds stress*, J. Fluid Mech., vol. 253, pp. 385-419, 1993

[10] Betyaer S. K., Gaifullin A. M., *Large-scale structure of the core of a spiral discontinuity in a fluid*, Izvestiya Akademii Nauk SSSR, Mekhanika Zhidkosti i Gaza, no. 5, pp. 53-60, September-October 1982

[11] Bhattacharjee S., Scheelke B., Troutt T. R., *Modification of vortex interactions in reattaching separated flow*, AIAA Shear Flow Control Conf., Boulder Colorado, March 12-14, 1985

[12] Bippes H., Turk M., *Oil flow patterns of separated flow on a hemisphere cylinder at incidence*, IB 222-82A07 DFVLR Interner Bericht, 1982

[13] Bradshaw P., Wang F. Y. F., *The reattachement and relaxation of a turbulent shear layer*, J. Fluid Mech., vol. 52, part 1, pp. 113-135, 1972

[14] Brown S. N., Stewartson K., *Laminar separation*, Ann.Rev. Fluid Mech. 1, 45, pp. 45-72, 1969

[15] Brune G. W., *Topology in aerodynamics — an aid for the interpretation of flow patterns*, Boening Report D6-51878, 1983

[16] Buckmaster J., *Perturbation technique for the study of three-dimensional separation*, The Phys.of Fluids, vol. 15, no. 12, December 1972

[17] Burggraf O. R., *Analytical and numerical studies of the structure of steady separated flows*, J. Fluid Mech., vol. 24, par. 1, pp. 113-151, 1966

[18] Cebeci T., *Progress in the calculation of three dimensional boundary layers on bodies of revolution at incidence*, Douglas Aircraft Company, Long Beach Calif. 1977

[19] Chamberlain J. P., Weston R. P., *Three-dimensional Navier-Stokes calculations of multiple interacting vortex rings*, AIAA 17th Fluid Dyn., Plasma Dyn. and Lasers Conf., Snowmass Colorado, June 25-27 1984

[20] Chamberlain J. P., Liu, C. H., *Navier-Stokes calculations for unsteady three-dimensional vortical flows in unbounded domain*, AIAA 22nd Aerospace Sciences Meeting, Reno Nevada, January 9-12 1984

[21] Cooke J. C., Robins A. J., *Boundary-layer flow between nodal and saddle points of attachment*, J. Fluid Mech., vol. 41, part 4, pp. 823-835, 1970

[22] Craft T. J., Launder B. E., Suga K., *Extendind the applicability of eddy viscosity models through the use of deformation invariants and non-linear elements*, 5th IAHR Conf. on Refined-Flow Modelling and Turbulence Measurement, Paris France, September 7-10, 1993

[23] Czerwińska J., *Computation of the 3-D transonic flow in a nozzle*, Opr. IMPPAN, 119/98, 1998

[24] Czerwińska J., *Dwu i Trójwymiarowa analiza topologiczna struktur elementarnych w przepływie*, XIII KKMP w Częstochowie, 1998

[25] Czerwińska J., *Two dimensional flow in curved channel*, Opr. IMPPAN 194/98, 1998

[26] Czerwińska J., *Computation of the 3-D transonic flow in a curved channel*, Opr. IMPPAN 260/98, 1998

[27] Dallmann U., Vollmers H., Su W. H., *Flow Topology and Tomography for Vorex Identification in Unsteady and 3-D Flows*, Proceedings IV TAM Symposium Denmark, May 25-29, 1997

[28] Dallmann U., *Topological structures of 3-D flow separations*, DLR 221-82 A07

[29] Dallmann U., *Topological structures of 3-D vortex flow separation*, AIAA 16th Fluid Dyn., Plasma Dyn. and Lasers Conf., Danvers Massachusetts, July 12-14, 1983

[30] Dallmann U., *On the formation of 3-D vortex flow structures*, DLR Interner Bericht, IB 221-85A13, 1985

[31] Dallman U., *3-D vortex separation phenomena — a challenge to numerical methods*, Procee. of the 5th GAMM-Conf. on Num. Meth. in Fluid Mech., Rome Italy, October 5-7, 1983

[32] Dallman U., *Structural stability of 3-D vortex flows*, Lecture notes in eng., vol. 13, Nonlin. Dyn. of Transcritical Flows, Procee. of DFVLR Intr. Collq., Bonn Germany, March 26, 1984

[33] Dallman U., Gebing H., *Flow attachment at flow separation lines*, Acta Mechanica, vol. 4, pp. 47-56, 1994

[34] Dallman U., Gebing H., *How to validate unsteady flow simulations? - on topological equivalence of separated flow around spheres and ellipsoids*, 5th Intr. Symp. on Comp. Fluid Dyn., Sendai Japan, August 31 — September 3, 1993

[35] Dallman U., Gebing H., Vollmers H., *Unsteady 3-D separated flows around a sphere — analysis of vortex chain formation*, IUTAM Symp. on Bluff-Body Wakes, Dynamics and Instabilities, Goettingen Germany, September 7-11, 1992

[36] Dallmann U., Hilgenstock A., Riedelbauch S., *On the footprints of 3-D separated vortex flow around blunt bodies*, AGARD Conf. Procee. 494, Vortex Flow Aerodynamics, Scheveningen Netherlands, October 1-4, 1990

[37] Dallmann U., Kordulla W., Vollmers H., *3-D separated flow structures*, IUTAM Symp. Boundary Layer Separation, London UK, 1986

[38] Dallmann U., Kordulla W., Vollmers H., Schulte-Werning B., *Analysis of the charging topological structures of 3-D separated flows*, Phy. of Sep. Flow.-Num.Exp. and Theor. Aspects, Vieweg, Braun Schweig, Numerical Fluid Mech., vol. 40, 1993

[39] Dallmann U., Schulte-Werning B., *On the 3-D and unsteadiness of separated flows*, 3rd Intr. Cong. of Fluid Mech., Cairo Egypt, January 2-4, 1990

[40] Dallmann U., Schulte-Werning B., *Topological changes of axisymmetric and non-axisymmetric vortex flows*, IUTAM Symp. Cambridge UK, August 13-18, 1989

[41] Davey A., *Boundary layer flow at a saddle point of attachment*, Fluid Mech., vol. 10, pp. 593-610, 1961

[42] Dean W. R., *Note on the motion of liquid near a position of separation*, Proceed. of the Cambridge Philos. Soc., vol. 46, pp. 293-306, 1950

[43] Degani D., Schiff L. B., *Numerical simulation of the effect of spatial disturbances on vortex asymmetry*, 27th Aerospace Science Meet., Reno Nevada, January 9-12, 1989

[44] Deng G. B., Piquet J., *Navier-Stokes computations of horseshoe vortex flows*, Intr. J. of Num. Meth. in Fluids, vol. 15, pp. 9-24, 1992

[45] Doerffer P., *Oddziaływanie pomiędzy prostopadłą falą uderzeniową a turbulentną warstwą przyścienną*, Zesz. Nauk. IMPPAN, 309/1270/90, 1990

[46] Doerffer P., Kania W., Bejm M., *Oddziaływanie pomiędzy falą uderzeniową a turbulentną warstwą przyścienną*, Opr. IMPPAN, 269/97, 1997

[47] van Dommelen L. L., Shen S. F., *The flow at a rear stagnation point is eventually determined by exponentially small values of the velocity*, J. Fluid Mech., vol. 157, pp. 1-16, 1985

[48] Duck P. W., *3-D marginal separation*, NASA Technical Memorandum 101411, COMP-88-22, 1988

[49] Duck P. W., Unsteady three-dimensional separation including breakdown, NASA Techn.Memorandum 102525, ICOMP-90-07, February 1990

[50] Elliott J. W., Smith F. T., *Dynamic stall due to unsteady marginal separation*, J. Fluid Mech., vol. 179, pp. 489-512, 1987

[51] Franujione J. G., Ottino J. M., *Feasibility of numerical tracking of material lines and surfaces in chaotic flows*, Phys. Fluids, vol. 30 (12), pp. 3641-3643, December 1987

[52] Freymuth P., Finaish F., Bank W., *Visualization of the vorex street behind a circular cylinder at low Reynolds numbers*, Phys. Fluids 29 (4), April 1986

[53] Freymuth P., Finaish F., Bank W., *Three-dimensional vortex patterns in a starting flow*, J. Fluid Mech, vol. 161, pp. 239-248, 1985

[54] Freymuth P., Finaish F., Bank W., *The wing tip vortex system in a starting flow*, ZFW 10, Heft 2, 1986

[55] Freymuth P., Finaish F., Bank W., *Futher visualization of combined wing tip and starting vortex systems*, AIAA Journal, vol. 25, no. 9, September 1987

[56] Fross J. F., *Surface selections and topological constraint evaluations for flow field analyses*, Univ. Erlangen-Nurnberg, 1988

[57] Fujii K., *Navier-Stokes simulation of transonic flow over wing-fuselage combinations*, AIAA 4th App. Aerodyn. Conf., San Diego California, June 9-11, 1986

[58] Fujii K., *Practical applications of ne LU-ADI scheme for the 3-D Navier-Stokes computation of transonic viscous flows*, AIAA 24th Aerospace Sciences Meet., Reno Nevada, January 6-9, 1986

[59] Gersten K., *Corner interface effects*, AGARD report 288, March 1959

[60] Gersten K., Herwig H., Wauschkuhn P., *Theoretical and experimental investigations of two dimensional flows with separated regions of finite length*, AGARD Conf. Procee. no. 291, Comp. of Viscous-Invicvid Interactions, 1980

[61] Ghia U., Ghia K. N., Rubin S. G., Khosla P. K., *Study of incompressible flow separation using primitive variables*, Computers and Fluids, vol. 9, pp. 123-142, 1981

[62] Golovkin V. A., Klyavkin V. M., Kolkov V. G., *Optical visualization of accelerated and decelerated flow over a circular cylinder*, Izvestiya Akademii Nauk SSSR, Mekhanika Zhidkosti i Gaza, no. 2, pp. 136-142, March-April 1981

[63] Gushehin V. A., Nkonshin V., *Numerical simulation of the unsteady separated fluid flows in wide range of Reynolds numbers*, Intr. CFD Conf., Nagoya Japan, August, 1989

[64] Hall M. G., *A theory for the core of a leading-edge vortex*, Fluid Mech., vol. 11, pp. 209-228, 1961

[65] Han T., Patel V. C., *Flow separation on spheroid at incidence*, J. Fluid Mech., vol. 92, part 4, pp. 643-657, 1979

[66] Hanxin Z., *The behavor of separation line and separation criterion in three dimensional steady flows*, 3rd ACFM, Tokyo Japan, pp. 62-65, 1986

[67] Harper J. F., *On the boundary layers in two dimensional flow with vorticity*, Fluid Mech 17, 1963

[68] Hayes W. D., *The three-dimensional boundary layer*, Navord Report 1313 Nots 384, May 1951

[69] Herberg T., *Numerische Simulation und Analyse der sationären und instationären laminaren Ablöseblase an der zurückspringenden, abgerundeten Stufe mit Hilfe der Karhunen-Loeve Zerlegung*, DLR 95-31

[70] Hilgenstock A., *Validation of transonic turbulent flows past D wing configurations*, Aeronautical Journal, pp. 219-230, August-September 1991

[71] Hilgenstock A., Vollmers H., Dallmann U., *Open separation and vortex formation numerical simulation and analysis of a D wing flow*, 10th Australasian Fluid Mech. Conf., Melbourne Australia, December 11-15, 1989

[72] Himeno R., Shirayama S., Kamo K., Kuwahara K., *Computational study of 3-D wake structure*, AIAA 18th Fluid Dyn. and Plasma Dyn. and Lasers Conf., Cincinnati Ohio, July 16-18, 1985

[73] Hirschel E. H., Bretfhauer N., Röhe H., *Theoretical and experimental boundary-layer studies on car bodies*, MBB-UFE122-AERO-MT 610, 1982

[74] Hirschel E. H., *Computation of 3-D boundary layers at fuselages*, MBB-UFE122-AERO-MT-615, 1982

[75] Hirschel E. H., *Three-dimensional boundary layer calculations in design aerody-namics*, Proc. IUTAM Symp. on 3-D turb. bound.-lay., Berlin, March 29-31, 1982

[76] Hirschel E. H., *Boundary-layer computations on non-axisymmetric bodies*, MBB-UFE122-AERO-MT-591, 1982

[77] Hirschel E. H., Kordulla W., *Local properties of Three-dimensional separation lines*, Z.F.W. 4, Heft 5, 1980

[78] Hirschel E. H., Rizzi A., *The mechanism of vorticity creation in Euler solutions for lifting wings*, MBB-LKF R2-AERO-MT-753, 1987

[79] Hornung H. G., *The vortex skeleton model for 3-D steady flows*, DFVLR, 1983

[80] Hornung H. G., Perry A. E., *Streamsurfaces bifurcation, vortex skeletons and separation*, DFVLR Interner Bericht, IB 222-82 A25

[81] Howarth L., *On the calculation of steady flow in the boundary layer near the surface of a cylinder in a stream*, Report no. 1632, Amsterdam 1934

[82] Hsieh T., Wang K. C., *Concentrated vortex on the nose of an inclined body of revolution*, AIAA Journal, vol. 14 no. 5, pp. 698-700, May 1976

[83] Huang Z., *Hydrodynamic visualization of 3-D separated flow*, 27th Aerospace Sciences Meet., Reno Nevada, January 9-12, 1982

[84] Huevre P., Monkewitz P. A., *Local and global instabilities in spatially developing flows*, Ann. Rev. Fluid Mech., vol. 22, pp. 473-573, 1990

[85] Hung C. M., *Computations of Navier-Stokes equations for three dimensional flow separation*, NASA Tech. Mem. 102266, December 1989

[86] Hung C.M., Sung C. H., Chen C. L., *Computation of saddle point of attachement*, AIAA 22nd Fluid Dyn. Plasma Dyn. and Lasers Conf., Honolulu Hawaii, June 24-26, 1991

[87] Hunt J. C. R., Abell C. J., Peterka I. A., Woo H., *Kinematical studies of the flows around free or surface-mounted obstacles; applying topology of the flow visualization*, J. Fluid Mech, vol. 86, part 1, pp. 179-200, 1978

[88] Ishii K., Kuwahara K., Ogawa S., Chyn W. J., Kawamura T., *Computation of flow around a circular cylinder in a supercritical regime*, 18th Fluid Dyn. and Plasma Dyn. and Lasers Conf., Cincinatti Ohio, July 16-18, 1985

[89] Jaroch M., *Oil flow visualization experiments in the separated and reattachment regions of the flow past a transverse flat plate with a long splitter plate*, Z.Flugwiss. Weltraumforsch, 11, 230-236, 1987

[90] Klemp J. B., A.Acrivos, *A moving-wall boundary layer with reverse flow*, J. Fluid Mech., vol. 76, part 2, pp. 363-381, 1976

[91] Kline S. J., Bardina J., Strawn R., *Correlation and computation of deattachement and reattachment of turbulent boundary layers on two dimensional surfaces*, AIAA 14th Fluid and Plasma Dyn. Conf., Palo Alto California, June 23-25, 1981

[92] Kluwick A., Interacting boundary-layers, ZAMM 67 4, T3-T13, 1987

[93] Kluwick A., Gittler P., Bodonyi R. J., *Viscous-inviscid interactions on axisymmetric bodies of revolution in supersonic flow*, J. Fluid Mech., vol. 140, pp. 281-301, 1984

[94] Kordulla W., Müller B., Vollmers H., *Comparison of two different Navier-Stokes methods for the simulation of 3-D transonic flows with separation*, 27th Aerospacee Sciences Meet., Reno Nevada, January 9-12, 1989

[95] Kraemer K., *On vortex-sheet-separation with particular reference to the D-wing leading-edge-separation*, IUTAM-Symp. on Concentrated Vortex Motions in Fluid, Ann Arbor, Mich. July 6-11, 1964

[96] Kuwahara K., *Flow simulation on supercomputers and its visualization*, The 15th National Conf. on Theor. and Appl. Mech., Tainan Taiwan, December 13-14 1991

[97] Kuwahara K., Ishii K., *Computation of flow around a circular cilinder in a supercritical regime*, Symp. on Num. Sim. in Aerodyn., Tokyo Japan, February 3, 1986

[98] Lee H., Schetz J. A., *Computational and experimental study of tip vortices*, AIAA Applied Aerodynamics Conf., AIAA-83-1868, 1983

[99] Legendre R., *Évolution réguliere on catastrophique d'écoulements permanents dépendant de parametres*, La Recherche Aerospatiale, no. 4, p. 225-232, 1982

[100] Legendre R., *Lignes de Courant d'un écoulement permanent décollement et séparation*, La Recherche Aérospatiale, no. 6, p. 327-335, 1977

[101] Legendre R., *Séparation de l'écoulement laminaire tridimensionnel*, La Recherche Aéronautique, no. 54, 1956

[102] Legendre R., *Écoulement au voisinage de la pointe avant d'une aile a forte fleche aux incidences moyennes*, VIII Congres Inter. de Mécanique Théorique et Appliquée, Istamboul 1952

[103] Leuchter O., Solignac J. L., *Experimental investigation of the turbulent structure vortex wakes*, ONERA report 107, 1983

[104] Lim T. T., Chong M. S., Perry A. E., *The viscous tornado*, 7th Australasian Hydraulics and Fluid Mech. Conf., Brisbane, 18-22 August 1980

[105] Lin C. H., Tavantzis J., Ting L., *Numerical studies of motion of vortex filaments — implementing the asymptotic analysis*, AIAA 17th Fluid Dyn., Plasma Dyn. and Laser Conf., Snowmass Colorado, June 25-27 1984

[106] Lindroos M., *Numerical integration of the Navier-Stokes equations for steady flow past a wavelike bulge on a flat plate*, Helsinki Univ.of Techn. Lab. of Aerodyn., report no. 78-A2, series A, December 1978

[107] Lohe M. A., *Existence an uniqueness of generalized vortices*, J.Math.Phys. 24 (1), January 1983

[108] Lowson M. V., Riley A. J., Swales C., *Flow structure over D wings, 33rd Aerospace Sciences Meeting and Exhibit*, Reno Nevada, 9-12 January, 1995

[109] Lugt H. J., Ohring S., *The oblique ascent of a viscous vortex pair toward a free surface*, J. Fluid Mech., vol. 236, pp. 461-476, 1992

[110] Magagniato F., *„Kappa" — Karlsruhe Parallel Program for Aerodynamics*, TASK Quarterly, vol. 2 no. 1, 1998

[111] Marconi F., *The spiral singularity in the supersonic inviscid flow over a cone*, AIAA 16th Fluid and Plasma Dyn. Conf., Danvers Massachusetts, July 12-14, 1983

[112] Maruhn K., *Drukverteilungsrechnungen au elliptischen Rümpfen und in ihrem Ausenramen*, Luftfartforschung, 1941

[113] Mason P. J., Sykes R. J., *Three-dimensional numerical integrations of Navier-Stokes equations for flow over surface-mounted obstacles*, J. Fluid Mech., vol. 91, part 3, pp. 433-450, 1979

[114] Mason P. J., *Trailing vorticies induced by surface mounted obstacles*, Meteorological Research Unit RAF, Cardington, July 1982

[115] Maull D. J., East L. F., *Three-dimensional flow in cavities*, J. Fluid Mech., vol. 16, part 4, pp. 620-632, 1963

[116] Meier H. U., Kreplin H. P., Vollmers H., *Development of boundary layers and separation patterns on a body of revolution at incidence*, DFVLR IB 222-82A34, 1982

[117] Merkine L. O., Brevdo L., *Boundary-layer separation of a two-layer rotating flow on a b-plane*, J. Fluid Mech., vol. 167, pp. 31-48, 1986

[118] Moffatt H. K., *Viscous and resistive eddies near a sharp corner*, Fluid Mech. 18, pp. 1-18, 1963

[119] Mokhtari S., Bradshaw P., *Longitudinal vortices in wind tunnel wall boundary layers*, Aeronautical J., pp. 233-236, june-July 1983

[120] Mou-Ji L. et al, *Flow patterns and aerodynamic characteristics of wing with strake*, AIAA paper 79-1877, Aircraft Syst. and Techn. Meet. New York, August 20-22 1979

[121] Musller T. J., *Flow visualization by direct injection*, Fluid Mech. Measur., Springer-Verlag, 1986

[122] Nakamura A., *Relation between certain quasi-vortex solutions and solitons of the Sine-Gordon equation and other nonlinear equations*, J.of the Physical Soc. of Japan, vol. 52, no. 6, pp. 1918-1920, 1983

[123] Nakamura J., *Steady wake behind a sphere*, The Phys. of Fluids, vol. 19, no. 1, pp. 5-8, January 1976

[124] Oshima Y., Kuwahara K., *Experimental and numerical study of vortex interaction*, AIAA 17th Fluid Dyn., Plasma Dyn. and Lasers Conf., Snowmass Colorado, June 25-27, 1984

[125] Peace A. J., Riley N., *A viscous vortex pair in ground effect*, J. Fluid Mech., vol. 129, pp. 409-426, 1983

[126] Peake D. J., Tobak M., *On the issues concerning flow separation and vortical flows in 3-D*, NASA Tech. Mem. 84374, June 1983

[127] Peake D. J., Tobak M., *Three dimensional separation and reattachement*, AGARD report, 1982

[128] Peake D. J., Tobak M., *Three-dimensional interactions and vortical flows with emphasis on high speeds*, AGARD Report, no. 252, July 1980

[129] Peregrine D. H., *A note on the steady high Reynolds number flow around a circular cylinder*, J. Fluid Mech., vol. 157, pp. 493-500, 1963

[130] Perry A. E., Fairlie B. D., *Critical points in flow patterns*, Advances in Geophysics, vol. 18B, pp. 299-315, 1974

[131] Perry A. E., Chong M. S., Hornung H. G., *Local solutions of the Navier-Stokes equations in separated flows*, Third Symposium on Numerical and Physical Aspects of Aerodynamic Flows, Cal. State Univ, Long Beach 1985

[132] Perry A. E., Lim T. T., Chong M. S., *The instantaneous velocity fields of coherent structures in coflowing jets and wakes*, J. Fluid Mech, vol. 101, part 2, pp. 243-256, 1980

[133] Perry A. E., Chong M. S., *A series-expansion study of the Navier-Stokes equations with applications to 3-D separation patterns*, J. Fluid. Mech, vol. 173, pp. 207-223, 1986

[134] Perry A. E., Watmuft J. H., Chong M. S., *Flow visualization using hot-wire anemometry*, pp. 785-789

[135] Perry A. E., Lim T. T., *Coherent structure in coflowing jets and wakes*, J. Fluid Mech., vol. 88, pp. 451-463, 1978

[136] Perry A. E., Watmuft J. H., *The phase-averaged large-scale structures in 3-D turbulent wakes*, J. Fluid Mech, vol. 103, pp. 33-51, 1981

[137] Perry A. E., Tan D. K. M., *Simple 3-D vortex motions in coflowing jets and wakes*, J. Fluid Mech, vol. 141, pp. 197-231, 1984

[138] Perry A. E., Steiner T. R., *Large-scale vortex structures in turbulent wakes behind bluff bodies*, part I, Vortex formations process, Part II Far wake structures, Univ.of Melbourne, July 1985

[139] Perry A. E., *A study of degenerate and non-degenerate critical points in 3-D flow fields*, DFVLR Interner Bericht, IB 222-83 A 35

[140] Perry A. E., Lim T. T., Chong M. S., *Critical point theory and its application to coherent structures and the vortex shedding process*, Dept.of Mech. Eng.Univ of Melbourne, Parkville Australia April 1979

[141] Perry A. E., *A series expansion study of Navier-Stokes equations*, DFVLR-FB-84-34

[142] Pullin D. J., *The large-scale structure of unsteady self-similar rolled-up vortex sheets*, J. Fluid Mech., vol.88, part 3, pp. 401-430, 1978

[143] Purohit S. C., Shang J. S., Hankey W. L. Jr., *Effect of suction on the wake structure of a three-dimensional turet*, AIAA 16th Fluid and Plasma Dyn.Conf., Danvers Massachusetts, July 12-14 1983

[144] Ragab S. A., Nayfek A. H., *A comparison of second order triple-deck theory and interacting boundary layers for incompressible flows past a hump*, AIAA 18th Aerospace Sciences Meet., Pasadena California, January 14-16, 1980

[145] Rizzetta D. P., Burggraf O. R., Jenson R., *Triple-deck solutions for viscous supersonic and hypersonic flow past corners*, J. Fluid Mech., vol. 89, part 3, pp. 535-552, 1978

[146] Robinson A. C., Saffman P. G., *Three-dimensional stability of vortex arrays*, J. Fluid Mech., vol. 125, pp. 411-427, 1982

[147] Rogers S. E., Kwak D., Kaul U. K., *A numerical study of three-dimensional incompressible flow around multiple posts*, AIAA 24th Aerospace Sciences Meeting, Reno Nevada, January 6-9, 1986

[148] Ruban A. I., *Singular solution of boundary layer equations which can be extended continuosly through the point of zero surface friction*, Izvestiya Akademii Nauk SSSR, Mekhanika Zhidkosti i Gaza, no. 6, pp. 42-52, December 1981

[149] Ruban A. I., *The theory of laminar separation of a fluid at an angular inflection on a surface*, Fluid Mechanica - Soviet Research, vol. 6, no. 3, May-june, 1977

[150] Savulescu St. N., *A topological model for the onset of large scale changes in Blasius boundary layer*, Max Plank Institut für Strömungsforshung MPI-FB 86

[151] Seshadri S. N., Narayan K. Y., *Possible types of flow on lee-surface of D wings at supersonic speeds*, Aeronautical Journal, pp. 185-199, May 1988

[152] Seshadri S. N., Narayan K. Y., *Shock-induced separated flows on the lee-surface of D wings*, Aeronautical Journal, pp.128-141, May 1988

[153] Shen C., Floryan J. M., *Low Reynolds number flow over cavities*, Phys. Fluids, vol. 28 (11), pp. 3191-3202 November 1985

[154] Shirayama S., *A structure of tip vortices at a D wing*, AIAA 20 th Fluid Dyn. Plasma Dyn. and Lasers Conf., Buffalo New York, june 12-14, 1989

[155] Shirayama S., *Flow past a sphere: topological transitions of the vorticity field*, AIAA J., vol. 30, no. 2, pp. 349-358, February 1992

[156] Shirayama S., Kuwahara K., *Computational study of flow in curved pipes with circular cross-section*, AIAA/ASME 4th Fluid Mech., Plasma Dyn. and Lasers Conf., Atlanta Georgia, May 12-14, 1986

[157] Shulte-Werning B., Dallmann U., Müller B., *Some aspects of the numerical simulation of compressible viscous flow around bluff bodies at low Ma number*, Procee. of the 8thGAMM-Conf. on Num Meth. in fluid Mech., 1990

[158] Shulte-Werning B., Dallmann U., *Numerical simulation of the vortex chain formation by vorticity shedding from a sphere into the wake*, IUTAM Symp. on Separated Flows and Jets, Novosibirsk UdSSR, July 9-13, 1990

[159] Sibulkin M., *A note on the bathtub vortex and the earth's rotation*, American Scientist, vol. 71, July-August 1983

[160] Smith F. T., *Steady and unsteady boundary layer separation*, Ann. Rev. Fluid Mech., vol. 18, pp. 197-220, 1986

[161] Smith F. T., *Laminar flow of an incompressible fluid past a bluff body; separation, reattachment eddy properties and drag*, J. Fluid Mech., vol. 92, part 1, pp. 171-205, 1979

[162] Smith J. H. B., *Vortex flow in aerodynamics*, Ann. Rev. Fluid Mech., vol. 18, pp. 221-242, 1986

[163] Stephan K., Lin S., Durst M., Huang F., Seher D., *An investigation of energy separation in a vortex tube*, Int. J. Heat Mass Transfer, vol. 26, no. 3, pp. 341-348, 1983

[164] Stewartson K., *On Goldstein's theory of laminar separation*, Quart. J. Mech. and Appl. Matem., vol. XI, pp. 4, 1958

[165] Stewartson K., Smith F. T., Kaups K., *Marginal separation*, Studies in Applied Math. 67, pp. 45-61, 1982

[166] Stock H. W., *Computation of the boundary layer and separation lines on inclined ellipsoids and of separated flow on infinite swep wings*, AIAA 13th Fluid and Plasma Dyn. Conf., Snowmass Colorado, July 14-16, 1980

[167] Stropsky D. M., Djilali N., Gartshore J.S., Salcudean M., *Application of momentum integral methods and linearized potential theory for predicting separation bubble characteristics*, Transs. of the ASME, vol. 12, December 1990

[168] Suzuki K., Kubota H., *Topology of computed incompressible three dimensional separated flow field around high angle of attack cone-cylinders*, Procee. Intr. Symp. Comp. Fluid Dyn., pp. 317-322, August 1989

[169] Tafti D. K., Vanka S. P., *A numerical study of flow separation and reattachment on a blunt plate*, Phy Fluids A, vol. 3, no. 7, pp. 1749-1759, July 1991

[170] Taneda S., *Formation of streamwise vorticies in the flow past a corner*, Jour. of Physical Society of Japan, vol. 52, no. 1, pp. 8-9, January 1983

[171] Tani I., *Critical survey of published therories on the mechanism of leading-edge stall*, Aeoronautical Research Inst., Univ. Tokyo, Report no. 367, June 1961

[172] Tatsumi S., Martinelli L., Jameson A., *Flux-limited schemes for the compressible Navier-Stokes equations*, AIAA J., vol. 33, no. 2, February 1995

[173] Tatsumi S., Martinelli L., Jameson A., Design, *Implementation, and Validation of flux limited schemes for the solution of the compressible Navier-Stokes equations*, AIAA-94-0647, 32nd Aerospace Sciences Meet., Reno Nevada, January 10-13, 1994

[174] Tobak M., Peake D. J., *Topological structures of 3-D separated flows*, AIAA 14th Fluid and Plasma Dyn. Conf., Palo Alto California, June 23-25, 1981

[175] Tobak M., Ünal A., *Bifurcations in unsteady aerodynamics*, NASA Tech. Mem. 88316, June 1986

[176] Tomboulides A. G., Triantafyllou G. S., Karniadalus G. E., *A new mechanism of period doubling in free shear flows*, Phys. Fluids A, vol. 4, pp. 1329-1332, July 1992

[177] Townsend A. A., *The behaviour of a turbulent boundary layer near separation*, J. Fluid Mech, vol. 12, pp. 536-554, 1962

[178] Varty R. L., Currie J. G., *Measurements near a laminar separation point*, J. Fluid Mech., vol. 138, pp.1-19, 1984

[179] Visbal M. R., *The laminar horseshoe vortex system formed at a cylinder*, AIAA 22nd Fluid. Dyn. and Lasers Conf., Honolulu Hawaii, June 24-26 1991

[180] Visbal M. R., *Structure of laminar juncture flows*, AIAA Journ., vol. 29, no. 8, pp. 1273-1282, August 1991

[181] Visbal M. R., *Structure of vortex breakdown on a pitching D wing*, AIAA 93-0434, 31st Aerospace Sciences Meet. and Exhibit, Reno Nevada, January 11-14, 1993

[182] Visbal M. R., Gordnier R. E., *Parametric effects on vortex breakdown over a pitching D wing*, 32nd Aerospace Sciences Meet. and Exhibit, Reno Nevada, January 10-13, 1994

[183] Visbal M. R., Gordnier R. E., *Crossflow topology of vortical flows*, AIAA J., vol. 31, no. 5, pp. 1085-1087, 1993

[184] Vollmers H., *Integration of streamlines from measured static pressure fields on a surface*, 6th US-FRG DEA Meet., „Viscous and Interacting Flow Field Effects", Goettingen Germany, April 28-30, 1981

[185] Vollmers H., Kreplin H. P., Meier H. V., *Separation and vortical-type flow around a prolate spheroid — evaluation of relevant parameters*, Conf. Procee. Aerodynamics of Vortical Type Flows in 3-D, no. 342, 1983

[186] Vorus W. S., *A theory for flow separation*, J. Fluid Mech., vol. 132, pp. 163-183, 1983

[187] Wang K. C., *Separation patterns of boundary layer over an inclined body of revolution*, AIAA Journal, vol. 10 no. 8, pp. 1044-1050, August 1972

[188] Wang K. C., *On the disputes about open separation*, AIAA 21 Aerospace Sciences Meeting, Reno Nevada, January 10-13 1983

[189] Wang K. C., Hsieh T., *Separation patterns at high incidences*, AIAA 10th Applied Aerodynamics Conf., Palo Alto California, June 22-24, 1992

[190] Mc Williams J. C., Frierl G. R., *On the evolution of isolated, nonlinear vortices*, J. Phys. Oceanography, vol.9, pp. 1155-1182, November 1979

[191] Williams J. C., *Incompressible boundary-layer separation*, Ann. Rev. Fluid Mech, vol. 9, pp. 113-144, 1977

[192] Winkelmann A. E., *On the occurrence of mushroom shaped stall cells in separated flow*, AIAA 16th Fluids and Plasma Dyn. Conf., Danvers Masssachusets, July 12-14, 1983

[193] Winckelmans G. S., *Topics in vortex methods for the computation of three- and two-dimensional incompressible unsteady flows*, Calif. Inst. of Techn., February 1989

[194] *Calculation of 3-D separated turbulent flow in boundary layer*, AGARD report 255, 1990

[195] *Vortex flow aerodynamics*, AGARD report 494, 1990